INTEGRATING SEQUENCE STRATIGRAPHY AND ROCK-PHYSICS TO INTERPRET SEISMIC AMPLITUDES AND PREDICT RESERVOIR QUALITY

A DISSERTATION

SUBMITTED TO THE DEPARTMENT OF GEOPHYSICS

AND THE COMMITTEE ON GRADUATE STUDIES

OF STANFORD UNIVERSITY

IN PARTIAL FULFILLMENT OF THE REQUIREMENTS

FOR THE DEGREE

OF DOCTOR OF PHILOSOPHY

Tanima Dutta

August 2009

I certify that I have read this dissertation and that, in my opinion, it is fully adequate in scope and quality as a dissertation for the degree of Doctor of Philosophy.

_____
Gary Mavko (Principal Adviser)

I certify that I have read this dissertation and that, in my opinion, it is fully adequate in scope and quality as a dissertation for the degree of Doctor of Philosophy.

_____
Tapan Mukerji

I certify that I have read this dissertation and that, in my opinion, it is fully adequate in scope and quality as a dissertation for the degree of Doctor of Philosophy.

_____
Stephan Graham

Approved for the University Committee on Graduate Studies

Abstract

This dissertation focuses on the link between seismic amplitudes and reservoir properties. Prediction of reservoir properties, such as sorting, sand/shale ratio, and cement-volume from seismic amplitudes improves by integrating knowledge from multiple disciplines. *The key contribution of this dissertation is to improve the prediction of reservoir properties by integrating sequence stratigraphy and rock physics.*

Sequence stratigraphy has been successfully used for *qualitative* interpretation of seismic amplitudes to predict reservoir properties. Rock physics modeling allows *quantitative* interpretation of seismic amplitudes. However, often there is uncertainty about selecting geologically appropriate rock physics model and its input parameters, *away from the wells*.

In the present dissertation, we exploit the predictive power of sequence stratigraphy to extract the spatial trends of sedimentological parameters that control seismic amplitudes. These spatial trends of sedimentological parameters can serve as valuable constraints in rock physics modeling, especially away from the wells. Consequently, rock physics modeling, integrated with the trends from sequence stratigraphy, become useful for interpreting observed seismic amplitudes away from the wells in terms of underlying sedimentological parameters. We illustrate this methodology using a comprehensive dataset from channelized turbidite systems, deposited in minibasin settings in the offshore Equatorial Guinea, West Africa.

First, we present a practical recipe for using closed-form expressions of effective medium models to predict seismic velocities in unconsolidated sandstones. We use an effective medium model that combines perfectly rough and smooth grains (the extended Walton model), and use that model to derive coordination number, porosity, and pressure relations for P and S wave velocities from experimental data. Our recipe provides reasonable fits to other experimental and borehole data, and specifically improves the predictions of shear wave velocities. In addition, we provide empirical relations on normal compaction depth trends of porosity, velocities, and V_P/V_S ratio for shale and clean sands in shallow, supra-salt sediments in the Gulf of Mexico.

Next, we identify probable spatial trends of sand/shale ratio and sorting as predicted by the conventional sequence stratigraphic model in minibasin settings (spill-and-fill model). These spatial trends are evaluated using well data from offshore West Africa, and the same well data are used to calibrate rock physics models (modified soft-sand model) that provide links between P-impedance and quartz/clay ratio, and sorting. The spatial increase in sand/shale ratio and sorting corresponds to an overall increase in P-impedance, and AVO intercept and gradient. The results are used as a guide to interpret sedimentological parameters from seismic attributes, away from the well locations.

We present a quantitative link between carbonate cement and seismic attributes by combining stratigraphic cycles and the rock physics model (modified differential effective medium model). The variation in carbonate cement volume in West Africa can be linked with two distinct stratigraphic cycles: the coarsening-upward cycles and the fining-upward cycles. Cemented sandstones associated with these cycles exhibit distinct signatures on P-impedance vs. porosity and AVO intercept vs. gradient crossplots. These observations are important for assessing reservoir properties in the West Africa as well as in other analogous depositional environments.

Finally, we investigate the relationship between seismic velocities and time temperature index (TTI) using basin and petroleum system modeling at Rio Muni basin, West Africa. We find that both V_P and V_S increase exponentially with TTI. The results can be applied to predict TTI, and thereby thermal maturity, from observed velocities.

Acknowledgments

The journey to get a Ph.D. degree from Stanford has been the most wonderful and enriching experience for me. I am indebted to all the people who have made this possible.

First, I want to express my gratitude to Gary Mavko for being an outstanding adviser. Without his guidance, constructive criticism, and encouragement, this dissertation was not possible. Gary is an open-minded dynamic researcher, and he embraced the idea of linking sequence stratigraphy and rock physics. He taught me to approach scientific investigations with the open mind of a detective, and consider all possibilities before arriving at the conclusion. I have been fortunate for having the opportunity to work with Gary. *Thank you Gary!*

I want to thank Tapan Mukerji for teaching me never to loose that holy curiosity. After meeting Tapan, I realize that knowledge is infinite, and a Ph.D. is not enough! Tapan has been a great resource in my research; whenever I was stuck, he was always there to rescue me with his brilliant ideas. Tapan taught me the significance of broadening knowledge in different subjects, along with honing skills in a specialized subject. I am truly lucky that I had Tapan as my teacher and mentor. *Dhanyabad Tapan!*

I thank Steve Graham for making sure that our research was acceptable to a sedimentologist and a stratigrapher. I have learned a lot of geology from Steve, both in class and on several fantastic field trips. In particular, I had a memorable time participating in the sequence stratigraphy field trip at Utah and Colorado. I am honored to

participate in field trip at Death Valley and present at the SPOODS annual meeting. The discussions with Steve and his students have been very fruitful for my thesis. Special thanks to Jack Dvorkin for his constructive comments, which have been crucial in my research. Thanks to Tiziana Vanonorio for her enthusiasm and encouragement.

I express a great deal of thanks to the SRB program and its sponsors for the financial support during five years of my stay at Stanford. Along with that, I sincerely thank Fuad Nijim for his extraordinary administrative skills. Fuad, thanks for taking care of the things that we generally take for granted.

I acknowledge Hess Corporation and Charlie West (formerly at Hess) for providing us an excellent dataset from Equatorial Guinea, offshore West Africa. A special thanks to Jim Hewlett and Steve Utchtyl for helping me understand the stratigraphic setting from this study area. I am grateful to BP for providing us the borehole data from shallow sediments located in the Gulf of Mexico. Thanks to Per Avseth, Norsk Hydro and Fugro for the seismic and well data from Campos Basin, Brazil. I express my sincere gratitude to Time Lane (BP) and Ken Peters (USGS) for their collaborations with my Ph.D. research. I also thank Michael A. (Mike) Payne for his positive feedback in my work.

I thank all the students of the SRB group whom I had the pleasure of knowing and working with: thanks to Mauricio, Anyela, Ingrid, Diana, Youngseuk, Ezequiel, Kyle, Kevin, Cinzia, Kaushik, Richa, Franklin, Ratna, Carmen, Piyapa, Ramil and Danica. You all have enriched my life in some fashion.

A special thanks to Franklin and his wife Yasmary for helping my family at a critical time. Thanks to Richa for the wonderful time we spent together. We did many things together at Stanford, including taking classes, engaging in nature studies, playing tennis and badminton. I am honored to have close friendship from Ratna. He taught me some interesting aspects on granular medium, while I tried teaching him basic sedimentology and stratigraphy. We always had a great *adda*, countless discussions on endless topics, which we cherished for long hours.

I am indebted to my parents, Kalpana Dutta and Ashim Dutta, and my brother, Tanmay, for their continuous support and encouragement. Without the unconditional love

and guidance from my parents, I would not have become what I am today. My mother advised me to achieve perfection in whatever I do, while my father reminded me to maintain a good sense of humor with a positive attitude towards life. Thank you *Ma* and *Baba* for all the values you taught me and for all the sacrifices you made for me, which you consider nothing at all, but I am grateful.

I deeply thank my best friend and husband, Kaushik for his extraordinary patience and constant encouragement, and for the small things he does everyday to make me happy. Without Kaushik, there is no way I would be able to finish my Ph.D. He instilled the love for Geo-science in my early career. I have truly benefited discussing my research with Kaushik, he has been always the best critic in my work. I am really fortunate to have Kaushik as companion in this wonderful voyage of life. I dedicate this dissertation, with all my heart and with all my soul, to Kaushik and to our son, Anik Banerji.

Contents

List of Tables

List of Figures

Chapter 1
Introduction

"With every new answer unfolded, science has consistently discovered at least three new questions."
--Werner Von Braun

1.1 Objective

The main objective of this dissertation is to improve the prediction of reservoir properties from seismic amplitudes by integrating sequence stratigraphic principles and rock physics models. This general objective contains three specific goals: 1) To identify the predictable, spatial trends of reservoir properties using a sequence stratigraphic framework; 2) To link reservoir properties with seismic velocities using an improved rock physics model; and 3) To improve the understanding, specifically, of seismic signatures for depositional as well as diagenetic processes in West Africa deep-water environment. The overall problem and motivations for each of these specific objectives are described below.

1.2 The problem: what geologic processes control reflection amplitude

Prediction of reservoir quality (e.g., porosity, permeability, net-to-gross) is a critical element for exploration and development of hydrocarbon accumulations in sedimentary basins (Kupecz et al., 1997). The spatial and temporal variability of these reservoir properties is of primary importance for evaluating the economic potential of hydrocarbon reservoirs. Reflection seismology has been extensively used in hydrocarbon exploration, and has been particularly successful in reservoir delineation, characterization and monitoring (e.g., Berg and Woolverton, 1985; Sheriff and Geldart, 1995; Brown, 1991).

Reflection seismology paved the way to development of seismic stratigraphy (Payton, 1977). The fundamental principle of seismic stratigraphy is that within the resolution of the seismic method, seismic reflections and their amplitudes usually correspond to chronostratigraphic surfaces. A chronostratigraphic surface represents a break in depositional record known as a hiatus. Two key questions to address are:

1. What are the critical sedimentological parameters that control impedance contrast at a hiatus?

2. How do these sedimentological parameters vary spatially, parallel and perpendicular to chronostratigraphic surfaces?

To solve the questions stated above, we need to understand the geologic processes at the hiatus in a sequence-stratigraphic framework. This will guide us to select sedimentological parameters that determine reflection amplitude. The spatial and temporal variations of sedimentological parameters and their trends as indicated by sequence stratigraphy can serve as constraints in rock physics modeling, especially away from the wells.

1.3 Background and motivation

1.3.1 Predicting trends of sedimentological parameters from sequence stratigraphy

The findings in seismic stratigraphy allowed the development of sequence stratigraphy as a new paradigm in geological sciences (Sloss, 1963; Mitchum et al., 1977;

Weimer and Link, 1991). Sequence stratigraphy can predict the probable spatial relationship of reservoir rocks, source rocks and seals from reflection continuity, geometry and stacking patterns in post-stack seismic sections. This tool has been successfully used for qualititative interpretation of seismic amplitudes and velocities to predict reservoir properties (e.g., Peickert, 1985; Neidell et al., 1985; Zeng et al., 2003). In the present dissertation, we exploit this predictive power of sequence stratigraphy to extract the critical sedimentological parameters that control seismic impedance.

Seismic impedance depends on several sedimentological parameters such as sand/shale ratio, textural maturity (sorting, grain sphericity and angularity), position of clay within pore micro-structure (laminar vs. dispersed) and different diagenetic processes (quartz overgrowth, clay mineral authigenesis and pressure solution). This has been demonstrated by several researchers (e.g., Murphy, 1982; Han; 1986; Nur et al., 1991; Mavko and Jizba; 1991; Marion 1990; Yin 1992; Marion et al., 1992; Nur et al., 1995; Avseth et al., 2000; Gutierrez, 2001; Florez, 2005). The interpretation of seismic amplitude is therefore inherently non-unique. Our goal is to minimize this non-uniqueness by identifying critical sedimentological parameters and systematic trends of their spatial variations as indicated by sequence stratigraphic interpretation in a particular depositional setting. Let us consider the following example.

Figure 1.1 shows a submarine fan system in a post-stack seismic section. In order to improve the prediction of reservoir properties from seismic data, it is crucial to know how the sedimentological parameters are varying from the proximal to the distal location. If we know the reservoir properties at the proximal location, how can we quantitatively predict their spatial variations distally? Does the sand/shale ratio increase at the distal location? Are the sands at the distal location better sorted? Do the amplitude anomalies correspond to any diagenetic carbonate cements? The problem becomes easier to solve if we pose the questions in a sequence-stratigraphic framework. Sequence stratigraphic models from an analog depositional environment can be used to predict the systematic relative changes of these sedimentological parameters.

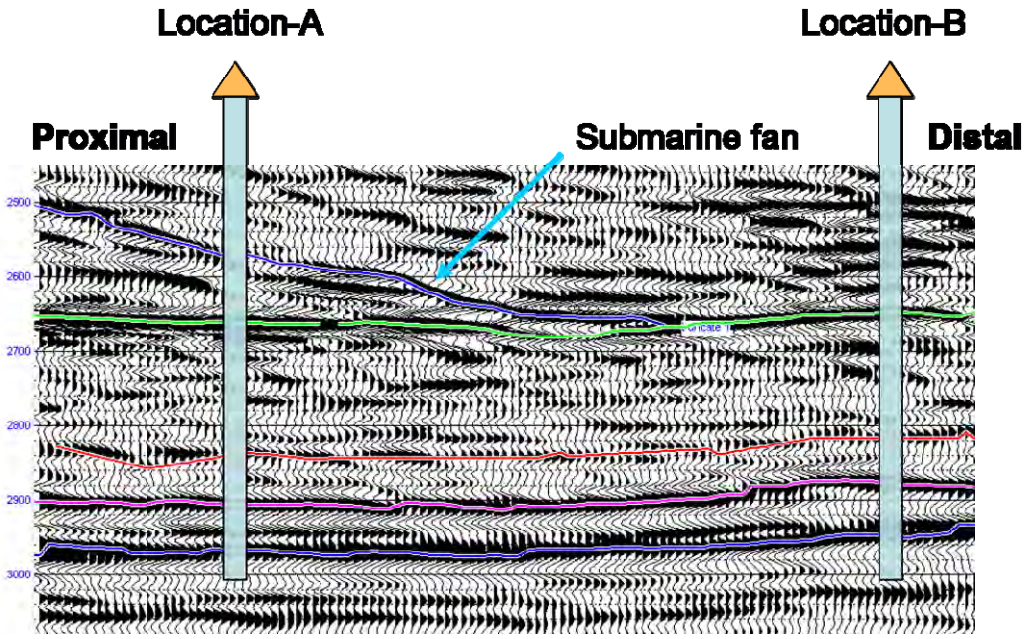

Figure 1.1: An example seismic section from Campos Basin, Brazil. In order to improve the prediction of reservoir quality away from the wells, it is essential to understand the systematic spatial variation of sedimentological properties from the proximal location (A) to the distal location (B).

1.3.2 Improved rock physics model for linking sedimentological parameters with seismic properties

Rock physics modeling allows the interpretation of seismic amplitude to transit from the qualitative to the quantitative domain by establishing a quantitative link between sedimentological parameters and elastic properties. Rock physics models are particularly useful for testing multiple possible geological scenarios using well logs. When integrated with sequence stratigraphy, rock physics modeling can also be useful for interpreting observed seismic amplitudes away from the wells in terms of underlying sedimentological parameters.

Commonly used rock physics models for unconsolidated sediments, e.g., the soft-sand model (Dvorkin et al., 1996; Mavko et al., 1998) tend to overpredict shear wave velocities (e.g., Goddard, 1990; Zimmer, 2003; Makse et al., 2004). In order to mitigate this overprediction, the modeled effective shear modulus at the critical porosity is often divided by an ad hoc correction factor. Another completely ad hoc fix is to use the frictionless versions of contact models (e.g., frictionless version of Walton, 1987 model)

combined with unrealistically high coordination numbers. One of our goals in this dissertation is to improve the rock physics modeling in unconsolidated sediments using an appropriate coordination number, porosity and pressure relation.

1.3.3 Reservoir characterization of turbidite system in West Africa for depositional and diagenetic processes

Sequence stratigraphic principles are more robust in marginal marine settings than in deep-water depositional environments. Since sediments in marginal marine environments are deposited at or near sea level, they are extremely sensitive to changes in relative sea-level, and are therefore particularly suitable for high resolution sequence stratigraphy (Emery and Meyers, 1996). However, Posamentier and Weimer (1993) have emphasized the need for extending the sequence stratigraphic principles to deep marine environments.

Deep water environments constitute potentially large volumes of unexplored hydrocarbon in several sedimentary basins of the world (Pettingill, 1998), and therefore exploration and delineation of reservoirs in such environments have an increasing focus in petroleum industry (Weimer and Slatt, 2004). Since deep-water systems are often characterized by very complex distributions of sediments, reservoir characterization based on conventional seismic and well-logs may be uncertain in these environments (Tyler and Finley, 1991; Weimer et al., 2000). There is a need to incorporate rock physics for reservoir characterization in deep-water, as has been already shown by Avseth (2000).

A comprehensive dataset from offshore West Africa available through Hess Corporation provides us with a unique opportunity to study depositional and diagenetic processes in channelized turbidites deposited at the continental slope. The dataset consists of thin-sections, cores, well logs, post stack, and partial stack seismic data. We combine appropriate rock physics models and sequence stratigraphic models to quantify the seismic signatures due to depositional processes (sand/shale ratio, sorting) as well as diagenesis of carbonate minerals present in siliciclastic reservoirs.

1.4 Terminology for communicating with multiple disciplines

Since the present dissertation is interdisciplinary in nature, it is important that we carefully select the terminologies for a better communication with audience from multiple disciplines. There are some terminologies that are familiar to petrophysicist and rock- physicist for decades, but they bear little significance to a sedimentologist. In order to bridge this gap in communication, we have prepared a table that will be relevant for both rock-physicist and sedimentologist, shown in Table 1.1. In this table, we have also included rock physics models for different scenarios. We have used the terms shown in Table 1.1 interchangeably in this thesis.

Table 1.1: Terminologies used by rockphysicist and sedimentologist.

Rock physics Model	Rock physics	Sedimentology
Backus average	Laminated shaly sand [(1)]	Interbedded shale and sandstones (centimeter scale)
		Laminaset of alternating sand and shale lamina (milimeter scale)
Thomas-Stieber, Marion and Yin	Dispersed shaly sand [(2)]	Suspended sand in clay-rich matrix or Pseudomatrix
		Lack of laminations due to flocculated clay and/or bioturbation
Soft-sand, Modified soft-sand	Soft-sand (acoustically softer)	Uncemented sands
Contact cement, Constant cement, Stiff-sand, Modified DEM	Stiff-sand (acoustically stiffer)	Cemented sandstones

[(1)] For rock physics, an arrangement of alternating shale and sand units, that leads to elastic anisotropy. This includes very fine scale features such as varves or coarse scale features such as bedsets. For sedimentology, laminated shaly sands are formed due to compaction of dispersed clay. [(2)] For rock physics, bimodal mixing of shale and sand giving a V pattern in the velocity-porosity crossplot. For sedimentology, dispersed *sandy-shale* corresponds to suspended sand grains in clay-rich matrix due to debris flow in turbidites or bioturbation. And, dispersed *shaly-sand* corresponds to psedomatrix formed by detrital shale clasts, rip-up clasts, and micas due to deep burial.

1.5 Chapter descriptions

This thesis consists of seven chapters, including this introduction. The chapters are linked together and represent different scenarios for integrating sedimentology, stratigraphy and rock physics.

Chapter 2 introduces a workflow to integrate sequence stratigraphy and rock physics. We use sequence stratigraphic interpretations to obtain critical sedimentological parameters that affect seismic amplitudes and identify the predictable trends of their relative spatial variations. These spatial trends are then used to constrain rock physics models and their input parameters away from the wells. We include an example of this workflow for quantifying sorting trends in progradational lobes of a submarine fan system from the Campos Basin, Brazil. We obtain a distinct trend of variation in sorting and porosity from landward to basinward in the AVO intercept-gradient plane. These trends can serve as a template to guide the interpretation of observed intercept and gradient away from the wells. This chapter was presented at the 76th Annual International SEG Convention in New Orleans (Dutta et al., 2006), and has been published in The Leading Edge (Dutta et al., 2007a).

Chapter 3 provides a practical recipe for using closed-form expressions of effective medium models to predict seismic velocities in unconsolidated sandstones. We use an effective medium model that combines perfectly rough and smooth grains (the extended Walton model), and use that model to derive coordination number, porosity, and pressure relations for P and S wave velocities from experimental data. Our recipe provides reasonable fits to other experimental data on glass-beads and Ottawa sands, and specifically improves the predictions of shear wave velocities. The results of this chapter are important for establishing normal compaction trends in unconsolidated sands in the shallow subsurface (demonstrated in Chapter 4). This chapter has been submitted at Geophysics, and will be presented at the 79th Annual International SEG Convention in Houston (Dutta et al., 2009b).

Chapter 4 presents normal compaction depth trends of porosity, velocities, and

V_P/V_S ratio in shallow, supra-salt sediments in the Gulf of Mexico. For this, we combine data from multiple sources, such as isonic (sonic-while-drilling), geotechnical and core measurements from shallow sections of the Gulf of Mexico, and laboratory measurements on unconsolidated sands conducted at low effective pressure. The compaction trends in clean sandstones are consistent with the predictions of our improved granular medium model presented in Chapter 3. These results can be useful in establishing normal compaction trends in the shallow sub-surface, where log data are usually not available and are of poor quality. Establishing such trend curves is important in seismic exploration for several reasons, especially for detecting drilling hazards and distinguishing it from shallow resource-potential prior to drilling in deep-water environments. This chapter has been has been published in The Leading Edge (Dutta et al., 2009a).

Chapter 5 establishes a link between conventional sequence stratigraphic interpretations and quantitative seismic amplitudes. Specifically, we quantify the spatial trends of sand/shale and sorting in a laminated, channelized turbidite sequence deposited within minibasin settings offshore Equitorial Guinea, West Africa. First, we identify probable spatial trends of sand/shale and sorting as predicted by the conventional sequence stratigraphic model in minibasin settings (spill-and-fill model). Next, these trends are evaluated using well data, and the same well data are used to calibrate rock physics models (modified soft-sand model) that provide links between P-impedance and quartz/clay, and sorting. Our modeling suggests that the spatial increase in sand/shale and sorting corresponds to an overall increase in P-impedance, intercept, and gradient. The results can be applied to quantify sedimentological parameters from seismic attributes, away from the well locations. This chapter was presented at the 77th Annual International SEG Convention in San Antonio (Dutta et al., 2007b).

Chapter 6 presents a quantitative link between carbonate cement and seismic impedance by combining sequence stratigraphic cycles (system tracts) and rock physics models. The variation in carbonate cement volume in West Africa can be linked with two distinct stratigraphic cycles: the coarsening-upward cycles and the fining-upward cycles,

and cemented sandstones associated with these cycles exhibit distinct signatures on P-impedance vs. porosity crossplot. The carbonate cemented sandstones from the fining-upward cycles are often associated with extensive cementation, resulting in lower porosity and higher P-impedance. In contrast, those from the coarsening-upward cycles are often associated with dissolution, resulting in higher porosity and lower P-impedance. The P-impedance vs. porosity trends of these rocks can be quantitatively interpreted using the modified differential effective medium model with cement volume as constraints from prior sequence stratigraphic interpretation. Our results suggest that combining sequence stratigraphic cycles and rock physics model can be useful to quantify reservoir quality associated with carbonate cementation and subsequent dissolution from seismic impedance. This chapter was presented at AGU Annual Meeting (Dutta et al., 2007c), 78th Annual International SEG Convention in Las Vegas (Dutta et al., 2008a), and Annual International AAPG Convention in San Antonio (Dutta et al., 2008b).

Chapter 7 investigates the relationship between seismic velocities and time temperature index (TTI). TTI, an important thermal maturity indicator, is directly linked with oil and gas generation, and can be linked with chemical compaction and onset of overpressure. In this chapter, we propose an empirical-numerical relation between TTI and seismic velocities. We perform petroleum system modeling at a well location in a deep-water petroleum system at Rio Muni Basin, offshore West Africa. The TTI values obtained from numerical modeling are then compared with velocities measured at the same well location. We find that both V_P and V_S increase exponentially with TTI. The results presented in this chapter can be applied to predict TTI, and thereby thermal maturity, from observed velocities. This chapter was presented at Annual International AAPG Convention in San Antonio (Dutta et al., 2008c).

1.6 Future implications and visions

The work in this dissertation will enable practitioners in the upstream petroleum industry to perform seismic reservoir characterization in a more physically and

geologically reliable way. An immediate extension of our work will be to consider variability in sedimentological parameters in overburden shale. The predictive trends of total organic content, silt content and clay particle orientation in shales will serve as valuable constraints in rock physics modeling.

Moreover, one can extend the work presented in this dissertation, and make seismic reservoir characterization even more integrated, taking into account other uncertainties than those related to variability in sedimentological parameters. This includes uncertainties related to thin-bed effects, tuning, and anisotropy.

The physical link between sequence stratigraphy, sedimentology and rock physics should be combined with statistics to account for uncertainties related to data and model parameters (Mavko and Mukerji, 1998; Takahashi, 2000; Avseth et al., 2005). Also, one can expand on our deterministic approach and include spatial multi-point statistics for predicting reservoir quality from seismic data (e.g., Gonzalez et al., 2008). The same methodology may be applied for other resources, like acquifer characterization from subsurface measurements.

1.7 References

Avseth, P., 2000, Combining rock physics and sedimentology for seismic reservoir characterization in North Sea turbidite systems: Ph.D. thesis, Stanford University.

Avseth, P., T. Mukerji, and G. Mavko, 2005, Quantitative Seismic Interpretation: Applying Rock Physics Tools to Reduce Interpretation Risk: Cambridge University Press.

Berg, R., and D. Woolverton, 1985, Seismic Stratigraphy II: An integrated Approach to Hydrocarbon Exploration, American Association of Petroleum Geologists Memoirs, 39.

Brown, A., 1991, Interpretation of Three-dimensional Seismic Data, third edition, American Association of Petroleum Geologist Memoirs, 42.

Dutta, T., Mukerji, T., and Mavko, G., 2005, Modeling elastic properties of unconsolidated sands: Eos Transactions, American Geophysical Union, 86, MR33A-0144.

Dutta, T., Mukerji, T., Mavko, G., and Avseth, P., 2006, Reservoir quality prediction by integrating sequence stratigraphy and rock physics: SEG Expanded Abstracts, 25, 1811-1815.

Dutta, T., Mukerji, T., and Mavko, G., 2007a, Rock physics modeling constrained by sequence stratigraphy: The Leading Edge, 26, 870.

Dutta, T., Mukerji, T., and Mavko, G., 2007b, Quantifying spatial trend of sediment parameters in channelized turbidite, West Africa: SEG Expanded Abstracts, 26, 1674-1679.

Dutta, T., Mukerji, T., and Mavko, G., 2007c, Seismic Response of Carbonate Cemented Sandstones, Eos Transactions, American Geophysical Union, 88(52), MR31C-0529.

Dutta, T., Mukerji, T., and Mavko, G., 2008a, How does carbonate cementation in sandstones affect seismic response?: SEG Expanded Abstracts, 27, 1675-1679.

Dutta, T., Mukerji, T., and Mavko, G., 2008b, How sedimentological variations in carbonate cemented sandstones affect seismic impedance?: AAPG Search and Discovery Article # 50130.

Dutta, T., Mukerji, T., Mavko, G., and Peters, K., 2008c, Do the seismic velocities depend on time-temperature index?: AAPG Search and Discovery Article # 40348.

Dutta, T., Mukerji, T., Mavko, G., Lane, T., 2009a, Compaction trends for shale and clean sandstone in shallow sediments, Gulf of Mexico: The Leading Edge, 28, 260-266.

Dutta, T., Mavko, G., and Mukerji, T., 2009b, Improved granular medium model for unconsolidated sands using coordination number, porosity and pressure relations: SEG Expanded Abstracts, 28.

Dvorkin, J. and A. Nur, 1996, Elasticity of high-porosity sandstones: Theory for two North Sea datasets: Geophysics, 61, 1363-1370.

Emery, D. and Myers, K., 1996, Sequence stratigraphy: Blackwell scientific publications, Inc.

Goddard, J.D., 1990, Nonlinear Elasticity and Pressure-Dependent Wave Speeds in Granular Media: Proceedings of the Royal Society of London. Series A, Mathematical and Physical Sciences, 430, 105-131.

Gonzalez, E., Mukerji, T., and Mavko, G., 2008, Seismic inversion combining rock physics and multiple-point geostatistics: Geophysics, 73, R11-R21.

Gutierrez, M., 2001, Rock Physics and 3D Seismic Characterization of Reservoir Heterogeneities to Improve Recovery Efficiency, Ph. D. thesis, Stanford University.

Flórez-Niño, J.M, 2005, Integrating geology, rock physics, and seismology for reservoir quality prediction: Ph.D. thesis, Stanford University.

Han, D., 1986, Effects of Porosity and Clay Content on Acoustic Properties of Sandstones and Unconsolidated Sediments, Ph. D. thesis, Stanford University.

Kupecz, J. A., J. C. Gluyas and S. Bloch, 1997, Reservoir Quality Prediction in Sandstones and Carbonates, American Association of Petroleum Geologist Memoirs, 69.

Makse, A., N. Gland, D. Johnson, and L. Schwartz, 2004, Granular packings: Nonlinear elasticity, sound propagation, and collective relaxation dynamics: Phys. Rev. E 70, 061302.

Marion, D., 1990, Acoustical, Mechanical and Transport Properties of Sediments and Granular Materials, Ph. D. Thesis, Stanford University.

Marion, D., Nur, A., Yin, H., and Han, D., 1992, Compressional velocity and porosity in sand-clay mixtures, Geophysics, 57, 554-563.

Mavko, G., and Jizba, D., 1991, Estimating grain-scale fluid effects on velocity dispersion in rocks, Geophysics, 56, 1155-1164.

Mavko, G., and Mukerji, T., 1998, A rock physics strategy for quantifying uncertainty in common hydrocarbon indicators: Geophysics, 63, 1997-2008.

Mavko, G., T. Mukerji and J. Dvorkin, 1998; The Rock Physics Handbook: Tools for Seismic Analysis in Porous Media, Cambridge University press, New York, 329 pp.

Mitchum, R. M. Jr., P. R. Vail and S. Thompson III, 1977, Seismic stratigraphy and global changes of sea level, part II: The depositional sequence as a basic unit for stratigraphic analysis, In: Payton, Ch. ed., Seismic Stratigraphy: Applications to Hydrocarbon Exploration, American Association of Petroleum Geologists Memoirs, 26, 53-62.

Murphy, W. F., III, 1982, Effects of Microstructure and Pore Fluids on the Acoustic Properties of Granular Sedimentary Materials, Ph. D. dissertation, Stanford University.

Neidell, N., J. H. Beard and E. Cook, 1985, Use of seismic-derived velocities for stratigraphic exploration on land: Seismic Porosity and Direct Gas Detection, In: Berg,O. R. and D. Woolverton, eds., Seismic Stratigraphy II: An Integrated Approach to Hydrocarbon Exploration, American Association of Petroleum Geologists Memoirs, 39, 49-77.

Nur, A., Marion, D., and Yin, H., 1991, Wave velocities in sediments, in Hovem, J.M., M. D. Richardon and R. D. Stoll, eds., Shear Waves in Marine Sediments, Kluwer Academic Publishers, Dordrecht, The Netherlands, 131-140.

Nur, A., Mavko, G., Dvorkin, J., and Gal, D., 1995, Critical porosity: The key to relating physical properties to porosity in rocks, in Proceedings, 65th Annual International Meeting, Soc. Expl. Geophys., 878.

Payton, C. E. ed., 1977, Seismic Stratigraphy: Applications to Hydrocarbon Exploration, American Association of Petroleum Geologists Memoirs, 26.

Peikert, E. W., 1985, Stratigraphic velocity interpretation: National Petroleum Reserve-Alaska, In: Berg, O. R. and D. Woolverton, eds., Seismic Stratigraphy II: An Integrated Approach to Hydrocarbon Exploration, American Association of Petroleum Geologists Memoirs, 39, 209-222.

Pettingill, 1998, Turbidite giants – lessons from the world's 40 largest turbidite discoveries: EAGE/AAPG 3rd Research Symposium on Developing and Managing Turbidite Reservoirs, Almeria, Expanded Abstracts, A027.

Posamentier, H. W, and Weimer, P., 1993. Siliciclastic sequence stratigraphy and petroleum geology — where to from here? American Association of Petroleum Geologists Bulletin, 77, 731–742.

Sheriff, R., and L. P. Geldart, 1995, Exploration Seismology, 2nd edition, Cambridge University Press, 520 pp.

Sloss, L. L., 1963, Sequences in the cratonic interior of North America, Geological Society of America Bulletin, 74, 93-113.

Takahashi, I, 2000, Quantifying information and uncertainty of rock property estimation from seismic data: Ph.D. thesis, Stanford University.

Tyler, N., and Finley, R. J., 1991, Architectural controls on the recovery of hydrocarbons from sandstone reservoirs: in Miall, A. D., and Tyler, N., Eds., Three-dimensional facies architecture of terrigenous clastic sediments and its implications for hydrocarbon discovery and recovery: Soc. Sed. Geol., 1-5.

Walton, K., 1987, The effective elastic moduli of a random pack of spheres: J. Mech. Phys. Sol., 35, 213-226.

Weimer, P., and Link, M.H., eds., Seismic facies and sedimentary processes of submarine fans and turbidite systems: New York, Springer-Verlag, 447 pp.

Weimer, P., and R. M. Slatt, 2004, The Petroleum Systems of Deep-Water Settings: SEG Distinguished Instructor Short Course Notes, 488 pp.

Weimer, P., Slatt, R. M., Dromgoole, P., Bowman, M., and Leonard, A., 2000, Developing and managing turbidite reservoirs: Case histories and experiences: Results of the 1998 EAGE/AAPG Research Conference: AAPG Bulletin, 84, 453-465.

Yin, H., 1992, Acoustic Velocity and Attenuation of Rocks: Isotropy, Intrinsic Anisotropy, and Stress-Induced Anisotropy, Ph. D. thesis, Stanford University.

Zeng, H., Ch. Kerans, and S. Ruppel, 2003, Integrating Detailed Stratigraphic Architecture with 3D Seismic for High-resolution Reservoir Modeling, American Association of Petroleum Geologists Meeting, Abstracts.

Zimmer, M., 2003, Controls on the Seismic Velocities of Unconsolidated Sands: Measurements of Pressure, Porosity and Compaction Effects, Ph. D. dissertation, Stanford University.

Chapter 2
Workflow to Integrate Sequence-stratigraphy and Rock physics

"In questions of science, the authority of a thousand is not worth the humble reasoning of a single individual."
--Galileo Galilei

2.1 Abstract

We present a workflow to integrate sequence stratigraphy and rock physics for quantitative interpretation of seismic amplitudes in terms of underlying reservoir properties, away from well locations. First, we use sequence stratigraphic interpretations to obtain critical sedimentological parameters that affect seismic amplitudes and identify the predictable trends of their relative spatial variations. Next, these spatial trends are used to constrain rock physics models and their input parameters away from the wells. Finally, we use the effective elastic moduli from rock physics modeling to compute forward seismic response (e.g., AVO attributes). We apply this workflow to quantify sorting trends in progradational lobes of a submarine fan system from the Campos Basin, Brazil. We use the sorting trends as predicted by the sequence stratigraphic

interpretations to constrain rock physics modeling away from the wells and generate AVO attributes. We obtain a distinct trend of variation in sorting and porosity from landward to basinward in the AVO intercept-gradient plane. These trends can serve as a template to guide the interpretation of observed intercept and gradient away from the wells. Since these trends incorporate the information from sequence stratigraphy, they can be used to predict the spatial variation in reservoir properties. In addition to the qualitative trend interpretation, we can now make quantitative interpretations about porosity and sorting based on the calibrated rock physics model.

2.2 Introduction

Sequence stratigraphy is a useful exploration tool for oil and gas as well as a production tool for reservoir development (Mulholland, 1998). It can predict the likely occurrence of reservoir facies, source rocks, and seals. Conventional sequence stratigraphic interpretation from seismic data has been predominantly qualitative, based on visual inspection of geometric patterns in post-stack seismic reflection data (Payton, 1977; Neal and Vail, 1993; Brown, 1996; Zeng et al., 1996). However, quantitative interpretation of seismic amplitudes is possible if we can extract information about mineralogical composition (e.g., quartz/clay ratio) and textural maturity (e.g., sorting, grain angularity, sphericity and roundedness) using principles of sedimentology.

Quantitative seismic interpretation uses rock physics to link seismic amplitude with reservoir properties such as porosity, clay-content, sorting and diagenetic cements (e.g., (Latimer et al., 2000; Castagna, 2001; Gutiérrez et al., 2001; Walls et al., 2002; Florez, 2005; Avseth et al., 2005; Braaksma et al., 2006). In quantitative seismic interpretation, model parameters are calibrated at well locations. However, one of the major sources of uncertainty in rock physics modeling arises from our lack of knowledge about trends of input parameters away from wells. This uncertainty can be reduced by constraining input parameters (for example, sand/shale ratio and textural maturity) as guided by sequence stratigraphic framework. Therefore, the reservoir property prediction from seismic amplitudes will benefit from close coupling between sequence stratigraphy and rock

physics.

In this chapter, we present a workflow to integrate sequence stratigraphy and rock physics. Specifically, we demonstrate how we can obtain spatial variations of sedimentological parameters from sequence stratigraphic interpretation for constraining rock physics model parameters. We then apply this technique to obtain sorting trends in progradational lobes deposited in a submarine fan, and use the trends to constrain rock physics modeling and compute AVO attributes.

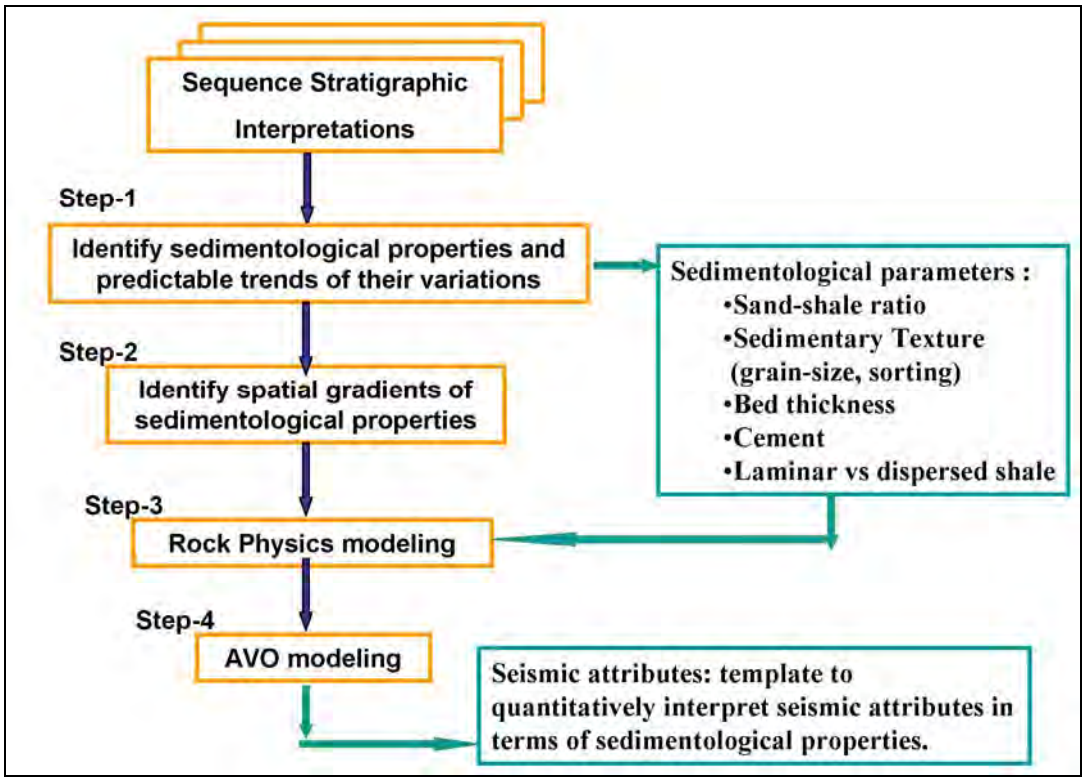

Figure 2.1: The schematic diagram describing our workflow to integrate sequence stratigraphy and rock physics for quantitatively interpreting seismic attributes in terms of sedimentological properties.

2.3 Methodology

In this section, we present a workflow to integrate sequence stratigraphy and rock physics for quantitative interpretation of seismic amplitudes in terms of underlying reservoir properties, away from well locations. The key steps are summarized in Figure

2.1, and are discussed as follows.

Step 1: Identify sedimentological properties and predictable trends of their variations

Van Wagoner et al. (1990) showed that transgression and regression cause predictable trends in sedimentological properties, such as sand-shale ratio, bed thickness, grain size, sorting, and bioturbation. Interestingly, the changes in these sedimentological properties have opposite trends for transgression and regression (Figure 2.2). During regression depositional energy generally tends to increase upward, resulting in increased bed thickness, higher sand-shale ratio, better sorting, and decrease in bioturbation. In contrast, a marine transgression signifies a general decrease in depositional energy and exhibits an opposite trend of the above sedimentological properties. We use quartz-clay ratio and sorting as indicators of mineralogical composition and textural maturity, respectively. If the rock undergoes longer transportation from the source area, usually the quartz-clay ratio increases. In addition, the grains tend to be better sorted, more rounded, and less angular. As a result, textural maturity increases with longer transportation history of the sedimentary grains. The mineralogical composition and textural maturity constitute important sedimentological properties that affect the elastic stiffness of the rocks and in turn affect seismic amplitudes.

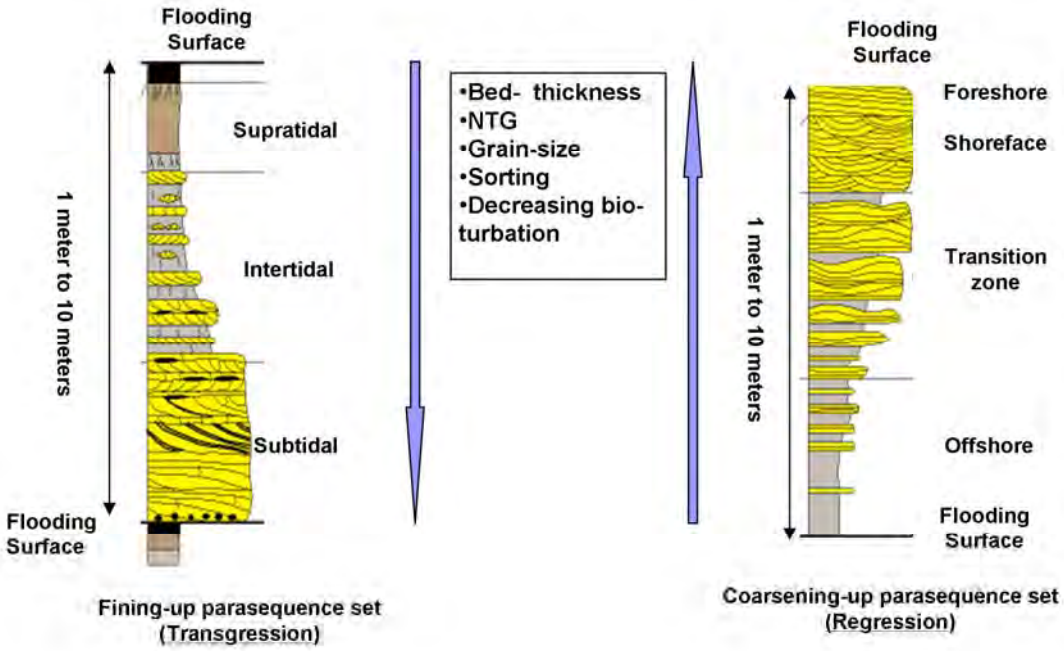

Figure 2.2: Vertical profile of sedimentological parameters from sequence stratigraphy. Transgression and regression exhibit opposite trends (modified from Van Wagoner et al., 1990).

The trends of sedimentological properties are more robust in shallow marine and marginal marine environments since sediments are deposited at or near sea level, and therefore, are sensitive to changes in relative sea level. The sediment delivery processes and tectonic settings in a deepwater system are quite different from the shallow and marginal marine environments, and may not be sensitive to changes in relative sea level (Emery and Myers, 1996). However, we can still benefit by applying sequence stratigraphy other than shallow marine and the m marine environments (Posamentier and Weimer, 1993). Core descriptions and thin sections, if available, are useful to validate or modify the trends of sedimentological properties.

Step 2: Identify spatial gradients of sedimentological properties

Gradients of sediment parameters are not the same perpendicular to the seismic reflector and parallel the reflector. Most seismic reflectors and their amplitudes

correspond to chronostratigraphic surfaces (Tipper, 1993). The exceptions are the seismic reflectors caused by multiples, fluid contacts, and diagenetic boundaries, which all lack chronostratigraphic significance. Chronostratigraphic surfaces represent depositional hiatus, which is defined as a gap in the sedimentation record due to erosion or non-deposition. Changes in sedimentological properties are abrupt across the hiatus and gradual along the hiatus (Figure 2.3).

The vertical gradients of sediment parameters are calibrated from well data. The estimation of lateral gradients requires multiple wells or horizontal wells. In the absence of such data, we can assume that the lateral gradient of sediment parameters is linear. However, these trends are specific to parasequence and parasequence sets, and parasequences are identified from sequence stratigraphic interpretation. Thus, using sequence stratigraphy, we obtain relative trends of variation in sediment properties within a depositional sequence. These trends then constrain the input parameters in rock physics modeling.

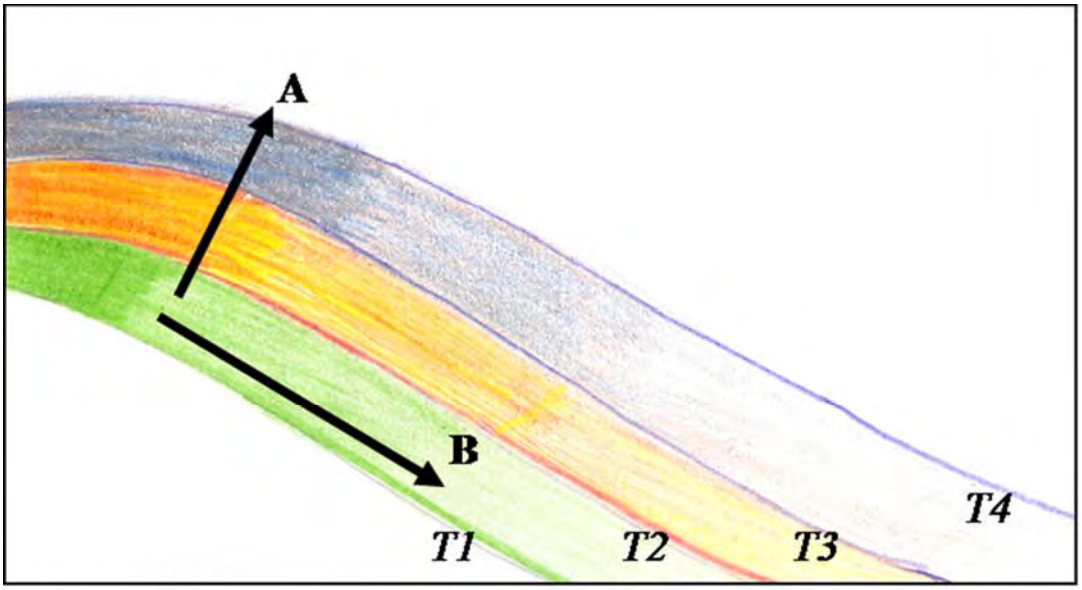

Figure 2.3: T1, T2, T3 and T4 are chrono-stratigraphic surfaces (hiatus), and seismic reflectors usually follow the chrono-stratigraphic surfaces. The gradation in color represents changes in sedimentological properties. The changes in sedimentological properties are abrupt across the hiatus (Trend A) and gradual along the hiatus (Trend B). This figure has been modified from Emery and Myers (1996).

Step 3: Rock physics modeling

Rock physics establishes the relationship between sedimentological properties and elastic moduli. After we determine the spatial trends of sediment parameters in a depositional sequence, appropriate rock physics models are selected. The input parameters are guided by our results from steps 1 and 2. The rock physics models are calibrated to well-log data. As output we obtain effective bulk modulus, shear modulus, density, V_P, and V_S as functions of porosity.

Step 4: AVO modeling

AVO forward modeling (Shuey, 1985) is used to obtain intercept and gradient at key stratigraphic interfaces using effective moduli predicted from rock physics analysis in step 3. Trends in textural maturity are carried through from sequence stratigraphy to the AVO plane, via rock physics. Finally, the modeling results can be used to interpret amplitudes in terms of sedimentological properties and reservoir quality.

2.4 Example from Campos Basin, Offshore Brazil

2.4.1 Depositional setting

We applied the above workflow using well logs and 3D seismic data from Campos Basin, offshore Brazil. The facies package was deposited in a deep-water turbidite system (Peres, 1990). Although submarine fans can be deposited at any time, they are most likely to be deposited during lowstand (Posamentier and Vail, 1988). Figure 2.4 shows the geometry and truncation patterns of seismic reflectors in the submarine fan. The stacking patterns in well logs are shown in Figure 2.5. In this submarine fan system, unchannelized depositional lobes show a porosity profile that increases upward.

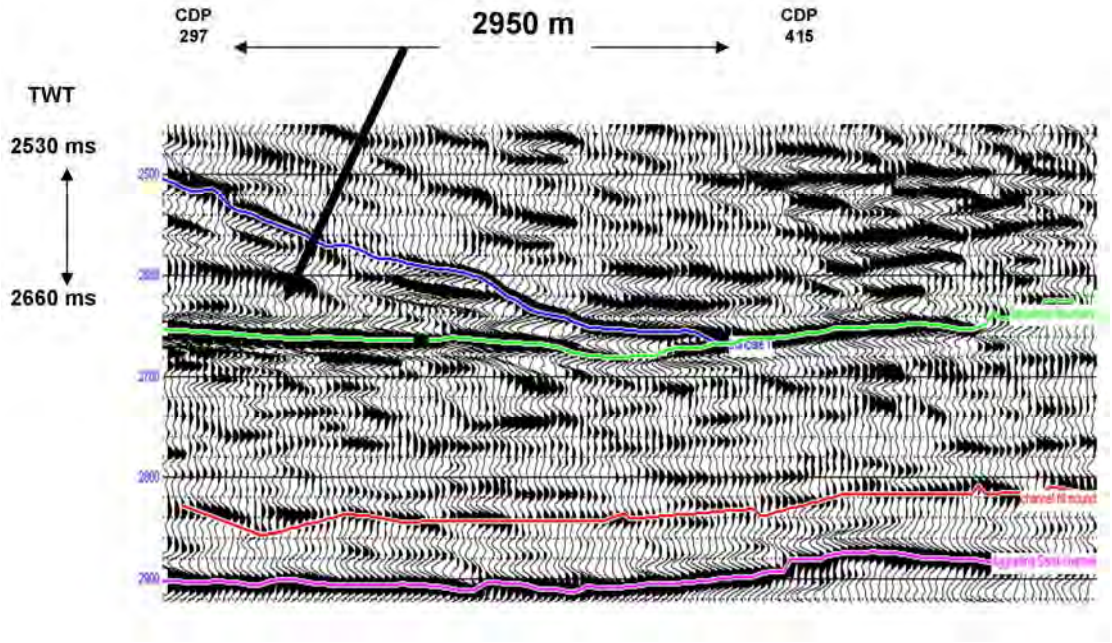

Figure 2.4: Seismic section showing geometry and truncation patterns of reflectors. The arrow indicates a submarine fan system.

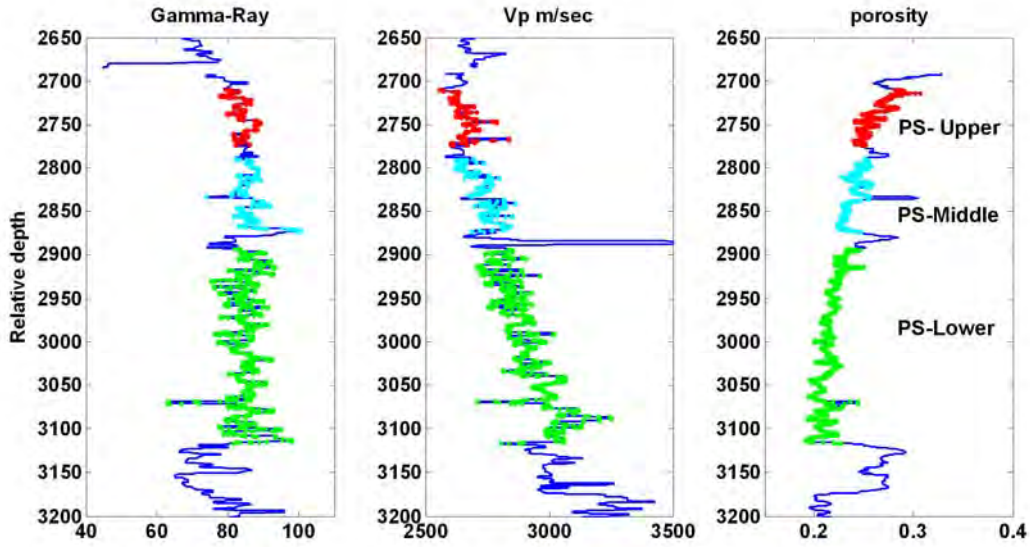

Figure 2.5: Well logs with three parasequences (PS) within progradational depositional lobes. The upper, middle and lower PS are highlighted in red, blue, and green, respectively. A trend of increasing porosity is observed from lower-PS to upper-PS.

2.4.2 Sorting trend in prograding depositional lobes

We interpret three parasequences (PS) within the prograding depositional lobes in our study area (Figure 2.6). Sakai and Masuda (1996) applied the parasequence concept to deep-water turbidite system. By definition, a parasequence is a deposit of a paracycle (Van Wagoner et al., 1988; Kamola and Van Wagoner, 1995), and represents a relatively conformable succession of genetically related beds or bedsets bounded by flooding surfaces or their correlative surfaces (Van Wagoner et al., 1988). We use the interpreted parasequences for applying sequence stratigraphic principles to obtain the relative sorting trend. Sorting is an important indicator of textural maturity, and controls porosity and seismic velocities. Poor sorting decreases porosity and increases the elastic moduli, and hence seismic velocities.

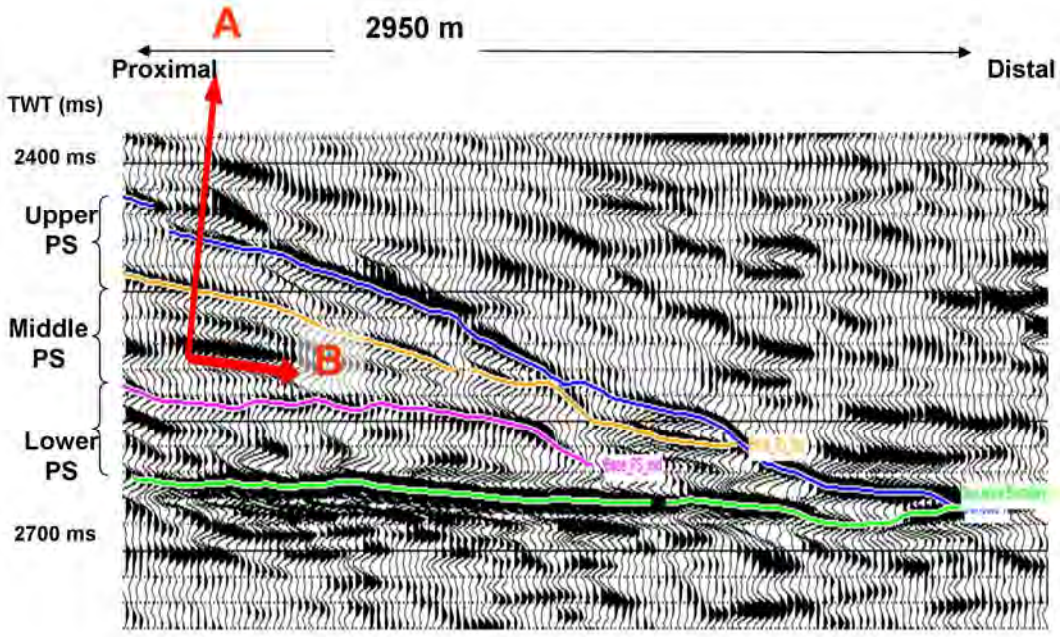

Figure 2.6: Three parasequences (PS) interpreted within progradational depositional lobes. The changes in sorting are abrupt across the para-sequence boundaries (Trend-A) and gradual along the boundaries (Trend-B).

We create the sorting trends as predicted by the sequence stratigraphic models from analog deepwater environments. The sequence stratigraphic model by Walker (1984) predicts that depositional energy in prograding depositional lobes increases vertically upward. We expect better sorting associated with higher depositional energy. Therefore,

we expect the lower PS to be very poorly sorted, the middle PS moderately sorted, and the upper one well sorted (Trend A, Figure 2.6). The Trend A of porosity at the proximal location is calibrated with well data. The mean porosities computed from well logs in the upper, middle, and lower PS are 26%, 23%, and 21% respectively. The porosity at the proximal location in each PS is assigned by this mean well-log porosity.

We compute the spatial trends of sorting using the sequence stratigraphic models of Piper (1978) and Stow and Bowen (1980). These models predict that sorting improves along the direction of sediment transport due to a slow process of segregation of silt particles from clay flocs. However, the exact functional form of the sorting trend (i.e., linear, quadratic, cubic, or something else) is uncertain. In this chapter, we assume that within each parasequence, sorting improves linearly parallel to the underlying parasequence boundary with an increase in Euclidean distance from the proximal to the distal location (Trend B, Figure 2.6). Additional data (such as multiple wells, horizontal wells or cores available at any parasequence) could have verified or modified these linear sorting trends. Such additional data are not available in the present study.

2.4.3 Relationship between sorting and porosity

We use an experimental sorting-porosity relationship for artificially mixed sand (Beard and Weyl, 1973; Jorden and Campbell, 1984). Figure 2.7 shows the range of porosities for different sorting and various sandstone grain sizes. Sorting is expressed in terms of the standard deviation of the distribution of the logarithm of the grain size. Figure 2.8 shows a plausible porosity section of progradational lobes. At the proximal location, the mean of porosities at each parasequence is calibrated from well logs. The lateral variation of sorting away from the well data is obtained from the trend predicted by sequence stratigraphy. The mean porosity at distal locations is selected using sorting-porosity relationship for medium sand-sized grains. The mean porosity at the distal location in upper PS (well sorted), middle PS (medium sorted), and lower PS (very poorly sorted) is 40%, 34%, and 26%, respectively. These values can be calibrated by porosities computed from deviated wells or additional wells at distal location. In our

study area, there is no well penetrating at the distal location.

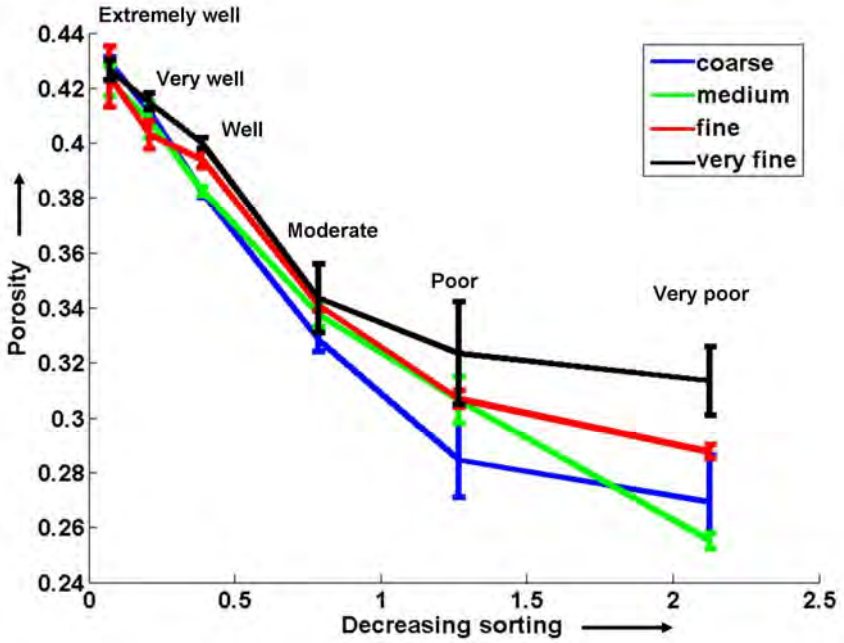

Figure 2.7: Porosity decreases with deteriorating sorting (Beard and Weyl, 1973; Jorden and Campbell, 1984). Different curves represent different grain sizes in sandstone. The solid lines indicate mean, and the bars indicate range in porosities at a particular sorting.

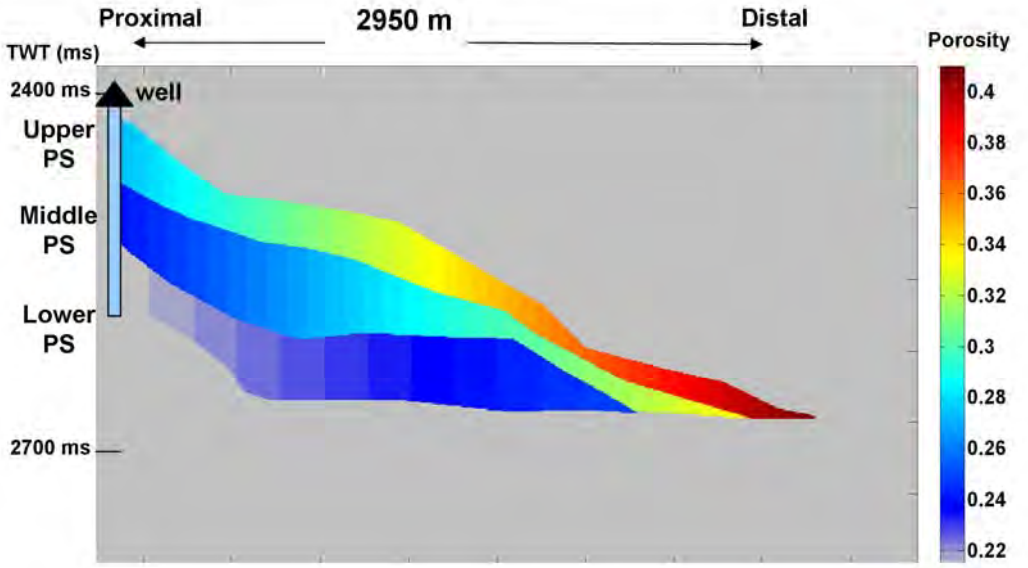

Figure 2.8: Porosity section in depositional lobes. At the proximal location porosities are obtained from well-logs. The lateral variations of porosity away from the well are predicted by sequence stratigraphy.

2.4.4 Selection of rock physics model and input parameters

The trends of the variations in sorting, obtained from sequence stratigraphy, guide us in selecting a rock physics model that accounts for sorting. The friable-sand model (Dvorkin and Nur, 1996; Mavko et al., 1998) can be used heuristically to compute elastic moduli of both well-sorted and poorly-sorted soft sands. This model is also referred to as the soft-sand model. The effective moduli at a well sorted, high-porosity end member (~40%) are computed using the Hertz-Mindlin contact theory.

The Hertz-Mindlin contact theory provides the following expressions for the bulk (K_{HM}) and shear (G_{HM}) moduli of a dense random pack of identical spherical grains subject to an effective pressure P (Mindlin, 1949; Mavko et al., 1998):

$$K_{HM} = \left[\frac{C^2(1-\phi_0)^2 G^2}{18\pi^2(1-\nu)^2} P\right]^{1/3} \tag{2.1}$$

$$G_{HM} = \frac{5-4\nu}{5(2-\nu)}\left[\frac{3C^2(1-\phi_0)^2 G^2}{2\pi^2(1-\nu)^2} P\right]^{1/3} \tag{2.2}$$

where ϕ_0 is the critical porosity (~40 % for sandstone), C is the coordination number (average number of grain contacts); G and ν are the mineral shear modulus and Poisson's ratio. The elastic moduli at a poorly sorted, zero porosity end member are given by the mineral moduli.

The effective elastic moduli of sand with porosities between 0 to critical porosity (~40%) are interpolated using the lower Hashin-Shtrikman bound. The effective bulk moduli (K_{eff}) and shear moduli (G_{eff}) are (Dvorkin and Nur, 1996; Mavko et al., 1998):

$$K_{eff} = \left[\frac{\phi/\phi_0}{K_{HM} + \frac{4}{3}G_{HM}} + \frac{1-\phi/\phi_0}{K + \frac{4}{3}G_{HM}}\right] - \frac{4}{3}G_{HM} \tag{2.3}$$

$$G_{eff} = \left[\frac{\phi / \phi_0}{G_{HM} + \frac{G_{HM}}{6} B} + \frac{1 - \phi / \phi_0}{G + \frac{G_{HM}}{6} B} \right] - \frac{G_{HM}}{6} B \qquad (2.4)$$

where K is the grain bulk modulus, and $B = \left(\frac{9K_{HM} + 8G_{HM}}{K_{HM} + 2G_{HM}} \right)$.

The heuristic argument of interpolation using the lower Hashin-Shtrikman bound (equations 2.3 and 2.4) is that adding small grains in the pore spaces adds minerals in a way that keeps the effective elastic moduli low, very close to the lower bound. The lower Hashin-Shtrikman bound is theoretically the lowest elastic stiffness possible for a mix of multiple phases.

Figure 2.9 shows porosities and velocities in three parasequences using well logs, and the velocities predicted by the friable sand model at different porosities. The well logs are the same as those shown earlier in Figure 2.5. We consider feldspar and clay along with quartz in the rock physics model for computing effective mineral moduli using the Voigt-Reuss-Hill average (Hill, 1952). The bulk and shear moduli of individual minerals are shown in Table 2.1. The coordination number is assumed to be 8 for well-sorted end members.

The velocity-porosity trends from well data are in good agreement with the friable-sand model predictions. The parallel lines in Figure 2.9 represent the model predictions for different mineralogical composition, i.e., different amount of quartz, feldspar, and clay. Increasing the amount of clay decreases the velocities. The stiff-sand model is suitable for cemented sands and does not capture the trends of these data. The friable sand model with 70% quartz, 20% feldspar, and 10% clay along with mean well-log porosity in each parasequence are used to compute the effective moduli at the proximal location. To model spatial variation of effective moduli, the porosity section from the sequence stratigraphic interpretation (Figure 2.8) is used as input to the calibrated rock physics model.

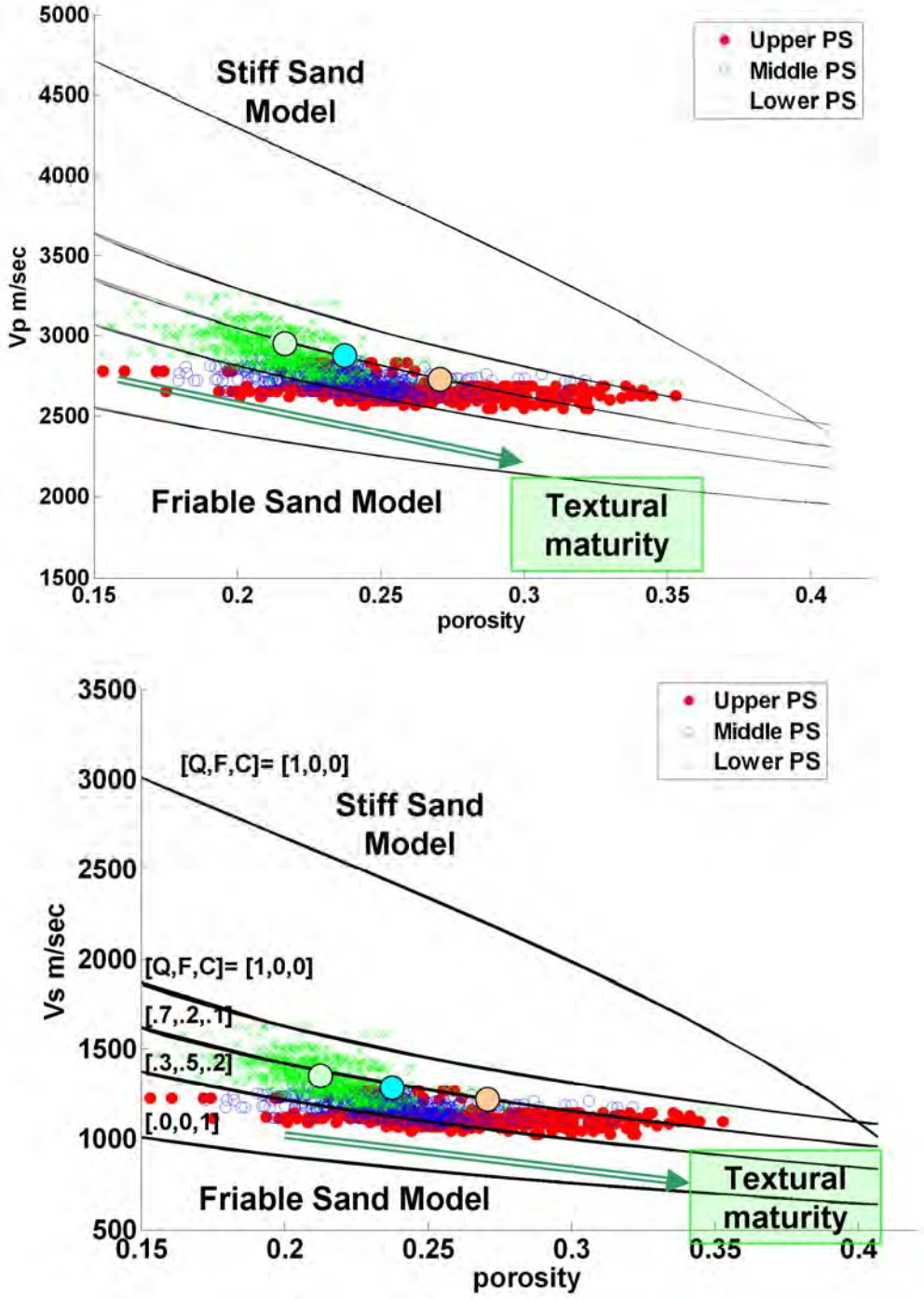

Figure 2.9: The scatter points show measurements of porosities and velocities from well logs in three parasequences of prograding lobes. The rock-physics model quantitatively explains the scatter in terms of sedimentological parameters. The friable sand model can be used to represent trend of sorting, an indicator of textural maturity. The solid circles represent mean porosities at proximal location for each parasequences and corresponding velocities obtained using the friable sand model.

Table 2.1: Bulk modulus, shear modulus and density of different minerals used in rock physics modeling.

Mineral	Bulk modulus (GPa)	Shear modulus (GPa)	Density (gm/cc)
Quartz	36.6	45	2.65
Feldspar	75.6	25.6	2.63
Clay	21	7	2.58

2.4.5 Modeling spatial AVO trend

The effective V_P, V_S, and density are used to compute intercept and gradient at the interfaces of the three parasequences using a simplified form of Zeoppritz equation by Shuey (1985). According to Shuey's two-term approximation, the intercepts (R_0) and the gradients (G) are:

$$R_0 = \frac{1}{2}\left(\frac{\Delta V_P}{\overline{V}_P} + \frac{\Delta\rho}{\overline{\rho}}\right) \tag{2.5}$$

$$G = \left(ER_0 + \frac{\Delta\nu}{\overline{\nu}}\right) \tag{2.6}$$

where

$$E = F - 2(1+F)\left(\frac{1-2\overline{\nu}}{1-\overline{\nu}}\right) \tag{2.7}$$

$$F = \frac{\Delta V_P / \overline{V}_P}{\Delta V_P / \overline{V}_P + \Delta\rho / \overline{\rho}} \tag{2.8}$$

$$\Delta V_P = V_{P2} - V_{P1},\ \Delta\rho = \rho_{P2} - \rho_{P1},\ \Delta\nu = \nu_{P2} - \nu_{P1} \tag{2.9}$$

$$\overline{V}_P = (V_{P2} + V_{P1})/2,\ \overline{\rho} = (\rho_{P2} + \rho_{P1})/2,\ \overline{\nu} = (\nu_{P2} + \nu_{P1})/2 \tag{2.10}$$

We obtain a distinct trend of variation in porosity from landward to basinward in the R_0-G plane (Figure 2.10). These trends can serve as a template to guide the interpretation of observed intercept and gradient away from the well data. Since these trends incorporate the information from sequence stratigraphy, they can be used to

predict the spatial variation in reservoir properties. We can now make quantitative interpretations about porosity and sorting based on the calibrated rock physics model in addition to the qualitative trend interpretation.

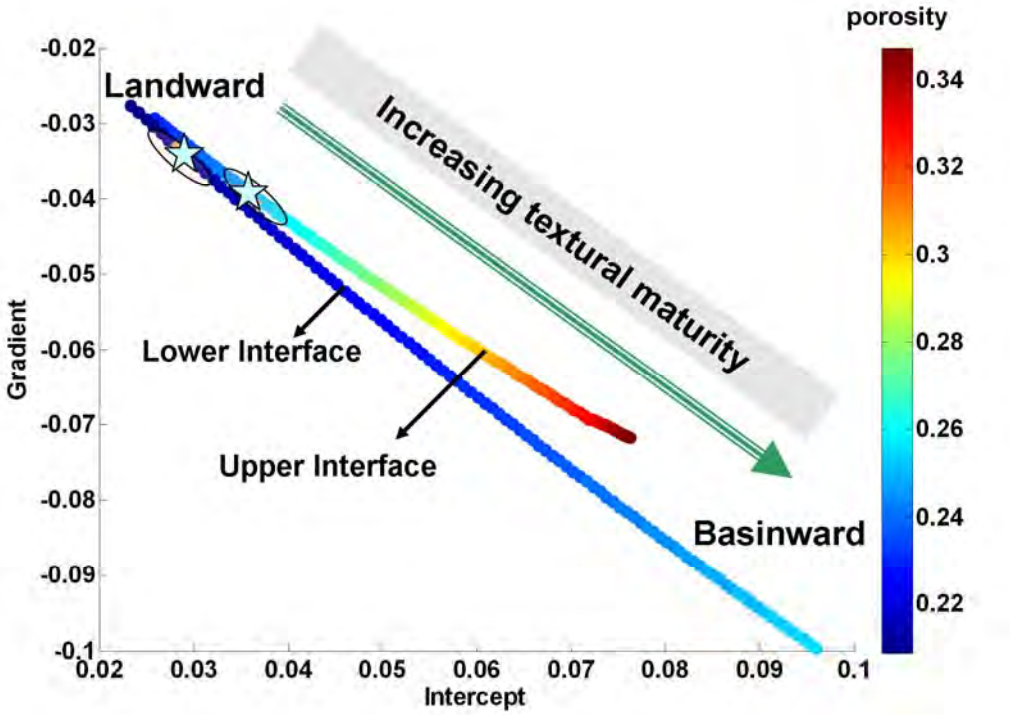

Figure 2.10 AVO modeling results: Intercept (R_0) and Gradient (G) crossplot color-coded by porosity. They indicate distinct trend of variation in textural maturity from landward to basinward. The 'stars' indicate mean of R_0 and G computed from neighboring well logs at proximal location. The ellipses around the mean values emphasizes that there will be scatter for real data.

2.5 Discussion and Conclusions

We have developed a workflow for using spatial trends of sedimentological parameters from sequence stratigraphic interpretations as constraints in rock physics modeling away from well locations. These trends are relative within a stratigraphic sequence. We have applied this method to estimate trends of sorting or grain-size variation in prograding lobes of a submarine fan in the Campos Basin, Brazil. Rock physics modeling was constrained using trends of grain sorting as guided by sequence stratigraphic interpretations.

The effective moduli computed from rock physics modeling were used to generate AVO attributes at two parasequence boundaries. In the R_0-G plane, we obtain a linear trend of variation in sediment properties from landward to basinward. The trend approximates the mean of a probability distribution of sedimentological properties. Geologic variability will add scatter around this trend. Textural maturity progressively increases along this trend basinward. Furthermore, since these trends are calibrated with the rock physics model it is possible to make quantitative interpretations about porosity and sorting. For example mean porosity is predicted to progressively change from ~24% to ~34% and ~22% to ~27% along the upper and lower interfaces, respectively.

There is uncertainty in our linear sorting trend since lobe-switching in the submarine fan will complicate the predictive power of the sequence stratigraphic model. Further developments to this workflow will include (1) consideration of multiple sequence stratigraphic models, and (2) calibrating the trends of sediment parameters from multiple well logs, core descriptions, thin sections, and grain-size analysis data, and (3) including uncertainty in the trends.

The workflow developed in this chapter allows us to constrain rock physics modeling, away from well locations, using spatial trends of sedimentological parameters from sequence stratigraphic interpretations. The direct advantage of integrating sequence stratigraphy and rock physics is that seismic attributes (e.g., intercept, gradient) can be quantitatively interpreted in terms of underlying sedimentological properties.

2.6 Acknowledgements

This work was supported by the Stanford Rock Physics and Borehole Geophysics (SRB) project and by DOE awards DE-FC26-04NT15506 and DE-FG02-03ER15423. We acknowledge Norsk Hydro and Fugro for permission to use data from the Campos basin. We also thank Per Avseth for arranging to get the data, and for valuable discussions.

2.7 References

Avseth, P., Mukerji, T., and Mavko, G., 2005, Quantitative Seismic Interpretation: Applying Rock Physics Tools to Reduce Interpretation Risk: Cambridge University Press.

Beard, D. C., and Weyl, P. K., 1973, Influence of texture on porosity and permeability of unconsolidated sand: American Association of Petroleum Geologists Bulletin, 57, 349-369.

Braaksma,H., Kenter, J.A.M., Proust, J.N., Dijkmans, V., Hoek, T.V. and Drijkoningen, G.G., 2002, Controls on acoustic properties of upper siliciclastic rocks (Boulonnais, northern France): Geophysics, 68, 58-69.

Brown, A. R., Wright, R. M., Burkhart, K. P., and Abriel, W. L., 1984, Interactive seismic mapping of net producible gas sand in the Gulf of Mexico: Geophysics, 49, 686-714.

Castagna, J.P., 2001, Recent advances in seismic lithologic analysis: Geophysics, 66, 42-46.

Dutta, T., Mukerji, T., Mavko, G., and Avseth, P., 2006, Reservoir quality prediction by integrating sequence stratigraphy and rock physics: SEG Expanded Abstracts, 25, 1811-1815.

Dutta, T., Mukerji, T., and Mavko, G., 2007, Rock physics modeling constrained by sequence stratigraphy: The Leading Edge, 26, 870.

Dvorkin, J., and Nur, A., 1996, Elasticity of high-porosity sandstones: Theory for two North Sea datasets: Geophysics, 61, 1363-1370.

Emery, D., and Myers, K., 1996, Sequence stratigraphy: Blackwell scientific publications, Inc.

Florez, J.M., 2005, Integrating geology, rock physics, and seismology for reservoir-quality prediction: Ph.D. Thesis, Stanford University.

Galloway, W.E., 1989, Genetic stratigraphic sequences in basin analysis I: Architectures and genesis of flooding-surface bounded depositional units: American Association of Petroleum Geologists, Bulletin, 73, 125–142.

Gutierrez, M., 2001, Rock physics and 3-D seismic characterization of reservoir heterogeneities to improve recovery efficiency: Ph.D. thesis, Stanford University.

Hill, R., 1952, The elastic behavior of crystalline aggregate: Proc. Phys. Soc., London A, 65, 349-354.

Jorden, J. R., and Campbell, F. L., 1984, Well Logging I - rock properties, borehole environment, mud and temperature logging: Society of Petroleum Engineers (SPE) of American Institute of Mining, Metallurgical and Petroleum Engineers (AIME).

Kamola, D.L., and Van Wagoner, J.C., 1995, Stratigraphy and facies architecture of parasequences with examples from the Spring Canyon Member, Blackhawk Formation, Utah. In: J.C. Van Wagoner and G.T. Bertram (Editors), Sequence Stratigraphy of Foreland Basin Deposits - Outcrop and Subsurface Examples from the Cretaceous of North America, Am. Assoc. Pet. Geol. Mem., 64, 27-54.

Latimer , R.B., 2000, An interpreter's guide to understanding and working with seismic-derived acoustic impedance data: The Leading Edge, 19, 242-256.

Mavko, G., Mukerji, T., and Dvorkin, J., 1998, The Rock Physics Handbook, tools for seismic analysis in porous media: Cambridge University press.

Mindlin, RD, 1949, Compliance of elastic bodies in contact: ASME Journal of Applied Mechanics, 71, A-259 -268.

Mulholland, J.W., 1998, Sequence stratigraphy: basic elements, concepts and terminology: The Leading Edge, 17, 37-40.

Neal, J., Risch, D. and Vail, P., 1993, Sequence stratigraphy- a local theory with global success: Oilfield review, 51-62.

Neidall, S., Beard, J.H. and Cook, E., 1985, Use of seismic derived velocities for stratigraphic exploration on Land: Seismic porosity and direct gas detection: Seismic Stratigraphy II, AAPG Memoir, 39, 49-77.

Payton, C.E., 1977, Seismic stratigraphy- applications to hydrocarbon explorations: AAPG Memoir, 26, The American association of petroleum geologists, 516.

Peres, W.E., 1990, Seismic-stratigraphic study of the Oligocene-Miocene shelf-fed turbidite systems of the Campos Basin, Brazil: Ph.D. thesis, The University of Texas at Austin.

Piper, DJW., 1978, Sedimentation in Submarine Canyons, Fans and Trenches: Turbidite muds and silts on deepsea fans and abyssal plains.

Posamentier, H. W, and Weimer, P., 1993. Siliciclastic sequence stratigraphy and petroleum geology — where to from here? American Association of Petroleum Geologists Bulletin, 77, 731–742.

Sakai, T. and Masuda, F., 1996, Slope turbidite packets in a fore-arc basin fill sequence of the Plio-Pleistocene Kakegawa Group, Japan: their formation and sea-level changes: Sedimentary Geology, 104, 89-98.

Shuey, R. T., 1985, A simplification of the Zoeppritz-equations: Geophysics, 50, 609-614.

Stow, D.A.V., Bowen, A.J., 1980, A physical model for the transport and sorting of fine-grained sediment by turbidity currents: Sedimentology, v. 27, 31-46.

Tipper, J.C., 1993, Do seismic reflections necessarily have chronostratigraphic significance: Geol. Mag. 130, 47-55.

Van Wagoner, J.C., Posamentier, H.W., Mitchum, R.M., Vail, P.R., Sarg, J.F., Loutit, T.S. and Hardenbol, J., 1988, An overview of the fundamentals of sequence stratigraphy and key definitions. In: C.K. Wilgus, B.S. Hastings, C.G.St.C. Kendall, H.W. Posamentier, C.A. Ross and J.C. Van Wagoner (Editors), Sea-Level Changes: An Integrated Approach, Soc. Econ. Paleontol. Mineral., Spec. Publ., 42, 39-45.

Van Wagoner, J.C., Mitchum, R.M., Campion, K.M., and Rahmanian, V.D., 1990, Siliciclastic sequence stratigraphy in well logs, cores and outcrops: The American Association of Petroleum Geologists, Methods in Exploration Series, no. 7.

Walker, R G., 1984, Turbidites and associated coarse clastic deposits in Facies models: Geoscience Canada Reprint Series 1,317 p.

Walls, J. D., Taner, M. T., Taylor, G., Smith, M., Carr, M., Derzhi, N., Drummond, J., McGuire, D., Morris, S., Bregar, J. and Lakings, J., 2002, Seismic reservoir characterization of a U.S. Midcontinent fluvial system using rock physics, poststack seismic attributes, and neural networks: The Leading Edge, 21, 428-436

Zeng, H., Beckus, M.M., Barrow, K.T and Tyler, N., 1996, Facies mapping from three dimensional seismic data: potential and guidelines from a tertiary sandstone-shale sequence model, Powderhorn field, Calhoun Country, Texas: AAPG Bulletin, 90, 16-46.

Chapter 3
Improved Granular Medium Model for Unconsolidated Sands Using a Coordination Number, Porosity, and Pressure Relation

"It doesn't matter how beautiful your theory is, it doesn't matter how smart you are. If it doesn't agree with experiment, it is wrong."
--Richard Feynman

3.1 Abstract

We present a recipe for using closed-form expressions of effective-medium models to predict velocities in unconsolidated sandstones. The commonly used Hertz-Mindlin effective-medium model for granular media often predicts elastic wave velocities that are higher, and V_P/V_S ratios that are lower, than those observed in laboratory and well log measurements in unconsolidated sediments. We use the extended Walton model, which introduces a parameter α to represent the fraction of grain-contacts that are perfectly

adhered. Using the extended Walton model with α ranging from 0.3 to 1, we obtain new empirical relations between coordination number (C), porosity, and pressure for P- and S-wave velocities by inverting dynamic measurements on dry, unconsolidated sands. We propose using the extended Walton model (α=0.6) along with these new C-porosity, and C-pressure relations for studying mechanical compaction of unconsolidated sandstones. The proposed model has been tested on two different experimental data sets. It provides a reasonable fit to observed P- and S-wave velocities, and specifically improves shear-wave predictions.

3.2 Introduction

Understanding seismic velocities of unconsolidated granular materials is important for interpreting acoustic measurements in sediments in the shallow subsurface. Although laboratory ultrasonic measurements have been conducted in such materials (Domenico, 1977; Yin, 1992; Estes et al., 1994; Zimmer, 2003), and various theoretical models have been developed (see overview in Wang and Nur, 1992), the discrepancy between measured and theoretical values of velocities remains a long-standing question.

Theoretical models for the elasticity of granular materials, such as the Hertz-Mindlin model (Mindlin, 1949), are based on rigorous calculation of the normal and shear contact stiffnesses of two elastic spherical grains in contact. The effective elastic moduli of the granular assembly are then estimated by taking averages of contact forces corresponding to an assumed distribution of strain over all the contacts (e.g., Walton, 1987). This is often referred to as an effective-medium approximation (EMA), where strain is usually assumed to be homogenous at the scale of the representative elementary volume of the sample. A notable exception is the work by Jenkins et al. (2005), which allows local non-homogenous strains. Laboratory experiments on isotropic compression of a granular assembly of spheres demonstrate that the measured dynamic bulk and shear moduli vary with confining pressure faster than the 1/3 power law predicted by the Hertz-Mindlin effective-medium model (Goddard, 1990; Zimmer, 2003). In addition, the observed V_P/V_S ratios are significantly higher than those predicted by most of the effective-

medium models.

Figure 3.1 shows the discrepancy between the velocities and the V_P/V_S ratio measured by Zimmer (2003) and those predicted by the Hertz-Mindlin effective-medium model. The model over-predicts V_S, and underpredicts V_P/V_S ratio. In this modeling, we used mineral moduli as shown in Table 3.2, and coordination number-porosity relation given by Murphy, 1982. The velocity data in Figure 3.1 represents envelop obtained from several loading cycles, and approximately corresponds to virgin compaction trends. These loading cycles are shown in Figure 3.2.

Several authors have tried to explain the discrepancies between measured data and EMT predictions. DeGennes (1996) suggested that the Hertz force model is not valid in granular media. However, other authors (e.g., Coste and Gilles, 1999) have experimentally confirmed the validity of the Hertz single-contact model. Makse et al. (1999, 2004) performed molecular dynamics simulations and concluded that the biggest error arises from the homogenous strain approximation usually adapted in EMA. They suggest that the assumption of homogenous strain is approximately valid for understanding the bulk modulus, but is seriously flawed for shear modulus. The coordination number-porosity relation from such simulations (e.g., Makse et al., 2004; Garcia et al., 2004; Garcia and Medina, 2006) usually predicts a lower coordination number than Murphy's empirical relation (Murphy, 1982). Granular dynamic numerical simulations demand significant computational time and resources, especially for large aggregates of grains. In addition, they lack the convenience for closed-form expressions for computing effective elastic moduli.

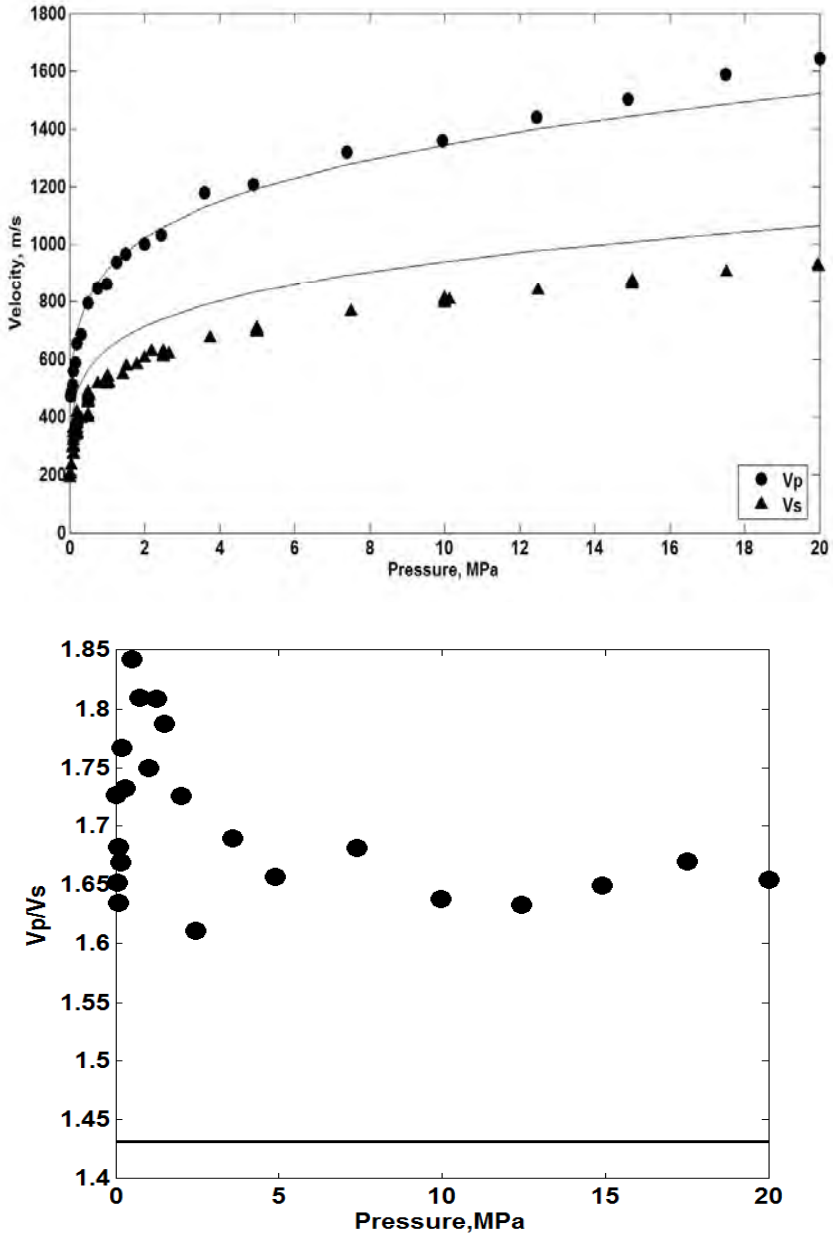

Figure 3.1: Top: velocities vs. pressure. Bottom: V_P/V_S ratio vs. pressure. The velocities and V_P/V_S ratio are measured by Zimmer (2003) on dry, unconsolidated sandstones (from Pomponio beach, California). The data shown in plot are selected from the loading cycles of the experiments (see Figure 3.2). The solid lines show the predictions of velocities by the Hertz-Mindlin contact model using the coordination number-porosity relation given by Murphy (1982). The model over-predicts V_S (top), and under-predicts V_P/V_S ratio (bottom).

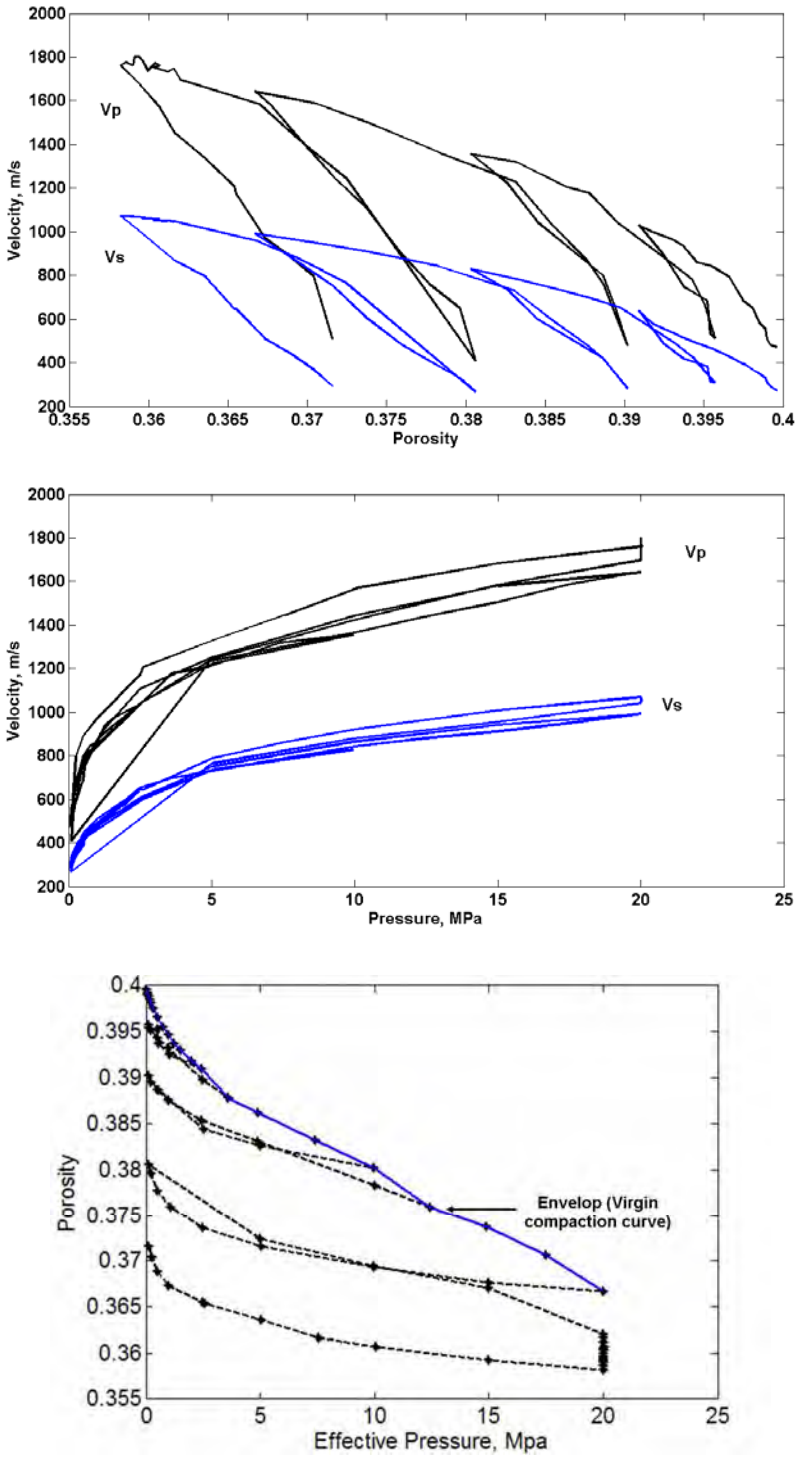

Figure 3.2: Loading cycles in Pomponio beach sample measured by Zimmer (2003). Top: velocities vs. porosity. Middle: velocities vs. pressure. Bottom: pressure vs. porosity. The computed envelop is shown as the blue line.

Our approach is to develop a practical recipe with the convenience of closed-form expressions in an effective-medium granular model, and combine that model with an appropriate coordination number (C) vs. porosity relations to capture the V_P/V_S behavior. We follow the binary scheme proposed by Bachrach et al. (2000, 2008), which assumes that some contacts behave as smooth contacts with zero tangential stiffness, and other contacts behave as adhered contacts with finite tangential stiffness. Instead of using Murphy's relations as in Bachrach's model, we use C-porosity and C-pressure relations inverted from experimental data.

We use the extended Walton model (Walton, 1987; Jenkins et al., 2005), which introduces a parameter α to represent the fraction of grain contacts that are perfectly adhered with each other. For a particular coordination number, the extended Walton model predicts the exactly same effective moduli as the Bachrach's model, where binary mixing is achieved using the Hertz-Mindlin model. We derive empirical C-porosity and C-pressure relations for P and S wave velocities by inverting dynamic measurements by Zimmer (2003) on dry, unconsolidated sandstones. We propose using the expanded Walton model (α =0.6) along with these new C, porosity, and pressure relations to predict velocities in unconsolidated sandstones for mechanical compaction. The proposed model provides reasonable fit to other experimental data on glass-beads (Zimmer, 2003) and Ottawa sands (Yin, 1992).

The chapter is organized as follows: We present a brief review of granular media models with different physical assumptions. Next, we use the extended Walton model to derive C-porosity, and C-pressure relations from experimental data. Finally, we provide a practical recipe for using granular media models in unconsolidated sands, and test it by applying it to other datasets.

3.3 Theoretical background on granular-media Models

We are interested in the effective elastic properties of a granular pack of spheres, for which each pair of grains in contact under normal and tangential loads determines

fundamental mechanics. Let us consider that two identical spheres, each with radius R, are pressed together. The force between the spheres acts over a contact zone. The radius of this contact zone a_n is small compared to R. Let 2δ be the relative normal displacement of the two spheres along the line joining their centers. The relative tangential displacement between the two spheres is 2τ. Similarly, the force can be decomposed into normal force component F_n, and tangential force component F_t.

The incremental relations between the force and the displacements can be expressed as (Norris and Johnson, 1997)

$$\Delta F_n = S_n(\delta)\Delta\delta, \quad \Delta F_t = S_\tau(\delta)\Delta\tau \tag{3.1}$$

where S_n and S_τ are the normal and tangential contact stiffnesses, with units of force/displacements. These stiffnesses can be written in the form

$$S_n = D_n a_n(\delta), \quad S_\tau = D_t a_t(\delta) \tag{3.2}$$

where D_n and D_t are actual stiffnesses with the units of pressure. They depend only on the material properties of the spherical grains.

$$D_n = \frac{4G}{1-\nu} = \frac{8\mu(\lambda+G)}{\lambda+2G}, \quad D_t = \frac{8G}{2-\nu} = \frac{16\mu(\lambda+G)}{3\lambda+4G} \tag{3.3}$$

where ν is the grain Poisson's ratio, λ is the Lame's first parameter of the grain, and G is the grain shear modulus.

The parameters a_n and a_t have dimensions of length. a_n is the radius of circle of contact between two spheres, and increases with δ, as shown in Table 3.1. a_t can be interpreted as the radius of the frictionally locked region of the contact; in the case of infinitely high friction (rough models) $a_n = a_t$, while in the case of zero friction (smooth models) $a_t = 0$. The radii a_n and a_t are independent of the material properties of the grains, and they depend upon the specific type of contact model. We have summarized the functional forms of a_n and a_t for several contact models in Table 3.1.

Table 3.1: The functional forms of a_n and a_t for different contact models. The effective elastic moduli, K_{eff} and G_{eff} depend on the contact stiffnesses S_n and S_τ, which in turn depend on a_n and a_t. The normal contact stiffness (S_n) depends on a_n, and the tangential contact stiffness (S_τ) depends on a_t. The values of S_n, S_τ and the effective elastic moduli are same for the Hertz-Mindlin model and the Walton's rough model. The effective elastic moduli in Digby's model are same as the Walton's smooth model when the initial contact radius (b) is zero.

Contact Model	Effective Moduli	Normal contact stiffness (S_n)	Tangential contact stiffness (S_τ)	a_n	a_t
Hertz-Mindlin (rough)	$K_{eff} = \frac{C(1-\phi)}{12\pi R} S_n$ $G_{eff} = \frac{C(1-\phi)}{20\pi R}(S_n + 1.5S_\tau)$	$\frac{4G}{1-\nu} a_n$	$\frac{8G}{2-\nu} a_t$	$(R\delta)^{1/2}$	a_n
Walton rough	,,	,,	,,	,,	,,
Walton smooth	,,	,,	,,	,,	0
Digby (hybrid of rough and smooth)	,,	,,	,,	$\left[(R^2\delta^2 + \frac{b^4}{4})^{1/2} + \frac{b^2}{2}\right]$ b= initial contact radius	b

The contact models presented in Table 3.1 are: (1) the Hertz-Mindlin model (Mindlin, 1949) for infinitely rough spheres (very high friction coefficient), (2) the Walton (1987)

model for infinitely rough spheres, (3) the Walton (1987) model for infinitely smooth spheres (zero friction coefficient), and (4) the Digby (1987) model for infinitely smooth spheres. In all of these contact models, the effective bulk moduli (K_{eff}) and the effective shear moduli (G_{eff}) can be expressed as (Winkler, 1983; Mavko et al., 1998)

$$K_{eff} = \frac{C(1-\phi)}{12\pi R} S_n \tag{3.4}$$

$$G_{eff} = \frac{C(1-\phi)}{20\pi R} (S_n + 1.5 S_\tau) \tag{3.5}$$

where C is the coordination number (average number of contacts that each grain has with its neighbors), and ϕ is the porosity. Note that the differences among the various contact models lie only in the assumed relation of a_n and a_t to pressure and friction (see Table 3.1).

The Hertz-Mindlin model (Mindlin, 1949) is the most commonly used contact model for unconsolidated sandstones. This model assumes that grain contacts are first exposed to normal loading, and tangential forces are applied afterwards. Walton (1987) formulated another contact model in which normal and shear deformation occur simultaneously. The results were given for two special cases: infinitely rough spheres (friction coefficient is very large) and ideally smooth spheres (friction coefficient is zero). a_n is same for both the cases, and $a_t = 0$ for smooth spheres. The values of S_n, S_τ and the effective elastic moduli are same for the Hertz-Mindlin model and the Walton's rough model. Digby (1981) formulated a different contact model, in which the contacting smooth spheres are initially firmly bonded across small, flat, circular area of the same average radius b. When b is zero, the effective elastic moduli are same as the Walton's smooth model.

In addition to the Hertz-Mindlin model, and the Walton models, we have compared the measurements on unconsolidated sands against the Jenkins model, modified Jenkins model, and the extended Walton model. In the Jenkins et al. model (2005), the centers of a pair of frictionless contacting grains have sufficient translational freedom to satisfy

force equilibrium, while their surrounding neighbors are constrained to move with the increments in the average strain. This incorporates an additional degree of freedom in the relative displacement of the grains in contact. The resulting elastic moduli are:

$$\lambda_{eff}^{J} = \frac{C(1-\phi)}{10\pi R} S_n^J \begin{Bmatrix} 1-2\psi^{-1}(\omega_1+7\omega_2)+2\psi^{-2}(\kappa_1+2\kappa_2+5\kappa_3) \\ -2\psi^{-3}(\xi_1+2\xi_2+5\xi_3) \end{Bmatrix} \tag{3.6}$$

$$G_{eff}^{J} = \frac{C(1-\phi)}{10\pi R} S_n^J \left\{1-2\left[\psi^{-1}(\omega_1+2\omega_2)-\psi^{-2}(\kappa_1+2\kappa_2)+\psi^{-3}(\xi_1+2\xi_2)\right]\right\} \tag{3.7}$$

where S_n^J is normal contact stiffness defined as

$$S_n^J = \frac{u(2R)}{(1-\nu)}\left[\frac{3\pi}{2C}\frac{(1-\nu)}{(1-\phi)}\frac{P}{G}\right]^{1/3} \tag{3.8}$$

u is the relative displacement of the points of contact, and P is the effective pressure. The other coefficients (ψ, ω_1, ω_2, κ_1, κ_2, κ_3, ξ_1, ξ_2, and ξ_3) are functions only of geometry. The Jenkins model is valid only for C >5.1. This model predicts a large drop in shear modulus compared to the Hertz-Mindlin model, the Walton rough model, and the Walton smooth model.

The Jenkins model considers translation, but the grains are assumed to be frictionless. We provide a modified form of Jenkins model by heuristically incorporating the frictional term as given by Jenkins et al. (2005). We call this the Modified Jenkins model. The elastic moduli, λ^{MJ} and G^{MJ} are obtained as follows

$$\lambda^{MJ} = \lambda^{Jenkins}\left[\frac{[2-\nu-2\alpha(1-\nu)]}{(2-\nu)}\right] \tag{3.9}$$

$$G^{MJ} = G^{Jenkins}\left[\frac{[2-\nu+3\alpha(1-\nu)]}{(2-\nu)}\right] \tag{3.10}$$

The elastic moduli in the Modified Jenkins model are obtained by multiplying the specific terms in bracket as shown in equations 3.9 and 3.10. This modification is ad hoc

and heuristic. However, we can think of the Modified Jenkins model as frictional-Jenkins model by comparing the expressions with the extended Walton model (equations 3.11 and 3.12). When α is zero (ideal smooth spheres) we obtain the original Jenkins model, and when α is equal to 1 (ideal rough spheres), in effect we compute the elastic moduli of an isotropic, random aggregate of identical frictional spheres. This model is valid only for C >5.1.

Walton's rough and smooth models can be combined, as shown by Jenkins et al., (2005) to represent a mixture of perfectly rough and smooth spheres. In this chapter, we refer this combined model as the extended Walton model. The elastic moduli, λ_{eff}^{Ew} and G_{eff}^{Ew}, are expressed as:

$$\lambda_{eff}^{Ew} = \lambda_{eff}^{Walton\_smooth} \frac{[2-\nu-2\alpha(1-\nu)]}{(2-\nu)} \tag{3.11}$$

$$G_{eff}^{Ew} = G_{eff}^{Walton\_smooth} \frac{[2-\nu+3\alpha(1-\nu)]}{(2-\nu)} \tag{3.12}$$

where

$$\lambda_{eff}^{Walton\_smooth} = \frac{C(1-\phi)}{5\pi} \frac{G}{(1-\nu)} \left[\frac{3\pi}{2} \frac{(1-\nu)}{(1-\phi)C} \frac{P}{G} \right]^{1/3} \tag{3.13}$$

$$G_{eff}^{Walton\_smooth} = \frac{C(1-\phi)}{5\pi} \frac{G}{(1-\nu)} \left[\frac{3\pi}{2} \frac{(1-\nu)}{(1-\phi)C} \frac{P}{G} \right]^{1/3} \tag{3.14}$$

We interpret α as the fraction of grain-contacts that are perfectly rough. When α is zero, we obtain the Walton smooth model, where all the grains have zero friction at their contacts. When α is equal to 1, we obtain the Walton rough model, which considers infinitely high friction at the grain contacts of identical spheres. For an intermediate value of α, this model represents a mixture of perfectly rough and smooth spheres.

Since the effective shear moduli (G_{eff}) of a granular aggregate is linearly proportional to tangential stiffness (S_τ) as shown in equation 3.5, it is possible to lower

G_{eff} by assuming S_τ is zero for some fraction of the grains. We use equations 3.11 and 3.12 to represent this scenario in the extended Walton model, where α represents the fraction of completely adhered contacts, and (1-α) represents the fraction of completely slipping contacts. Note that exactly the same expressions are reached by assuming that some of the grains have zero S_τ in the Hertz-Mindlin effective-medium model (Bachrach et al., 2000; Avseth and Bachrach, 2005; and Bachrach and Avseth, 2008). In this chapter, we use the extended Walton model along with new coordination number, porosity, and pressure relations to compute the effective elastic moduli.

3.4 Results from numerical experiments

We compute the velocity mis-prediction error between observed and modeled velocities by six different granular-media models assuming two different C-porosity relations: (a) the C-porosity relationship given by Murphy (1982), and (b) the C-porosity relationship obtained from granular dynamics simulations by Garcia et al. (2004). The latter relation provides a lower value of C (<5.1) at the porosity range (37 to 40%) of these sandstones, and cannot be used with the Jenkins et al. model (2005) and its modified version, since these models fail below coordination number 5.1. The observed ultrasonic velocities are from dry unconsolidated sands in the loading cycles measured by Zimmer (2003). Figure 3.3 shows the mis-prediction error at two different pressure regimes: 0 to 5 MPa and 6 to 20 MPa. We find that at the low pressure regime 0- 5 MPa, Garcia's C-porosity relation better predicts velocities than Murphy's C-porosity relation when coupled with *frictional* models (e.g., the Hertz-Mindlin and the Walton-rough models). The *frictionless* models (e.g., the Jenkins and the Walton-smooth) provide better velocity predictions with higher coordination number as given by Murphy. This numerical experiment shows that no existing granular media model perfectly fits the data with either Murphy or Garcia's C-porosity relations. Therefore, in order to improve the predictions, we design a new C-porosity relation.

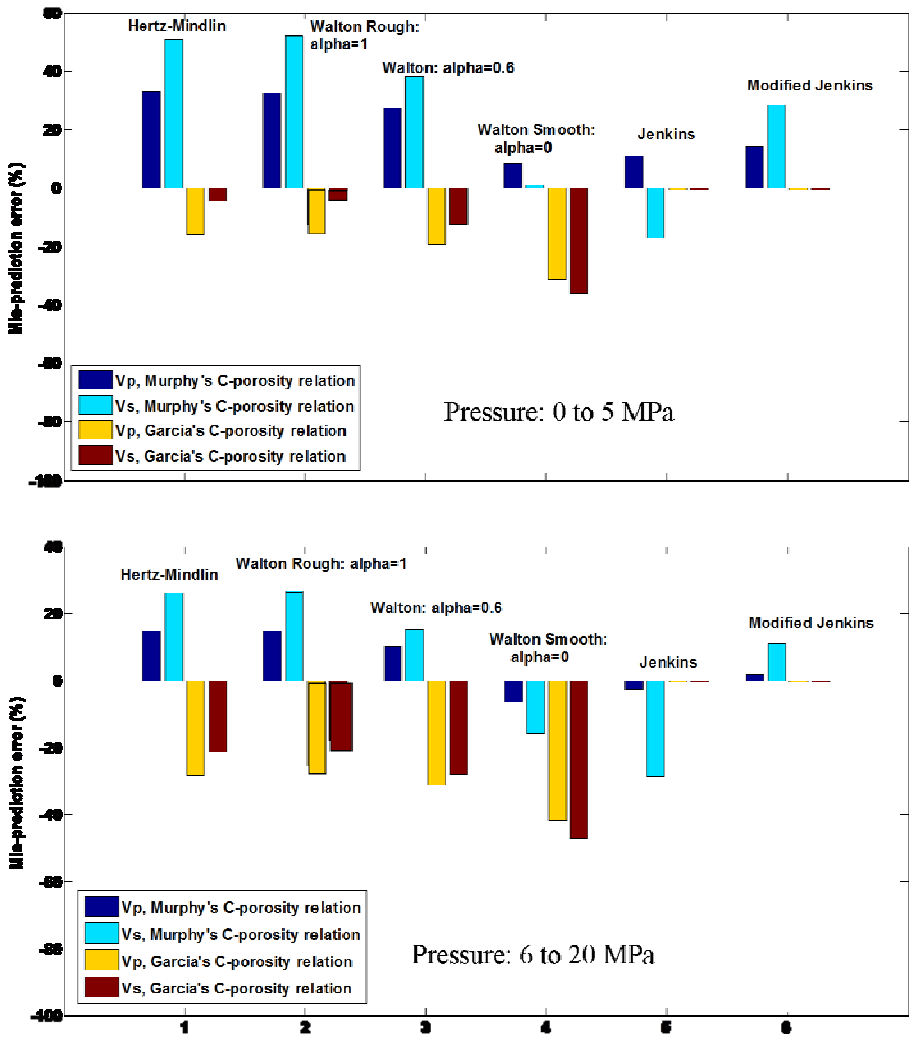

Figure 3.3: Velocity mis-predictions by different models using two different coordination number (C) vs. porosity relations: Murphy (1982) and Garcia et al. (2004). Top: low pressure regime (0 to 5 MPa). Bottom: high pressure regime (6 to 20 MPa). The C-porosity relation from numerical simulation (Garcia et al., 2004) works better with frictional models (e.g., Hertz Mindlin, Walton-Rough) only at low pressure regime.

New coordination number (C), porosity and pressure relations to compute effective velocities

We use the extended Walton model ($\alpha = 0.6$) to invert the coordination number from dynamic measurements on dry, unconsolidated sandstones by Zimmer (2003). This particular value of α is chosen since it provides geometrically realistic predictions of C (discussed later). We consider the first loading cycle of the sample from Pomponio

Beach, California. The initial porosity of this uncompacted sand is 40%. The porosity decreases from 40% to 37% due to an increase in effective pressure from 0 to 20 MPa. This is geologically analogous to the porosity loss during progressive burial due to mechanical compaction. The mineralogical composition of the sample from XRD analysis (Zimmer, 2003) and the moduli of each mineral used in our modeling are shown in Table 3.2. The effective mineral moduli are then calculated using Voigt-Reuss-Hill average (Mavko et al., 1998), and the effective density is calculated using arithmetic average. The effective mineral moduli are bulk modulus= 46 GPa, shear modulus= 31 GPa, and density=2.64 gm/cc.

Table 3.2: Mineralogical composition of Pomponio sand from Zimmer (2003), and the mineral moduli used in our modeling.

Mineral	Mineral Components (% Wt.)	Bulk modulus (GPa)	Shear modulus (GPa)	Density (gm/cc)
Quartz	53%	36.6	45	2.65
Plagioclase Feldspar	29%	75.6	25.6	2.63
K-Feldspar	12%	37.5	15	2.62
Clay	2%	22	7	2.58
Others [1]	3%	76.8	32	2.71

[1]includes dolomite, calcite, pyrite, pyroxene. In our modeling, we assume the mineral moduli of calcite. In addition, there is 1% amphibole for which we assume the mineral moduli of clay.

In order to obtain the best C at a particular porosity, we compute the V_P and V_S for different values of C using the extended Walton model ($\alpha = 0.6$). Next, we calculate velocity mis-prediction error. The value of C that minimizes the L1 norm of the mis-prediction error is taken to be the optimal C for that porosity. The best C values at different porosities and corresponding pressures are presented in Table 3.3 and Figure 3.4. We find that prediction of VS requires a lower value of C than the prediction of V_P. C_P and C_S represent coordination numbers to fit V_P and V_S, respectively. The C-porosity relations given by Murphy (1982) and Garcia et al. (2004) are also plotted in Figure 3.4 for comparison. Our relation is similar to Garcia's relation at higher porosity, and it

deviates from Garcia's relation and approaches Murphy's relation at lower porosity.

Table 3.3: Coordination number for P –wave (C_P) and S-wave (C_S) velocities inverted from data using the extended Walton model (α =0.6)

Porosity	Pressure (MPa)	C_P	C_S
40	0.5	5.5	4
39	2.45	7.8	6
38	9.95	8.6	6.8
37	17.5	10.2	7.5

We fit power law equations of the form $f(x) = ax^b + c$ to get the new C_P-porosity, C_S -porosity, C_P-pressure and C_S-pressure relations for P and S wave velocities, as shown in equations 3.15-3.18. In these equations, ϕ is in percentage and P is in MPa. The adjusted R-squares of all the fits are close to 0.9.

$$C_P(\phi) = (-2.338\text{e}-014)\phi^{9.099} + 14.45 \tag{3.15}$$

$$C_S(\phi) = (-1.798\text{e}-014)\phi^{9.099} + 11.02 \tag{3.16}$$

$$C_P(P) = (777.1)P^{0.001545} - 770.7 \tag{3.17}$$

$$C_S(P) = (-4.457)P^{-0.2724} + 9.401 \tag{3.18}$$

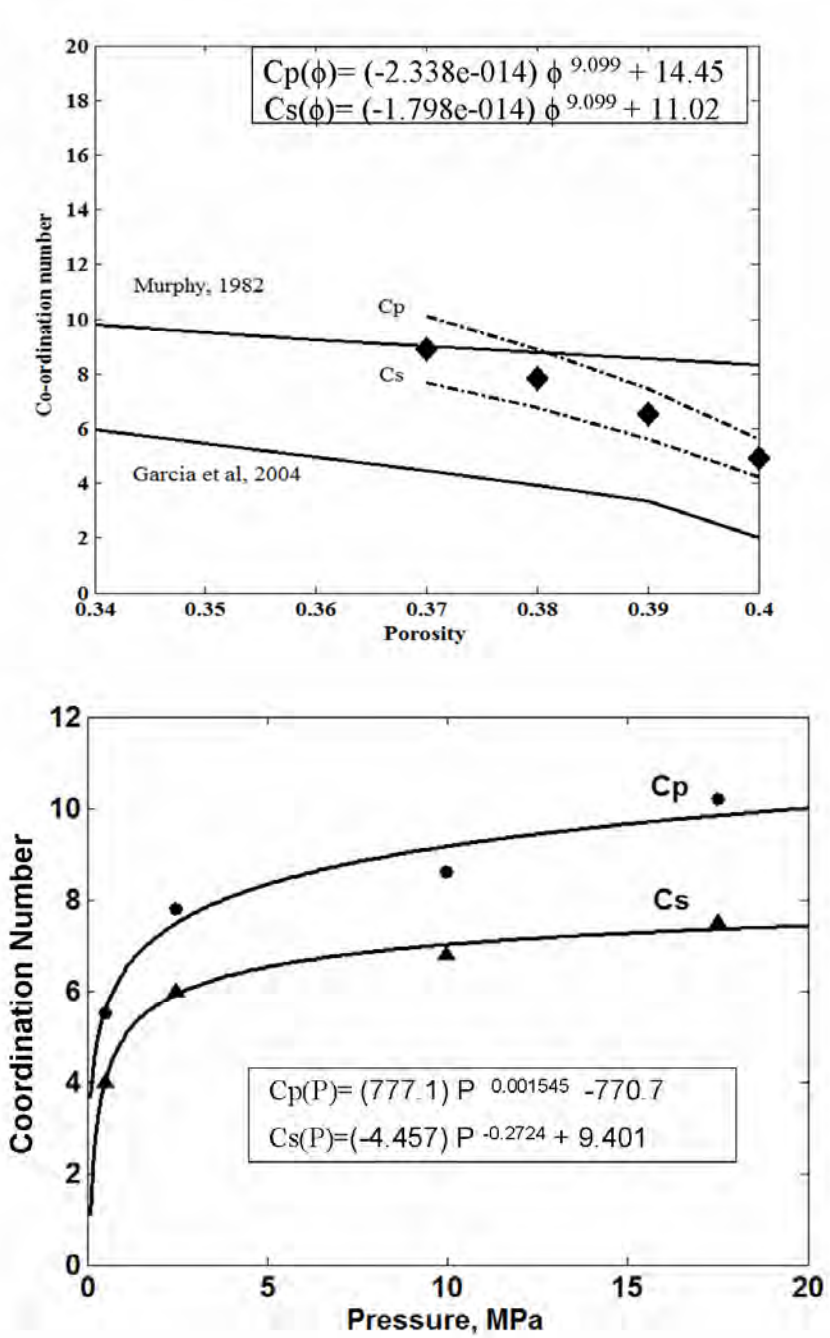

Figure 3.4: Top: coordination number (C) vs. porosity, Bottom: coordination number (C) vs. pressure. C-porosity relations by Murphy (1982) and Garcia et al. (2004) behave as upper and lower bounds, respectively. C_P and C_S represent coordination numbers obtained by fitting V_P and V_S, respectively. Note that we obtain $C_P > C_S$ at all porosities and pressures.

We test the sensitivity of the value of α on the selection of C. The best fits of C at different porosities are determined using the extended Walton model for different values of α (Figure 3.5). Here, C represents the mean of C_P and C_S. We observe that as α decreases, the difference between C_P and C_S decreases, and a larger value of C is required to fit the velocities. This observation suggests that lowering the values of α may not always be justified, especially when it demands very high, unrealistic C to fit the data. For example, choosing α =0, i.e., selecting zero friction at all the grain-contacts requires C=17 near critical porosity. Although this value of C fits the data, it is an unrealistically high coordination number for a random pack of grains. For example, a hexagonal close pack has the highest possible coordination number C=12. We suggest α=0.6 for two reasons: (1) it provides reasonable prediction of C in the porosity range for a random pack, and (2) the difference between C_P and C_S is lower compared to α=1.

It is possible to generalize the equations 3.15 to 3.18 for values of α different than 0.6. We use the functional form $f(x) = a + b\phi^c / d + \alpha^c$ to get the relations for general values of α ranging from 0.3 to 1 (equations 3.19 to 3.22). The adjusted R-squares of all the fits are close to 0.9.

$$C_p(\phi,\alpha) = (136.14 - 35.12\phi^{0.36}) / (-.06 + \alpha^{0.36}) \tag{3.19}$$

$$Cs(\phi,\alpha) = (62.19 - 24.37\phi^{0.25}) / (-.51 + \alpha^{0.25}) \tag{3.20}$$

$$C_p(P,\alpha) = (1.75 + 2.01\phi^{0.28}) / (-.23 + \alpha^{0.28}) \tag{3.21}$$

$$C_p(P,\alpha) = (-1.52 + 1.52\phi^{.004}) / (-.99 + \alpha^{.004}) \tag{3.22}$$

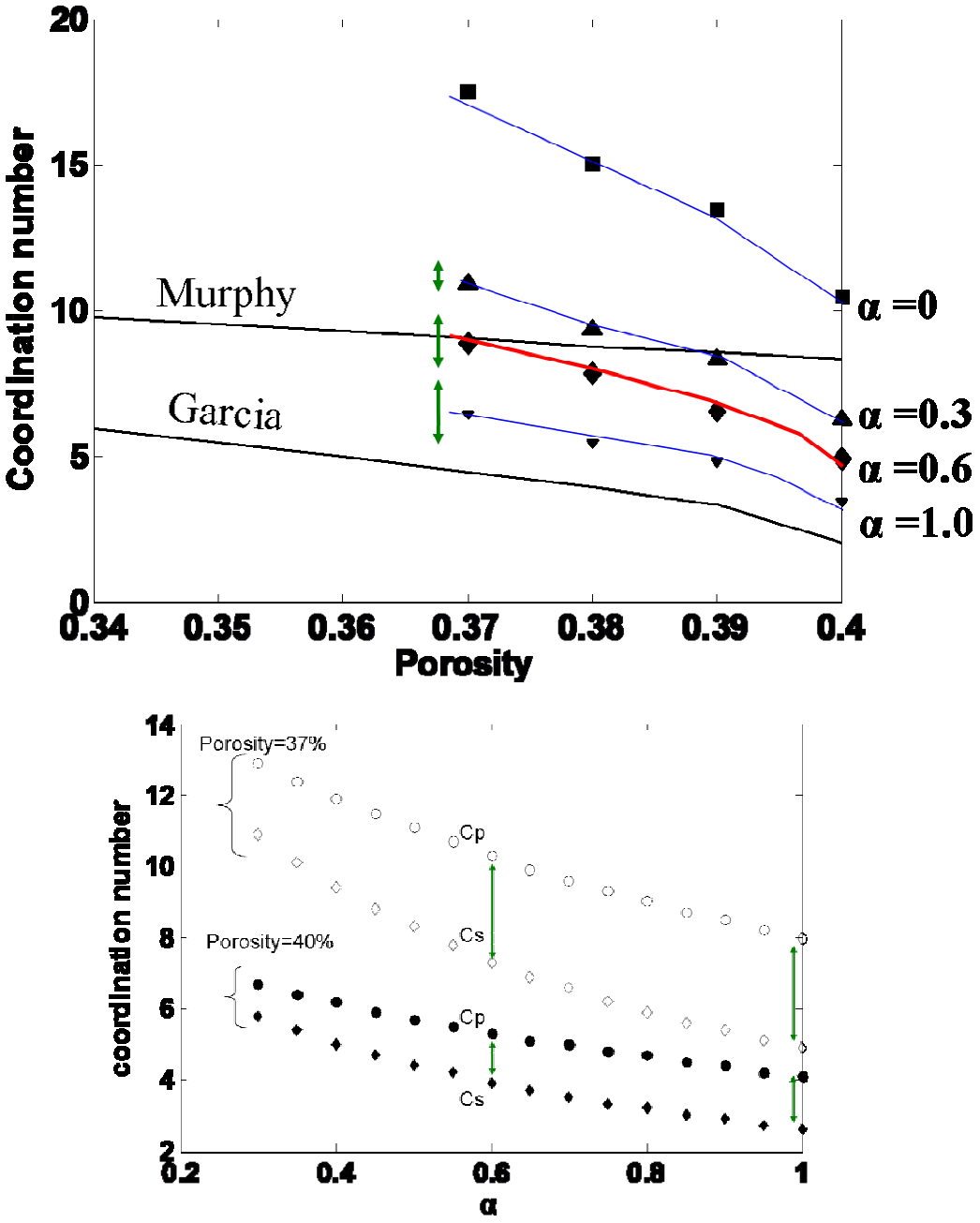

Figure 3.5: Top: Average of P and S coordination numbers vs. porosity for four different values of α. Bottom: Coordination number vs. α for two different values of porosity. The green arrow represents the magnitude of difference between C_P and C_S (C_P and C_S are coordination numbers for predicting V_P and V_S, respectively). As α decreases, the difference between C_P and C_S is lowered, and a higher value of C is required to fit the velocities. It is possible to fit the observed velocities with α=0 using a single value for C, but this demands an unrealistically high C near critical porosity for a random pack of grains.

3.5 Proposed recipe for using granular medium model for unconsolidated sands

From the above modeling results, it is clear that in order to improve the prediction of velocities in granular materials, one can account for porosity, pressure, friction, and coordination number (C). We express C as a function of pressure and porosity. The C-porosity or the C-pressure relations are then combined with the extended Walton model using α =0.6. In the absence of knowledge of the fraction of frictionless contacts, the value of α is chosen such that it provides reasonable estimation of C for the porosity changes in unconsolidated sands due to mechanical compaction.

We provide a two-step recipe to predict effective elastic properties in unconsolidated sandstones:

Step 1: Use equations 3.15-3.18 to obtain coordination number as a function of pressure or porosity.

Step 2: Use $\alpha = 0.6$ in equations 3.11 and 3.12 to compute effective dry elastic moduli for the granular aggregate.

The following presuppositions and limitations apply to the proposed recipe:

1. The contact model assumes identical, isotropic, elastic spherical grains

2. Each contact experiences homogenous strain (a limitation due to Effective medium approximation)

The above recipe is for dry rocks. The presence of pore fluid in the system will need to be addressed separately (e.g., Gassmann, 1951). Also, the theory does not account for cement at the grain contacts. We apply the above recipe to predict velocities as a function of pressure. Figure 3.6 shows velocities and V_P/V_S ratio on dry, unconsolidated sandstones. The same data were used to invert C-porosity, and C-pressure relations. We showed the conventional Hertz-Mindlin model predictions using Murphy's C-porosity relation for this particular data in Figure 3.1. In addition, we have tested our recipe on two different datasets. The predicted V_P and V_S show reasonable agreement with measurements on glass-beads (Zimmer, 2003) and Ottawa sandstone (Yin, 1992) (Figure

3.7). The velocity predictions by Hertz-Mindlin model using Murphy's C-porosity relation are also shown in Figure 3.7. Comparisons with the Hertz-Mindlin model demonstrate the improvement in velocity predictions; in particular the V_S predictions improve significantly using our recipe.

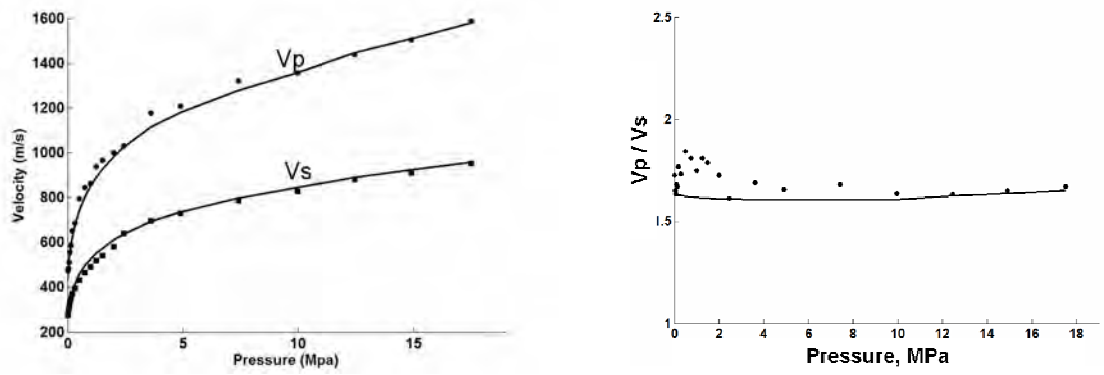

Figure 3.6: The velocities shown in this plot are measured by Zimmer (2003) on dry, unconsolidated sandstones (from Pomponio beach). The data is same as shown in Figure 3.1. The solid lines show the predictions of velocities using our recipe.

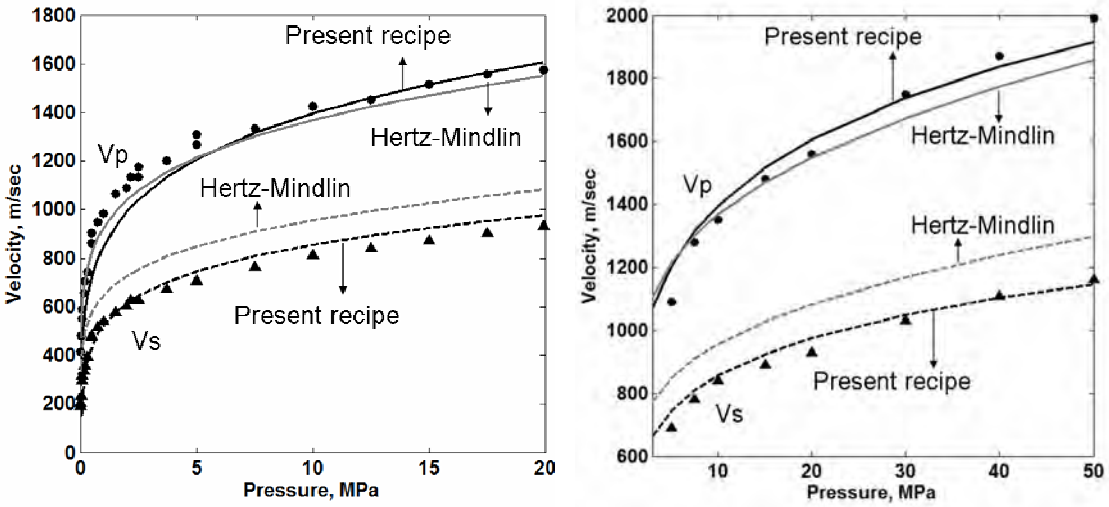

Figure 3.7: Testing the predictions of our recipe with experimental data. Left: glass-beads (Zimmer, 2003); Right: Ottawa sands (Yin, 1992). Black lines: predictions using present recipe, Grey lines: predictions using Hertz-Mindlin model with Murphy's coordination number-porosity relation. Our recipe reasonably predicts V_P as well as V_S measurements. Comparisons with the Hertz-Mindlin model demonstrate the improvement in velocity predictions; the V_S predictions, in particular, improve significantly using our recipe.

3.6 Discussion

In this chapter, we present a practical, recipe for using granular media model for unconsolidated sandstones with the convenience of closed-form expressions. For this, we use the extended Walton model, and combine that model with an appropriate coordination number (C), porosity, and pressure relations. The extended Walton model (Walton, 1987; Jenkins et al., 2005) can be used to allow some fraction of grains to have zero friction at their contacts. This lowers the average tangential stiffness of the granular aggregate for computations of effective elastic moduli. Note that although our model is similar to that of Bachrach et al. (2008), who used the Hertz-Mindlin model instead of the Walton model to compute the contact stiffnesses. The important difference between Bachrach et al. (2008) and our model is that instead of using Murphy's coordination number (C)-porosity relation (Murphy, 1982), we identify a different relation based on experimental data (equations 3.15-3.18).

The C-porosity and C-pressure relations for P and S wave velocities are derived by inverting dynamic measurements by Zimmer (2003) on dry, unconsolidated sandstones. For this, we have set the fraction of adhered contacts (α) to be equal to 0.6 in the extended Walton model. This particular value of α yields geometrically reasonable coordination numbers for a random closed pack of grains. The existing C-porosity relations by Murphy (1982) and Garcia et al. (2004) appear to behave as upper and lower bounds, respectively. Our C-porosity relation is similar to Garcia's relation at high porosity, and it approaches Murphy's relation at lower porosity. The C values in Murphy's relation are higher than our predicted values since Murphy's relation is compiled for random as well as ordered packings, such as hcp and fcc. The reason why numerical simulations provide a lower C is an open question. In real geological scenarios, grains are subjected to mechanical compaction over a finite geologic time. We conjecture that hiatus plays an important role during mechanical compaction. A hiatus (brief pause in sedimentation) can create tamping and shaking of grains, which may lead to tighter packing and increase in C, not usually accounted in the numerical simulations.

Present modeling results show that we need different C-porosity relations to improve the predictions of P and S wave velocities. The reasons can be two folds: (1) the granular media models are not perfect enough to predict the shear-wave velocities of real unconsolidated sands, and (2) the rock may experience a lower effective C when the shear wave propagates through it.

The C-porosity and C-pressure relations presented in this chapter represent the mean values of C at different porosities and pressures. We expect deviations from this mean trend due to uncertainty in measured data and model parameters. In order to account for this uncertainty, we can consider a Gaussian distribution of coordination number. For example, Smith et al. (1929) experimentally found that coordination number can be represented as a Gaussian distribution at different porosities.

The parameter α that we use to better fit experimental data is interpreted as the fraction of contacts that are perfectly locked under infinitesimal strain associated with dynamic loading. We might interpret α as an ad hoc correction for one of the biggest shortcomings of EMA, viz., that strains are homogenous and all contacts are similarly load-bearing. Photoelastic imaging of stress chains under isotropic loading (Majmudar and Behringer, 2005) and numerical simulations of granular packs (Geng et al., 2001; Makse et al., 2004) show that, in fact, the stress distribution is very heterogeneous.

For static experiments, the parameter α in equations 3.11 and 3.12 can be linked with S_τ as follows:

$$\alpha_S = \frac{2-\nu}{8a\mu} S_\tau \tag{3.23}$$

where α_S denotes the parameter α for static experiments, and μ is the coefficient of friction. Mindlin (1951) and other researchers (Winkler, 1983; Norris and Johnson, 1997) have shown that α_S depends on the friction-coefficient, μ:

$$\alpha_S = (1 - \frac{F_T}{\mu F_N})^{1/3} \tag{3.24}$$

In equations 3.23 and 3.24, α_s signifies the ratio of inner-annulus radius to contact radius. Mindlin (1951) suggested that the no-slip assumption is untenable under large strain, and slip occurs on an outer annulus. According to Mindlin (1951), slip begins at the edge of contact surface and progresses inward with increasing shear force, thereby decreasing the value of α_s. When the grains slip, they obey Coulomb's law of friction: $F_T = \mu F_N$, which leads to α_s=0. Therefore, α_s is zero when the grains slip, and we obtain the original Walton smooth model. For infinitely rough spheres, μ is very high and α_s is equal to 1. An intermediate value of α_s corresponds to an intermediate friction at the grain-contacts. Reliable measurements of static shear moduli on unconsolidated sands are not readily available from laboratory experiments. Therefore, future work can benefit from numerical simulation results with different values of the friction coefficient (e.g., Garcia and Medina, 2006) to test the predictions of effective static moduli. Winkler (1983) and Mavko (1979) have pointed out that, in general, non-linear effects are not observed at the small strain amplitudes typical of acoustic wave propagation. This implies that lowering the value of friction does not allow the grains to slip at small strain amplitudes. Therefore, the assumption of intermediate friction at the grain contacts is valid for static measurements where strain amplitude is large ($> 10^{-3}$), but should not be applied for small-strain ($<10^{-4}$), acoustic wave propagation.

3.7 Conclusions

We present a recipe to improve the predictions of seismic velocities, especially the shear wave velocities, in unconsolidated sands during mechanical compaction. For this, we assume that some of the grains have zero friction at grain contacts, and derive coordination number, porosity, and pressure relations for P and S wave velocities from experimental data. We use an extension of the Walton's contact model, which introduces a parameter α that represents the fraction of grains perfectly adhered to each other. We propose the extended Walton model ($\alpha = 0.6$) along with new C-porosity or C-pressure relations to predict velocities in unconsolidated sandstones for mechanical compaction. The proposed recipe provides reasonable fit to other experimental data on glass-beads

(Zimmer, 2003) and Ottawa sands (Yin, 1992), and specifically improves the predictions of shear wave velocities. This modeling approach can be useful for improving our understanding of V_S predictions and AVO signatures in unconsolidated sands.

3.8 Acknowledgements

This work was supported by the Stanford Rock Physics and Borehole Geophysics project and DOE contract DE-FC26-04NT15506. We thank Jack Dvorkin, James Spencer and Bill Murphy for valuable discussions.

3.9 References

Avseth, P. and R. Bachrach, 2005, Seismic properties of unconsolidated sands: Tangential stiffness, V_P/V_S ratios and diagenesis: SEG Expanded Abstracts, 24, 1473.

Bachrach, R., J. Dvorkin, and A. Nur, 2000, Seismic velocities and Poisson's ratio of shallow unconsolidated sands: Geophysics, 65, 559–564.

Bachrach, R. and P. Avseth, 2008, Rock physics modeling of unconsolidated sands: Accounting for nonuniform contacts and heterogeneous stress fields in the effective media approximation with applications to hydrocarbon exploration: Geophysics, 73, E197–E209.

Coste, C., and B. Gilles, 1999, On the validity of Hertz contact law for granular material acoustics: European Physical Journal B, 7, 155–168.

De Gennes, P., 1996, Static compression of a granular medium: The soft shell model: Europhysics Letters, 35, 145–149.

Domenico, S. N., 1977, Elastic properties of unconsolidated porous sand reservoirs: Geophysics, 42, 1339–1368.

Estes, C.A., G. Mavko, H. Yin, and T. Cadoret, 1994, Measurements of velocity, porosity, and permeability on unconsolidated granular materials: SRB Annual Report, 55(B):G1-1 – G1-9.

Garcia, X., M. Araujo1, and E. Medina, 2004, P-wave velocity–porosity relations and homogeneity lengths in a realistic deposition model of sedimentary rock: Waves Random Media, 14, 129–142.

Garcia, X., and E.A.Medina, 2006, Hysteresis effects studied by numerical simulations: Cyclic loading-unloading of a realistic sand model: Geophysics, 71, F13.

Gassmann, F., 1951, Uber die elastizitat poroser medien: Veirteljahrsschrift der Naturforschenden Gesellschaft, 96, 1-23.

Geng, J., D. Howell, R.P. Behringer, G. Reydellet, L. Vanel, and E. Clement, 2001, Footprints in the sands: The response of granular material to local perturbations: Physical Review Letters, 87, 035506 1-4.

Goddard, J.D., 1990, Nonlinear Elasticity and Pressure-Dependent Wave Speeds in Granular Media: Proceedings of the Royal Society of London. Series A, Mathematical and Physical Sciences, 430, 105-131.

Hertz, H., 1882, On the Contact of Rigid Elastic Solids and on Hardness, chapter 6. New York: Macmillan.

Jenkins, J., D. Johnson, L. La. Ragione, and H. Makse, 2005, Fluctuations and the effective moduli of an isotropic, random aggregate of identical, frictionless spheres: Journal of the Mechanics and Physics of Solids, 53, 197- 225.

Majmudar, T.S. and R.P. Behringer, 2005, Contact force measurements and stress induced anisotropy in granular materials: Nature, 23, 1079-1082.

Makse, A., N. Gland, D. Johnson, and M. Schartz, 1999, Why effective-medium theory fails: Physical Review Letters, 83, 5070–5073.

Makse, A., N. Gland, D. Johnson, and L. Schwartz, 2004, Granular packings: Nonlinear elasticity, sound propagation, and collective relaxation dynamics: Phys. Rev. E 70, 061302.

Mavko, G., 1979, Frictional attenuation: An inherent amplitude dependence: Journal of Geophysical Research, 84, 4769-4775.

Mavko, G., T. Mukerji, and J. Dvorkin, 1998, The Rock Physics Handbook, tools for seismic analysis in porous media: Cambridge University press.

Mindlin, RD, 1949, Compliance of elastic bodies in contact: Trans. ASME, 71, A-259.

Mindlin, R. D., W. P. Mason, I. F. Osmer, and H. Deresiewicz, 1951, Effects of an Oscillating Tangential Force on the Contact Surfaces of Elastic Spheres: Proceedings of the First U.S. National Congress of Applied Mechanics, 203–208.

Murphy, W.F., 1982, Effects of Microstructure and Pore Fluids on the Acoustic Properties of Granular Sedimentary Materials: PhD dissertation, Stanford University.

Norris, A.N., and D.L. Johnson, 1997, Non-linear elasticity of granular media: Journal of Applied Mechanics, 64, 39-49.

Smith, W., P. Foote, and P. Busang, 1929, Packing of homogenous spheres: Physical Review, 34, 1271-1274.

Walton, K., 1987, The effective elastic moduli of a random pack of spheres: J. Mech. Phys. Sol., 35, 213-226.

Wang, Z. and A. Nur, 1992, Elastic wave velocities in porous media: A theoretical recipe, Seismic and Acoustic Velocities in Reservoir Rocks, 2, SEG Geophysics reprint series, 10.

Winkler, K.W., 1983, Contact stiffness in molecular porous materials: Comparison between theory and experiment: Geophys. Res. Lett., 10, 1073-1076.

Yin, H., 1992, Acoustic velocity and attenuation of rocks: Isotropy, Intrinsic Anisotropy, and Stress-Induced Anisotropy: PhD dissertation, Stanford University.

Zimmer, M., 2003, Seismic velocities in unconsolidated sands: Measurements of pressure, sorting, and compaction effects. Ph.D. dissertation, Stanford University.

Zimmer, M. A., M. Prasad, G. Mavko, and A. Nur, 2007, Seismic velocities of unconsolidated sands: Part 1. Pressure trends from 0.1 to 20 MPa: Geophysics, 72, E1-E13.

Chapter 4
Compaction trends for shale and clean sandstone in shallow sediments, Gulf of Mexico

"Simplicity is the ultimate sophistification."

--Leonardo da Vinci

4.1 Abstract

We present compaction trends for shale and clean sandstones in shallow sediments of the Gulf of Mexico. Specifically, we explore how the elastic properties (V_P, V_S and V_P/V_S ratio) and porosity of shallow sediments change with depth and effective pressure. The knowledge of such trends is useful for successful drilling operations, especially in deep-water environments. However, well data in the shallow section (<1000 meters) are often rare, and when available can be of poor-quality and lacking in necessary measurements. To address this problem, we integrate measurements for shale and sandstones from multiple sources including well-logs, geotechnical borehole data, and core measurements from shallow sections of Gulf of Mexico. We find that laboratory measurements by Zimmer (2003) on high-porosity, unconsolidated sandstones conducted

at low effective pressure agree with other data, and can be used to compute the compaction trends in shallow sandstones. Our study shows that compaction trends in shallow sub-surface can be drastically different from that of the deeper section. Therefore, simple extrapolation of depth trends from the deeper section can lead to erroneous results in the shallow sub-surface. The compaction trends in clean sandstones agree with the predictions using an effective-medium model (extended Walton model) combined with appropriate coordination number, porosity, and pressure relations. The results can be useful to interpret seismic amplitudes of shallow sediments in terms of resource potential and drilling hazards.

4.2 Introduction

Compaction depth trends are important in drilling, basin modeling and seismic explorations for several purposes: (1) to detect overpressure and hydrocarbon zones and distinguishing them from seismic velocity anomalies (e.g., Hottmann and Johnson, 1965; Magara, 1978; Chapman, 1983; Japsen, 1998 and 1999; Winthaegen and Verweij, 2003), (2) to calculate interval velocities and depth conversion of seismic data and earth models (e.g., Slotnick, 1936; Japsen, 1993; Al-Chalabi 1997b), (3) to predict seismic signatures of sand-shale interfaces as a function of depth (e.g., Smith and Sondergeld, 2001), and (4) to recognize over-compacted zones due to uplift (e.g., Acheson, 1963; Magara, 1978; Bulat and Stoker, 1987; Japsen, 1993, 1998, and 2000; Hillis, 1995; Hansen, 1996b; Heasler and Kharitonova, 1996; Ware and Turner, 2002; Corcoran and Doré, 2005; Corcoran and Mecklenburgh, 2005; Walford and White, 2005; Mackay and White, 2006).

Several researchers have studied the effects of compaction on the porosity of sands and shales (e.g., Magara, 1980; Ramn and Bjoerlykke, 1994; Lander and Walderhaug, 1999). The effects of compaction on velocity-depth trends have been discussed by different researchers (e.g., Slotnick, 1936; Bulat and Stoker, 1987; Hillis, 1995; Al-Chalabi, 1997a; Magara, 1978; Hansen, 1996b; Faust, 1951; Acheson, 1963; Chapman, 1983; Japsen,1998, 1999, and 2000). However, porosity and velocity depth trends in shallow section are not well established. The main challenge in computing such trends is

the paucity of well log data in shallow subsurface. Figure 4.1 shows a typical well log response from the Gulf of Mexico. It lacks measurements in the shallow section (< 3000 ft or ~1000 meters) due to riser-less drilling, and log response from the deeper section cannot be used to compute normal compaction trend due to overpressure. One way to overcome this challenge is to integrate data from multiple sources. In this chapter, we compute porosity and velocity depth trends by integrating data from multiple sources including well-logs, geotechnical borehole data, and core measurements from shallow sections of Gulf of Mexico, and laboratory measurements at low effective pressure.

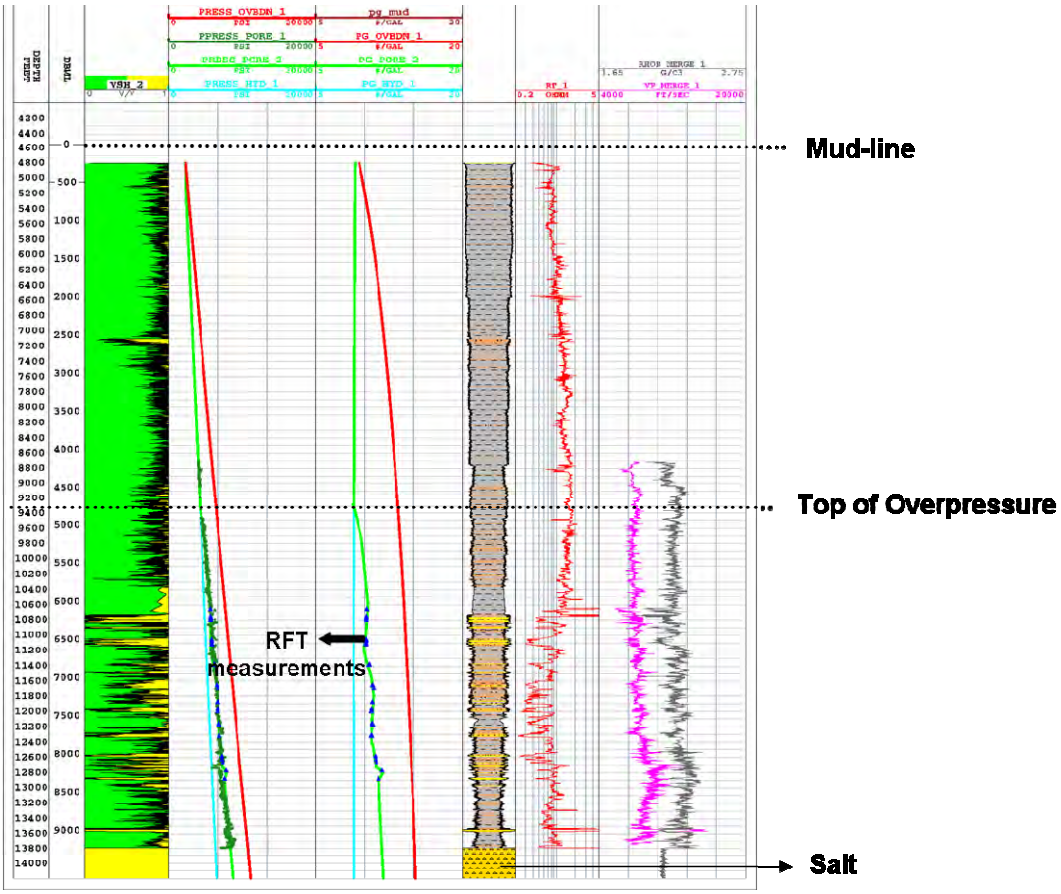

Figure 4.1: A typical well log from deep-water environment, Gulf of Mexico. No velocity and density data are available in the shallow section. The deeper interval is overpressured: the pore pressure as measured by repeat formation tester (RFT) is higher than the hydrostatic pressure.

We have organized this chapter into three sections. First we discuss the data used to compute the compaction trends and the petrophysical analysis of borehole data. Next we compute empirical trends of porosity and elastic properties (V_P, V_S and V_P/V_S ratio) for shales and sandstones. Finally we show how these empirical trends in sandstones agree with predictions of an effective-medium model (extended Walton model) combined with appropriate coordination number, porosity, and pressure relations.

4.3 Data Integration and Petrophysical Analysis

To obtain the compaction depth trends in shallow sediments, we integrate measurements of density, porosity, and compressional and shear wave velocities from the following sources:

(1) Conventional LWD measurements (Green Canyon, GOM).

(2) P-wave velocity measurements (Green Canyon, GOM) using isonic (sonic-while-drilling) tool. This tool records acoustic waveforms which are monopole.

(3) Density measurements using soil boring tool and borehole gravimeter in geotechnical boreholes (Green Canyon, GOM).

(4) Porosity and P-wave velocity measurements on cores (GOM). The measurements on shale are compiled using the data from Gregory, 1977; Hamilton, 1965 and Hamilton, 1979. For sandstones, we combine the experimental data from Gregory, 1977; Hamilton, 1979 and Paxton, 2002, along with the other datasets.

(5) Density, P-wave velocity and S-wave velocity measurements on unconsolidated, clean sandstones by Zimmer (2003) at low effective pressures (0 to 20 MPa).

The sequence of loading, unloading, and reloading corresponds to sedimentation, erosion and re-sedimentation in a basin (Nygård et al., 2004). The behavior during unloading and reloading is very different from that during the first loading (Zimmer, 2003). When the pre-consolidation stress is exceeded, the subsequent stress-strain curve follows the ‘virgin’ or ‘normal-compaction’ curve. This curve is much steeper than the unloading and reloading curves. In the present study, we consider experimental data during the loading cycles.

The down-hole data are processed and interpreted for identification of different lithologies, especially clean sands, shales and salts. To do this, we perform detailed petrophysical analysis of wells containing shallow and intermediate log data, and of geotechnical measurements. In the study area, some of the wells encounter salt at shallow depths. The compaction history of sediments beneath salt is different from that of the supra-salt sediments. In the present study, we focus on the supra-salt section. Figure 4.2 and Figure 4.3 show data from the shallow interval in two boreholes with isonic compressional velocity and geotechnical density measurements, respectively. The volume of shale (vshale) is carefully interpreted from gamma-ray, neutron and resistivity logs whenever they are available. For the purpose of our study, it is crucial to identify any anomalous zone that deviates from normal compaction trend based on petrophysical analysis. For example, we observe an anomalous interval at a depth ~1500 feet where resistivity and velocity are significantly lower than the background trend (Figure 4.2). The similar depth interval in the study area is characterized by higher porosity than the background in a different borehole (Figure 4.3). This interval corresponds to an overpressure zone owing to the presence of shallow water flow sands. Identification of such anomalous zones is valuable for our study, so that we exclude these zones when establishing the normal compaction trend.

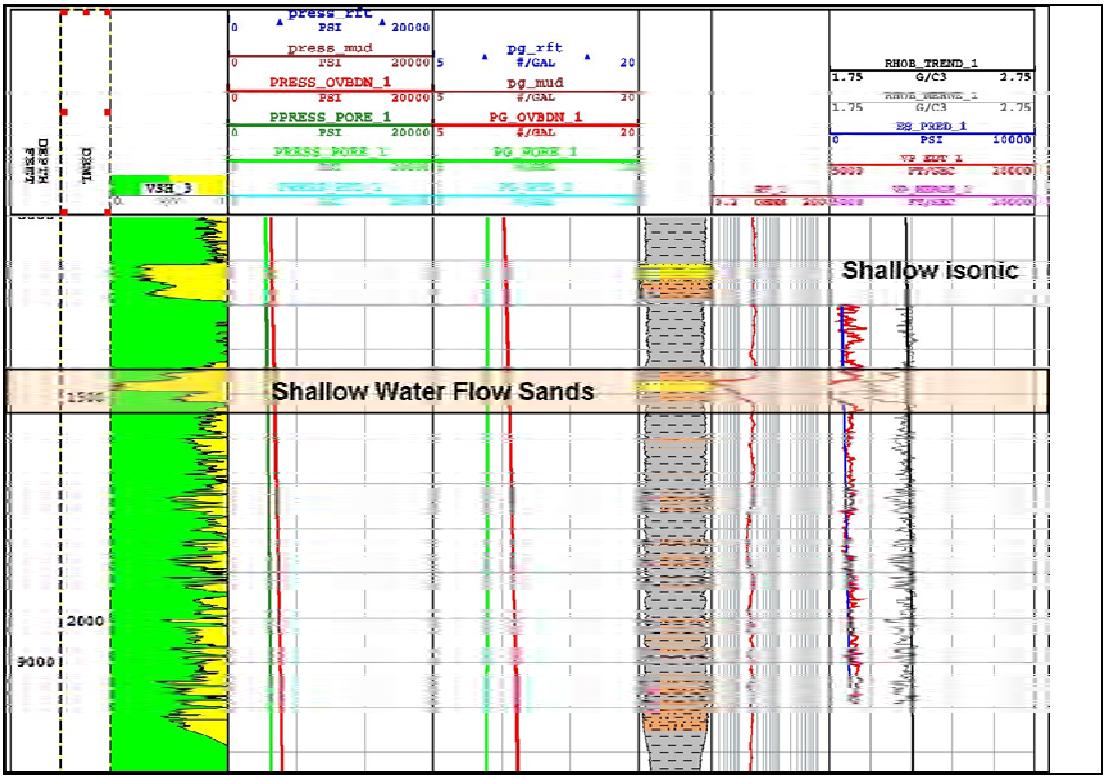

Figure 4.2: Example of a well log showing shallow isonic measurements that were used to compute velocity-depth-pressure trend. The interval of shallow water flow (SWF) sands is highlighted by the shaded rectangle. Note that resistivity and velocity deviate from their normal trends in SWF sands.

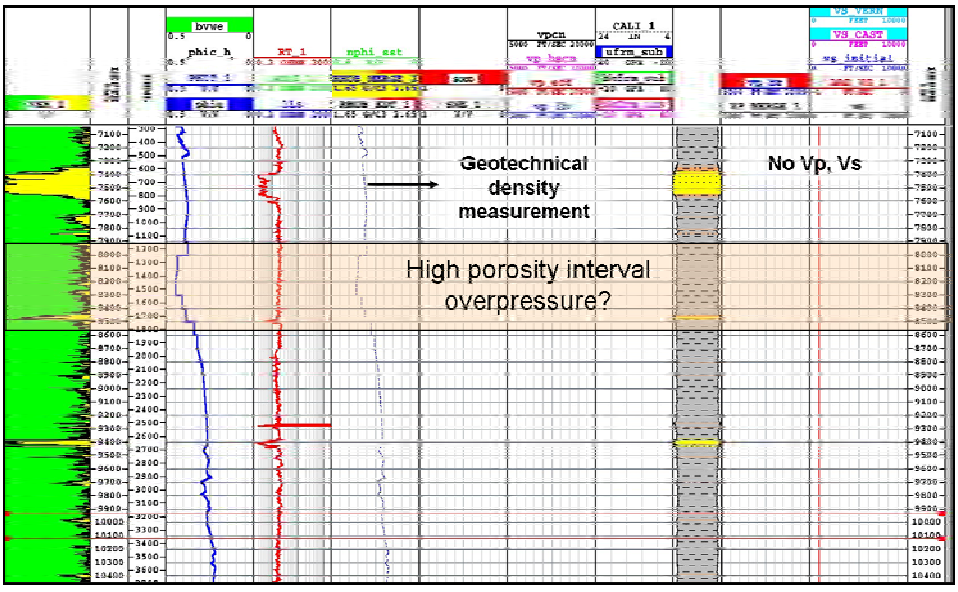

Figure 4.3: Example of a borehole with density measurements that were used to compute porosity-depth-pressure trend. The probable interval of overpressure associated with shallow water flow (SWF) sands is highlighted by the shaded rectangle. Note that density and porosity deviate from their normal trends in SWF sands.

We follow Terzaghi's effective stress principle to compute the effective pressure, which is simply defined as the difference between the overburden pressure and the pore fluid pressure (Terzaghi and Peck, 1967). The pore pressure is calibrated with repeat formation tester (RFT) measurements whenever they are available.

4.4 Results

We identify the normal compaction trends for shale and sandstones in the shallow, supra-salt section at Gulf of Mexico. We present the depth trends for (A) porosity, (B) velocities (V_P and V_S), and (C) V_P/V_S ratio. The depth trends of rock properties can also be represented in terms of effective pressure. We obtain the following empirical relation that relates effective pressure for normally compacted sediments to equivalent depth in the study area:

$$d = 2P + 180 \tag{4.1}$$

where d =depth below mud-line (ft) and P= effective pressure in psi/ft. Equation 4.1 is computed using several well data for shale and clean sandstones from Green Canyon, Gulf of Mexico .

4.4.1 Porosity-depth trends

Compaction disequilibrium (under-compaction) is known as the most dominant mechanism for overpressure development in clastic basins and deepwater environment (Dutta, 2002). In order to predict pore pressure build-up in sediments due to compaction disequilibrium, it is necessary to establish a trend curve for porosity versus depth due to normal compaction. One commonly used approach is based on Athy's (1930) porosity vs. depth relationship:

$$\phi = \phi_0 e^{-cZ} \tag{4.2}$$

where ϕ is the porosity at depth Z, ϕ_0 is the depositional porosity (i.e., critical porosity) at the mud-line (Z=0), and c is a constant.

Although several empirical results for porosity versus depth trends are available in the literature (e.g., Rubey and Hubbert, 1959; Rieke and Chilingarian, 1974; Hansen, 1996a; Hermanrud, 1998), they often lack calibration data in the shallow section. The porosity-depth trends in sands and shales during early burial are mostly affected by packing and ductile grain deformation (Surdam et al., 1989). Although cementation may occur during shallow burial (Dutton and Diggs, 1990), it is more common at higher burial depths. Diagenesis of shales is restricted to mechanical compaction during shallow burial (less than ~80 degree C). Chemical processes in shales begin at an intermediate diagenetic level (80-140 degree C), including transformation of smectite to illite and liberation of organic acids from organic matter. Ramm and Bjoerlykke (1994) suggested a clay dependent regression equation (equation 4.3) for Norwegian shelf sand and shale data which is valid for mechanical compaction at shallow depths.

$$\phi = 45e^{-(0.23+(0.27Cl))Z} \tag{4.3}$$

where Cl = total clay relative to total stable framework grains. For clean sandstones, $Cl = 0$.

We show porosity-depth trends for the Gulf of Mexico shale and clean sandstones in Figure 4.4a and Figure 4.4b, respectively. For shales, porosities measured by Gregory (1977) and Hamilton (1979) agree nicely with porosities derived from density measurements in geotechnical boreholes in the shallow section (0 to 3000 ft). These data are integrated with log-derived porosities in intermediate depths (3000 to 6000 ft) to establish the normal porosity-depth trend. Figure 4.4a shows an interval of anomalously higher porosity than background at a depth ~1500 ft. This interval corresponds to the shallow-water flow (SWF) regime, and is therefore excluded from computation of the normal compaction trend. For sandstones, porosity measured by Gregory (1977) and Paxton (2002) agree with porosity computed using geotechnical measurements in the shallow section (0 to 3000 ft), as well as, porosity measured by Zimmer (2003) at low effective pressure. Log-derived porosities at intermediate depth usually show scatter due

to silt content, but they agree reasonably with the mean trend of other data sources.

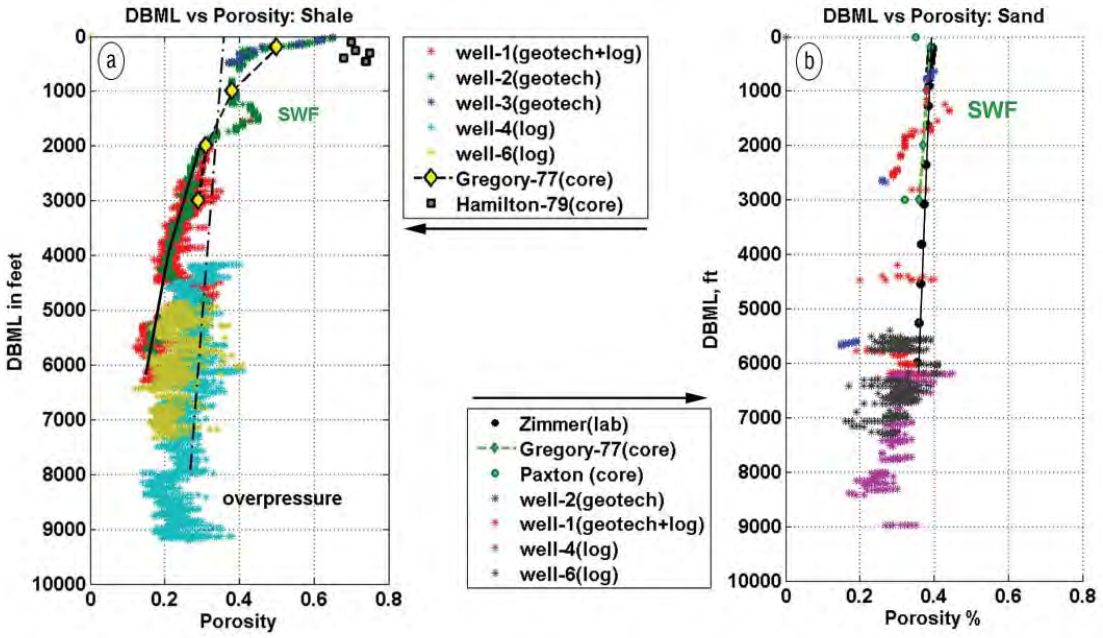

Figure 4.4 (a) Porosity-depth trends in shale (left). The anomalously higher than background porosity at a depth of 1500 ft in well-2 corresponds to shallow-water flow (SWF). The log data from well-4 and well-6 are overpressured. The porosity-depth relation derived using deeper section of log data underpredicts porosity in the shallow section. (b) Porosity-depth trends in clean, brine sandstones (right).

We observe that the trend of porosity reduction in the shallow section is different for shale and sandstones. Here, porosity decreases more rapidly in shale than in sandstones primarily due to the dewatering process. The existing porosity-depth relation derived using deeper section of log data (e.g., Wendt model) is not applicable in the shallow section, especially for shales. We fit a general exponential equation of the following form to get porosity-depth empirical trends:

$$\phi = ae^{bZ} + ce^{dZ} \tag{4.4}$$

Z= DBML (depth below mud-line) in feet. We use the same functional form as shown in equation 4.4 to compute depth trends for V_P, V_S and V_P/V_S ratio. The coefficients are shown in Table 4.1. Although an exponential equation with just one term has been

reported earlier (e.g., equation 4.2), we require two terms to better fit the rapid change of rock-properties in shallow subsurface.

4.4.2 Velocity-depth trends

Estimates of overpressure and amount of exhumation based on sonic data for a sedimentary formation rely on identification of a normal velocity–depth trend (e.g., Scherbaum, 1982). Such trends describe how sonic velocity increases with depth in relatively homogeneous, brine-saturated sedimentary formations as porosity is reduced during normal compaction. Storvoll et al. (2005) estimated linear velocity-depth trend lines for sandstones and shales on the Norwegian shelf using well log data. However, the trends for the shallow section (0 to 500 meters) were extrapolated using the data from deeper section.

Figure 4.5a and Figure 4.5b show our V_P-depth trends for shale and sands respectively for the Gulf of Mexico. Figure 4.5a shows that V_P measurements in shales by Gregory (1977) and Hamilton (1965, 1979) provide useful calibrations in the shallow section. They agree with the V_P obtained from isonic measurements in the shallow subsurface, and also match with the well-log velocities at greater depth. The shallow sub-surface is mostly dominated by shale; hence log data for sandstones tends to be rare. Therefore, velocity measurements on sandstones using core from Gulf of Mexico (Gregory 1977, Hamilton 1979) and experimental data from Zimmer (2003) on unconsolidated sands provide valuable calibrations for computing V_P -depth trends in the shallow sub-surface (Figure 4.5b).

There are fewer data for describing V_S-depth trends since it is difficult to measure shear wave velocities in the shallow section. The V_S-depth trend for shale (Figure 4.6a) is obtained from log data only, and no calibration data is available above 1000 ft. DBML. The V_S above this depth is extrapolated, assuming shear wave velocity approaches zero at the mud-line. This assumption is based on the critical-porosity concept (Nur et al., 1998), which suggests that sediments approach Reuss average (Reuss, 1929) at critical-porosity. The porosity of sediments immediately below the mud-line corresponds to critical

porosity (or depositional porosity). For sandstones, no V_S measurements are available in shallow depths at the wells. Hence, the V_S measurements by Zimmer (2003) on unconsolidated sandstones conducted at low effective pressures (0 to 20 MPa) contribute significantly in computing V_S -depth trend (Figure 4.6 b). We use equation 4.1 to convert effective pressures to equivalent depths.

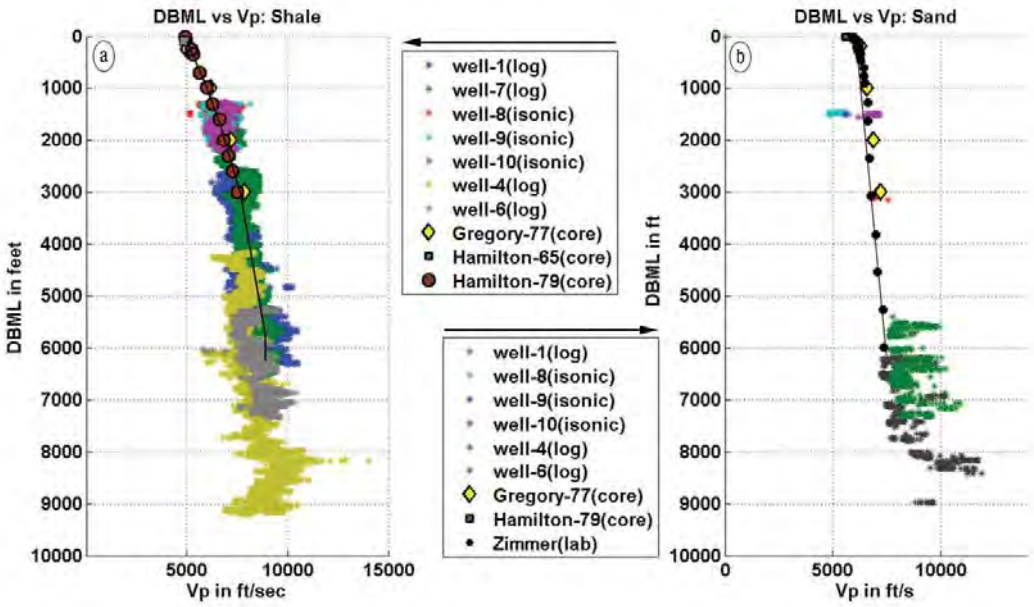

Figure 4.5: (a) V_P-depth trends in shale (left) ; (b) V_P-depth trends in clean, brine-sands (right). The velocity measurements on the Gulf of Mexico core provide useful calibrations at shallow depths.

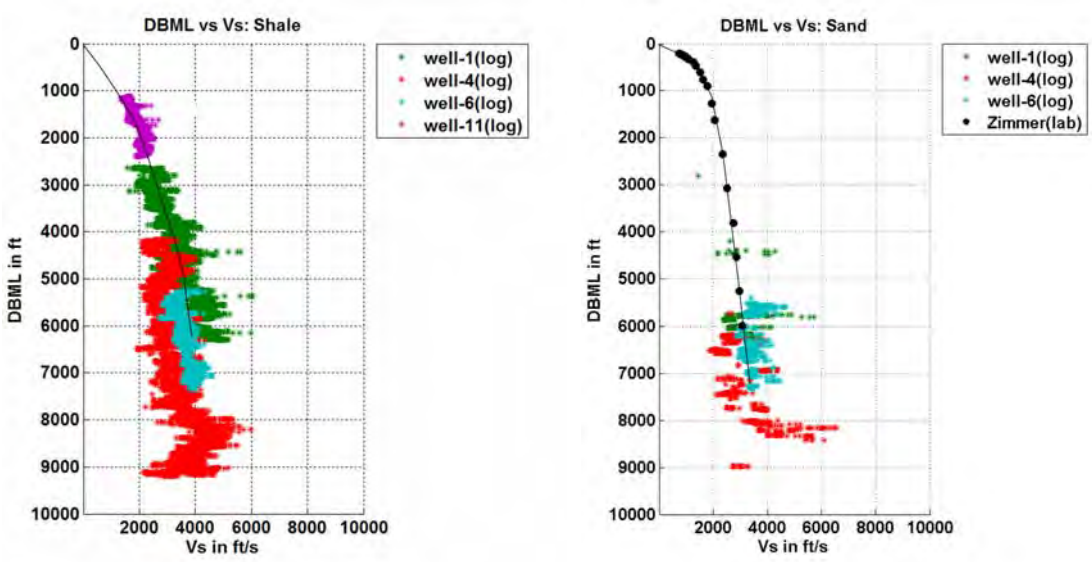

Figure 4.6: (a) V_S-depth trends in shale (left); (b) V_S-depth trends in clean, brine-sands (right). The velocity measurements on unconsolidated sands by Zimmer (2003) provide useful calibrations at shallow depths.

4.4.3 V_P/ V_S - depth trends

The V_P/V_S ratio (which is directly related to Poisson's ratio) is a key parameter that relates to low effective pressure or high pore pressure, especially under shallow-water flow conditions. Poor grain-to-grain contacts in overpressured zones with low effective stress affect the S-velocity more than the P-velocity (Dutta et al., 2002). In overpressured (softer) sediments, the V_P/V_S ratio is usually higher than the background trend. This has been observed in laboratory experiments (Domenico, 1984). The depth trend of V_P/V_S ratio is shown in Figure 4.7. For shales, we observe an anomalous interval of low V_P/V_S at depth 1500 - 2200 ft (Figure 4.7a). This anomaly corresponds to partial gas saturation, as evident from core observations at that particular well. V_P/V_S measurements are not available in shale at depth above 1000 ft due to lack of V_S measurements, and we extrapolate using critical-porosity concepts. For sandstones, measurements by Zimmer (2003) provide useful calibrations for computing V_P/V_S-depth trends. We observe that V_S decreases much faster than V_P at shallow depth, and V_P/V_S can be as high as 10 in the sediments immediately below mud-line (Figure 4.7b).

An exponential equation similar to equation 4.4 is used to describe depth trends of

V_P, V_S, and V_P/V_S ratio. The coefficients are shown in Table 4.1. Equation 4.1 can be used along with these coefficients to represent trends of rock-properties in terms of effective pressure.

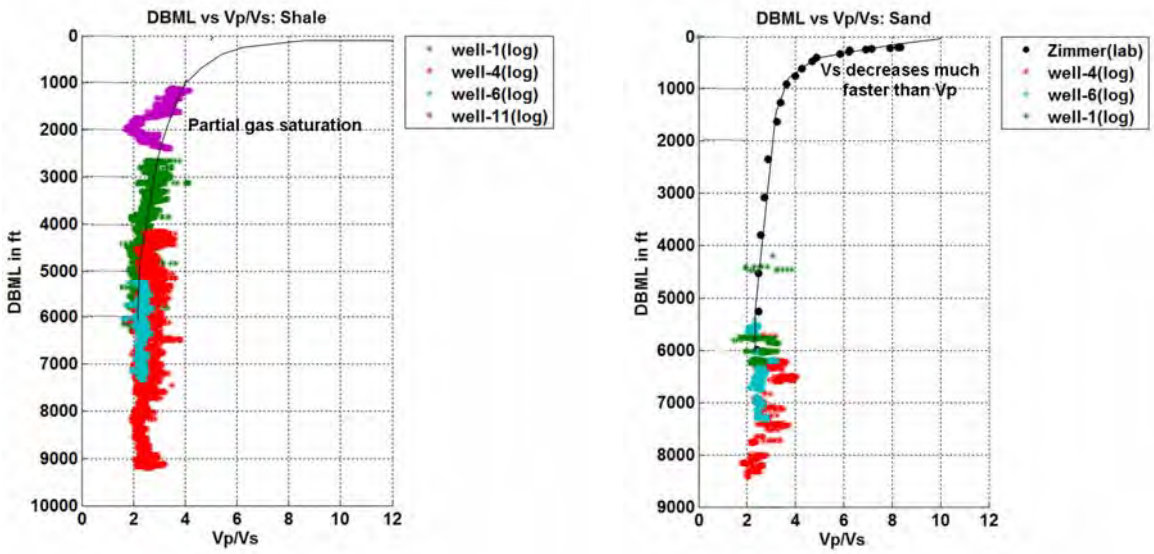

Figure 4.7: (a) V_P/V_S -depth trends in shale (left); (b) V_P/V_S -depth trends clean, brine-sands (right). V_S decreases much faster than V_P at low pressure/ shallow depth. V_P/V_S can be as high as 10 in the shallow sands immediately below mud-line.

Figure 4.8a and b explore the V_P-V_S relations in shale and sand respectively. Vernik's V_P-V_S equation for shale (Vernik et al, 2002) and the mud-rock relation by Greenberg and Castagna (1992) agree with the mean trend of log data from the Gulf of Mexico shales (Figure 4.8a). However, the V_P-V_S relation by Greenberg and Castagna for sandstone fails to predict the trend for sandstones, especially at shallow depths (grey points in Figure 4.8b). Vernik's V_P-V_S equations differ from Greenberg and Castagna at shallow depths since they honor the critical-porosity concept. We find that Vernik's V_P-V_S equation for sandstone is similar to Greenberg and Castagna at intermediate depths, but provides a better prediction at shallow depths.

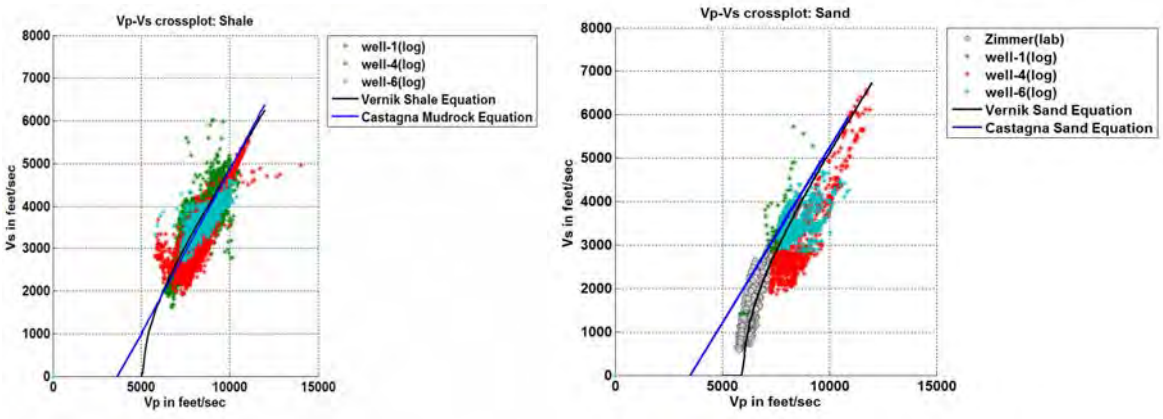

Figure 4.8: (a) V_P-V_S crossplot in shale (left); (b) V_P-V_S crossplot clean, brine-sands (right). In the shallow sediments, Vernik's V_P-V_S relation (Vernik et al, 2002) is more appropriate than Greenberg and Castagna (1992) relation.

Table 4. 1: Empirical depth trends of rock-properties for shallow sediments. The depths are in ft, porosities in fraction, and the velocities in ft/sec.

Coefficients of exponential fits using a general exponential equation: Rock Property = $ae^{bZ} + ce^{dZ}$, where Z = depth below mud-line (DBML) in ft.						
Rock property	Lithology	coefficients of exponential fits				
		a	b	c	d	R^2
Porosity	Shale	0.2875	-0.00774	0.4384	-0.0001761	0.97
Porosity	Clean, brine-sand	0.01132	-0.004874	0.3923	-1.678e-005	0.99
V_P	Shale	6917	4.633e-005	-1652	-0.0003646	0.82
V_P	Clean, brine-sand	6350	2.532e-005	-500.3	-0.003647	0.98
V_S	Shale	3540	1.2e-005	-3536	-0.000421	0.90
V_S	Clean, brine-sand	1951	7.962e-005	-1788	-0.001942	0.99
V_P/ V_S	Shale	14.86	-0.001911	2.714	-4.028e-006	0.90
V_P/ V_S	Clean, brine-sand	19.67	-0.007416	4.094	-0.0001182	0.99

4.4.4 Effective-medium modeling for velocity-depth trends in clean sands

An understanding of rock physics models is important for a reliable prediction of pore pressure in shallow sediments. Japsen (2000) investigated the relations between rock physics models and velocity-depth trends for normal compaction. He presented baselines for sandstones and shales based on the modified Voigt trend, and on a constrained time-average equation, respectively. Avseth et al (2001) showed that the Hertz-Mindlin theory (Mindlin, 1949; Mavko et al., 1998) can be applied to predict normal velocity-depth

trends in unconsolidated sediments. However, the modeling approach by Avseth et al (2001) lacked calibration data above ~6000 ft. In this chapter, we use the extended-Walton model along with new coordination number, porosity, pressure relations to compute velocity-depth trends in clean, dry sandstones. The coordination number represents average number of grain contacts in a granular pack. Next, Gassmann's fluid substitution (Gassmann, 1951) is performed to obtain depth trends in brine sandstones.

The Walton model (Walton, 1987) predicts effective elastic moduli for two special cases: infinitely rough spheres (friction coefficient is very large) and ideally smooth spheres (friction coefficient is zero). Jenkins et al. (2005) expressed the effective elastic moduli of Walton model as follows:

$$\lambda_{eff}^{w} = \frac{C(1-\phi)}{5\pi}\frac{G}{(1-\nu)}\left[\frac{3\pi}{2}\frac{(1-\nu)}{(1-\phi)C}\frac{P}{G}\right]^{1/3}\frac{[2-\nu-2\alpha(1-\nu)]}{(2-\nu)} \tag{4.5}$$

$$G_{eff}^{w} = \frac{C(1-\phi)}{5\pi}\frac{G}{(1-\nu)}\left[\frac{3\pi}{2}\frac{(1-\nu)}{(1-\phi)C}\frac{P}{G}\right]^{1/3}\frac{[2-\nu+3\alpha(1-\nu)]}{(2-\nu)} \tag{4.6}$$

where C is the coordination number, ϕ is the porosity, G is the grain shear modulus and P is the effective pressure. When α is zero, we obtain the Walton smooth model, where all the grains have zero friction at their contacts. When α is equal to 1, we obtain Walton rough model, which considers infinitely high friction at the grain contacts of identical spheres. Since the effective shear modulus (G_{eff}) of a granular aggregate is linearly proportional to tangential stiffness, it is possible to lower G_{eff} by assuming tangential stiffness is zero for some fraction of the grains. We use equations 4.5 and 4.6 to represent this scenario, where α represents the fraction of completely adhered contacts, and (1-α) represents the fraction of completely slipping contacts. We refer to this as the extended Walton model. Note that mixing of frictional and non-frictional grains can also be achieved assuming some of the grains have zero tangential stiffness in the Hertz-Mindlin effective medium model (Bachrach et al., 2000).

We use the extended Walton model (α = 0.6) to invert the coordination number (C)

from measurements on dry, unconsolidated sandstones by Zimmer (2003). We choose this particular value of α since it provides realistic prediction of C for a random pack of grains. The relations between C-porosity and C-pressure are expressed as:

$$C_P(\phi) = (-2.338\text{e}-014)\phi^{9.099} + 14.45 \tag{4.7}$$

$$C_S(\phi) = (-1.798\text{e}-014)\phi^{9.099} + 11.02 \tag{4.8}$$

$$C_P(P) = (777.1)P^{0.001545} - 770.7 \tag{4.9}$$

$$C_S(P) = (-4.457)P^{-0.2724} + 9.401 \tag{4.10}$$

where, C_P and C_S represent coordination numbers to predict V_P and V_S, respectively. ϕ is porosity in percentage, and P is effective pressure in MPa. We find that prediction of V_S requires a lower value of C than the prediction of V_P.

We apply the above C_P-pressure and C_S-pressure relations (equations 4.9 and 4.10) to the extended Walton model (α =0.6) to predict the velocities as a function of pressure. Figure 4.9 shows that both V_P and V_S predictions by this model agree nicely with the integrated datasets at shallow depths.

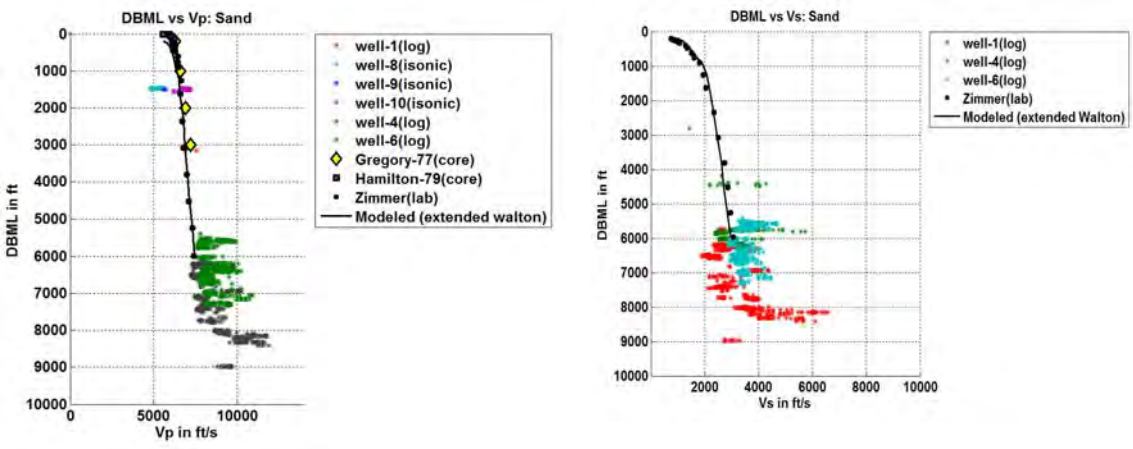

Figure 4.9: (a) V_P -depth trends in clean, brine-sands (left); (b) V_S -depth trends clean, brine-sands (right). The solid line represents velocity predictions using the extended Walton model with appropriate coordination number-pressure relations.

4.5 Conclusions

We provide normal compaction depth trends of porosity, velocities, and V_P/V_S ratio for shallow, supra-salt sediments in the Gulf of Mexico. For this, we combine data from multiple sources, such as, isonic, geotechnical and core measurements from shallow sections of Gulf of Mexico, and laboratory measurements on unconsolidated sands conducted at low effective pressure. However, the lack of conventional log data remains a challenge for calibration of these trends with log values at the shallow depth. We find that the trends of rock properties in shallow subsurface can be drastically different from that of the deeper section. Therefore, simple extrapolation of depth trends upwards, computed using data from the deeper section, can lead to erroneous results in the shallow section. Furthermore, we offer an effective medium modeling approach for clean sands using appropriate coordination number-pressure-porosity relations in the extended Walton model. These results can be useful in establishing normal compaction trends in the shallow sub-surface, where log data are usually not available and are of poor quality. Establishing such trend curves is important in seismic exploration for several reasons, especially for detecting drilling hazards and distinguishing shallow resource-potential prior to drilling in deep-water environment.

4.6 Acknowledgements

The authors sincerely thank BP for permission to use the borehole data from Gulf of Mexico. We thank Juan Florez, Richard Weiland, J.P.Blangy from BP for valuable discussions. A special thank to James Packwood (formerly at BP) for his guidance with detailed petrophysical analysis. This work was supported by the Stanford Rock Physics and Borehole Geophysics project and DOE contract DE-FC26-04NT15506.

4.7 References

Acheson, C.H., 1963, Time-depth and velocity-depth relations in western Canada: Geophysics, 28, 894–909.

Al-Chalabi, M., 1997a, Instantaneous slowness versus depth functions: Geophysics, 62, 270–273.

Al-Chalabi, M., 1997b, Time-depth relationships for multilayer depth conversion: Geophysical Prospecting, 45, 715–720.

Athy, L.F., 1930, Compaction and oil migration: American Association of Petroleum Geologists Bulletin, 14, 25–35.

Avseth, P., Mavko, G., Dvorkin, J., and Mukerji, T., 2001, Rock physics and seismic properties of sands and shales as a function of burial depth: Expanded Abstracts, 71st SEG Annual Meeting.

Bachrach, R., J. Dvorkin, and A. Nur, 2000, Seismic velocities and Poisson's ratio of shallow unconsolidated sands: Geophysics, 65, 559–564.

Bulat, J., and Stoker, S.J., 1987, Uplift determination from intervalvelocity studies, UK, southern North Sea, in J. Brooks, and K.W. Glennie, eds., Petroleum geology of north west Europe: London, Graham and Trotman, 293-305.

Greenberg, M.L., and Castagna, J.P., 1992, Shear-wave velocity estimation in porous rocks: Theoretical formulation, preliminary verification and applications: Geophysical Prospecting, 40, 195-209.

Corcoran, D.V., and Dor´e, A.G., 2005, A review of techniques for the estimation of magnitude and timing of exhumation in offshore basins: Earth-Science Reviews, 72, 129–168.

Corcoran, D.V., and Mecklenburgh, R., 2005, Exhumation of the Corrib gasfield, Slyne Basin, offshore Ireland: Petroleum Geoscience, 11, 239–256.

Domenico, S. N., 1984, Rock lithology and porosity determination from shear and compressional wave velocity: Geophysics, 49, 1188-1195.

Dutta, N. C., 2002, Deepwater geohazard prediction using prestack inversion of large offset P-wave data and rock model: The Leading Edge, 193-198.

Dutta, T., Mukerji, T., Mavko, G., Lane, T., 2009, Compaction trends for shale and clean sandstone in shallow sediments, Gulf of Mexico: The Leading Edge, 28, 260-266.

Dutton, S.P., and Diggs, T.N., 1990, History of quartz cementation in the Lower Cretaceous Travis Peak Formation, East Texas: Journal of Sedimentary Petrology, 60, 191-202.

Faust, L.Y., 1951, Seismic velocity as a function of depth and geologic time: Geophysics, 16, 192–206.

Gassmann, F., 1951, Uber die elastizitat poroser medien: Veirteljahrsschrift der Naturforschenden Gesellschaft, 96, 1-23.

Greenberg, M.L., and Castagna, J.P., 1992, Shear-wave velocity estimation in porous rocks: Theoretical formulation, preliminary verification and applications: Geophysical Prospecting, 40, 195–209.

Gregory, A. R., 1977, Aspects of rock physics from laboratory and log data that are important to seismic interpretation, in Seismic stratigraphy application to hydrocarbon exploration: AAPG Memoir 26.

Hamilton, E. L., 1965, Sound speed and related physical properties of sediments from experimental Mohole (Guadalupe site): Geophysics, 30, 257-261.

Hamilton, E. L., 1971, elastic properties of marine sediments: J. Geophys. Res., 76, 579-604.

Hamilton, E. L., 1979, V_P / V_S and Poisson's ratio in marine sediments and rocks: Journal of Acoustic Society of America, 66, 1093–1081.

Hansen, S., 1996a, A compaction trend for Cretaceous and Tertiary shales on the Norwegian Shelf based on sonic transit times: Petroleum Geoscience, 2, 159–166.

Hansen, S., 1996b, Quantification of net uplift and erosion on the Norwegian Shelf south of 66◦N from sonic transit times of shale: Norsk Geologisk Tidsskrift, 76, 245–252.

Heasler, H.P., and Kharitonova, N.A., 1996, Analysis of sonic well logs applied to erosion estimates in the Bighorn Basin, Wyoming: American Association of Petroleum Geologists Bulletin, 80, 630–646.

Hermanrud, C., L. Wensaas, G. M. G. Teige, H. M. N. Bolas, S. Hansen, and E. Vik, 1998, Shale porosities from well logs on Haltenbanken (offshore mid-Norway) show no influence of overpressuring, in B. E. Law, G. F. Ulmishek, and V. I. Slavin, eds., Abnormal pressures in hydrocarbon environments: AAPG Memoir 70, 65– 85.

Hillis, R.R., 1995, Quantification of Tertiary exhumation in the United Kingdom southern North Sea using sonic velocity data: American Association of Petroleum Geologists Bulletin, 79, 130–152.

Hottmann, C.E., and Johnson, R.K., 1965, Estimation of formation pressures from log-derived shale properties, Journal of Petroleum Technology, 17, 717–723.

Mindlin, R.D., 1949, Compliance of elastic bodies in contact: Trans. ASME, 71, A-259.

Paxton, S. T., Szabo, J. O., Ajdukiewicz, J. M., and Klimentidis, R. E., 2002, Construction of an intergranular volume compaction curve for evaluating and predicting compaction and porosity loss in rigid-grain sandstone reservoirs: AAPG Bulletin, 86, 2047-2067.

Japsen, P., 1993, Influence of lithology and Neogene uplift on seismic velocities in Denmark; implications for depth conversion of maps: American Association of Petroleum Geologists Bulletin, 77, 194–211.

Japsen, P., 1998, Regional velocity-depth anomalies, North Sea Chalk, A record of overpressure and Neogene uplift and erosion: American Association of Petroleum Geologists Bulletin, 82, 2031–2074.

Japsen, P., 1999, Overpressured Cenozoic shale mapped from velocity anomalies relative to a baseline for marine shale, North Sea: Petroleum Geoscience, 5, 321–336.

Japsen, P., 2000, Investigation of multi-phase erosion using reconstructed shale trends based on sonic data, Sole Pit axis, North Sea: Global and Planetary Change, 24, 189–210.

Jenkins, J., Johnson, D., Ragione, L. La., and Makse, H., 2005, Fluctuations and the effective moduli of an isotropic, random aggregate of identical, frictionless spheres: Journal of the Mechanics and Physics of Solids, 53, 197- 225.

Lander, R.H., and Walderhaug, O., 1999, Predicting porosity through simulating sandstone compaction and quartz cementation: American Association of Petroleum Geologists Bulletin, 83, 433–449.

Mackay, L.M., and White, N.J., 2006, Accurate estimates of the spatial pattern of denudation by inversion of stacking velocity data: An example from the British Isles: Geochemistry, Geophysics and Geosystems, 7, Q10007, 1–34.

Magara, K., 1976, Thickness of removed sedimentary rocks, paleopore pressure, and paleotemperature, southwestern part of Western Canada Basin: American Association of Petroleum Geologists Bulletin, 60, 554–565.

Magara, K., 1978, Compaction and Fluid Migration, Practical Petroleum Geology: Elsevier. Science Publishing Co.

Magara, K., 1980, Comparison of porosity-depth relationships of shale and sandstone: Journal of Petroleum Geology, 3, 175-185.

Mavko, G., Mukerji, T., and Dvorkin, J., 1998, The Rock Physics Handbook, tools for seismic analysis in porous media: Cambridge University press.

Mindlin, R.D., 1949, Compliance of elastic bodies in contact: Trans. ASME, 71, A-259.

Nur, A., Mavko, G., Dvorkin, J., and Galmundi, D., 1998, Critical porosity; a key to relating physical properties to porosity in rocks: The Leading Edge: 17, 357–362.

Nygård, R., Guttierrez, M., Høeg, K., and Bjørlykke, K., 2004, Influence of burial history on microstructure and compaction behaviour of Kimmeridge Clay: Petroleum Geoscience, 10 , 269 –270.

Ramm, M., and Bjørlykke, K., 1994, Porosity/depth trends in reservoir sandstones: assessing the quantitative effects of varying pore-pressure, temperature history and mineralogy, Norwegian Shelf data; Clay minerals, 29, 475-490.

Rieke, H.H., and Chilingarian, G.V., 1974, Compaction of argillaceous sediments: Amsterdam, Elsevier.

Rubey, W., and Hubbert, M. K., 1959, Role of fluid pressure in mechanics of overthrust faulting: Geol. Soc. Amer. Bull., 70, 167-206.

Scherbaum, F., 1982, Seismic velocities in sedimentary rocks; indicators of subsidence and uplift: Geologische Rundschau, 71, 519–536.

Slotnick, M.M., 1936, On seismic computations, with applications: Geophysics, 1, 299–305.

Smith, T., and Sondergeld, C.H., 2001, Examination of AVO response in the eastern deepwater Gulf of Mexico: Geophysics, 66, 1864–1876.

Storvoll, V., Bjørlykke, K., and Mondol, N.H., Velocity-depth trends in Mesozoic and Cenozoic sediments from the Norwegian Shelf: AAPG Bulletin, 89; 359-381.

Surdam, R.S., Dunn, T.L., MacGowan, D.B., and Heasler, H.P., 1989, Conceptual models for the prediction of porosity evolution with an example from the Frontier Sandstone, Bighorn Basin, Wyoming, In Petrogenesis and petrophysics of selected sandstone reservoirs of the Rocky Mountain region: Rocky Mountain Association of Geologists.

Vernik, L., Fisher, D., and Bahret, S., 2002, Estimation of net-to-gross from P and S impedance in deepwater turbidites: The Leading Edge, 21, 380-387.

Walford, H.L., and White, N.J., 2005, Constraining uplift and denudation of west African continental margin by inversion of stacking velocity data: Journal of Geophysical Research-Solid Earth, 110, B04403, 1–16.

Walton, K., 1987, The effective elastic moduli of a random pack of spheres: J. Mech. Phys. Sol., 35, 213-226.

Ware, P.D., and Turner, J.P., 2002, Sonic velocity analysis of the Tertiary denudation of the Irish Sea basin: Exhumation of the North Atlantic Margin: Timing, Mechanisms and Implications for Petroleum Exploration, 196 (eds A. G. Dor´e, J. A. Cartwright, M. S. Stoker, J. P. Turner, N. White), 355–370.

Terzaghi, K., and Peck, R.P., 1967, Soil Mechanics in Engineering Practice: John Wiley ans Sons, Inc.

Zimmer, M., 2003, Seismic velocities in unconsolidated sands: Measurements of pressure, sorting, and compaction effects: Ph.D. dissertation, Stanford University.

Chapter 5
Quantifying Spatial Trends of Sedimentological Parameters in Channelized Turbidite, West Africa

"The important thing is not to stop questioning. Curiosity has its own reason for existing. One cannot help but be in awe when he contemplates the mysteries of eternity, of life, of the marvelous structure of reality. It is enough if one tries merely to comprehend a little of this mystery every day. Never lose a holy curiosity"
-- Albert Einstein

5.1 Abstract

Our overall goal is to improve the prediction of reservoir quality, by establishing links between conventional sequence stratigraphic interpretations and quantitative seismic amplitudes. In this chapter, we quantify the spatial trends of sand/shale ratios and sorting in laminated, channelized turbidite sequences, deposited within minibasin settings on the

continental slope of Equatorial Guinea, offshore West Africa. First, we identify probable spatial trends of sand/shale ratios and sorting as predicted by the conventional sequence stratigraphic model (spill-and-fill model). Next, these trends are evaluated using well data, and the same well data are used to calibrate the modified soft-sand model that provides links between P-impedance and quartz/clay ratios, and sorting. We observe a systematic variation of quartz/clay ratio and sorting from proximal to distal locations even within a single facies. The quartz/clay ratio in sand-rich facies spatially increases from 0.4 to 1 along the downdip flow. In addition, porosity at the distal location (~35 % to 40%) is higher than the porosity at the proximal location (~30 % to 35%) due to improvement in sorting. The spatial increase in sand/shale ratios and sorting within the sand-rich facies increases the magnitudes of class IV AVO intercept and gradient. The direct application of our results is that seismic attributes (e.g., P-impedance, AVO intercept and gradient) can be interpreted in terms of underlying sedimentological parameters, away from well locations.

5.2 Introduction

This chapter focuses on quantifying spatial variation of sedimentological parameters in channelized turbidite sequences, by combining an appropriate sequence stratigraphic model in a deep-water depositional system, and a rock physics model for the elastic properties in uncemented sands. Sequence stratigraphy is a geological interpretation tool for process/response events (Mulholland, 1998). It can predict the likely occurrence of reservoir facies, source rocks and seals. Conventional sequence stratigraphic interpretation from seismic data has been predominantly qualitative, based on visual inspection of geometric patterns in post-stack seismic data (Payton, 1977; Neal et al., 1993; Brown, 1984; Zeng et al., 1996). However, quantitative interpretation of seismic data is possible if we can extract information about sedimentological parameters, such as the mineralogical composition (quartz/clay ratio) and the textural maturity (sorting, grain angularity, sphericity and roundedness), and link them with seismic amplitudes using an appropriate rock physics model.

Rock physics modeling provides the fundamental basis for quantitative interpretation of seismic amplitudes in terms of sedimentological parameters (e.g., Castagna, 2001; Braaksma et al., 2002; Gutiérrez et al., 2002; Latimer et al., 2000; Avseth et al., 2005; Florez, 2005). In quantitative seismic interpretation, the input parameters in a rock physics model are calibrated at the well locations. However one of the major sources of uncertainty in rock physics modeling arises from our lack of knowledge about trends of model input parameters away from the wells.

Rock physics modeling away from the wells can improve using the spatial trends of sedimentological parameters as predicted by sequence stratigraphic interpretations. Various researchers have shown that sequence stratigraphy can provide predictive trends of spatial variations of sedimentological parameters away from the wells (e.g., Van Wagoner et al., 1990; Posamentier and Allen, 1993). However, it is essential to validate such predictive sequence stratigraphic trends using well data, and calibrate them with an appropriate rock physics model at the wells. Then we can benefit from spatial sedimentological trends guided by sequence stratigraphy, as well as the calibrated rock physics model to predict quantitative variation of sedimentological parameters away from the wells.

In this chapter, we have quantified the spatial trends of sand/shale ratios and sorting combining the spill-and-fill sequence stratigraphic model (Satterfield and Behrens, 1990; Winker, 1996) and the modified soft-sand model (discussed later in this chapter). The modified soft-sand model is similar to the soft-sand model with the exception that the effective moduli at the critical porosity are computed using a combination of Walton's rough and smooth models (Walton, 1987; Jenkins et al., 2005) along with empirical coordination number, porosity, and pressure relations as shown in Chapter 3.

The data used in this study are from offshore Equatorial Guinea, West Africa. The channelized, shaly sand sequences in our study area were deposited in minibasin settings (Dailly et al., 2002). We interpret that these shaly sands are laminated (interbedded) below the resolution of well logs using the Thomas-Stieber model (Thomas and Stieber, 1975), and validate our interpretation using core observations.

The spill-and-fill model in minibasin settings predicts an increase in sand/shale ratios and sorting along the flow direction in a turbidite channel (e.g., Brunt et al., 2004; Lerch et al., 2006). We quantify these spatial trends using the modified soft-sand model, after calibrating the model parameters at the well locations. The calibrated models are then used to interpret inverted P-impedance in terms of porosity and sand/shale ratio. The spatial increase in sand/shale ratios and sorting within the channel sand also provide distinct AVO signatures at the proximal versus the distal location, as evident from our model predictions and real data. We apply the results to quantify sand/shale ratio from observed AVO intercepts and gradients computed from partial stack volumes.

We have organized this chapter in four different sections. First, we present the spatial trends of sand/shale (quartz/clay) ratios and sorting as predicted from sequence stratigraphic models of deep-water channelized deposits. Next we use a comprehensive dataset from a similar depositional environment to interpret stratigraphic sequences, and identify the laminated (interbedded) nature of these turbidite sequences below well log resolution. We link spatial trends of sand/shale ratio and sorting with seismic amplitudes using an appropriate rock physics model, calibrated at the well locations. Finally, we apply the calibrated rock physics model for interpreting inverted P-impedance and AVO attributes in terms of sand/shale ratio and porosity, away from the wells.

5.3 Spatial trend of sedimentological parameters in channelized, turbidite environments

The spatial trends of sedimentological parameters in a specific depositional environment can be obtained from its analog using three different methods: outcrop observations, numerical simulations, and laboratory experiments. All of these methods in channelized, turbidite environments predict an increase in sand/shale ratios and improvement in sorting from proximal to distal location of a channel. Note that the spatial trends of sand:shale and sorting in channelized, turbidite environments are opposite from those in basin-floor environments (e.g., Bouma, 2001), which were previously studied by Avseth (2000). The details of sand:shale and sorting in

channelized, turbidite environments are discussed below.

Detailed outcrop studies of the internal facies architecture of deep-water systems are valuable to provide key predictive insights into analog intervals in the subsurface (e.g., Browne and Slatt 2002). Outcrop studies on submarine-canyon fills exposed at Wagon caves, California, show that median grain size and quartz/clay ratio decrease vertically upward (Anderson et al., 2006). Spatially, sorting improves from proximal to distal location due to segregation of clay from silt particles (Piper, 1978). The separation of charged clay flocs from silt particles is known as de-flocculation. The improved depositional sorting in the distal location can be explained by an increase in de-flocculation processes along the direction of sediment transport (Piper, 1978; Stow and Bowen 1980).

Numerical simulation of turbidity currents commonly agree with the trends from outcrop observations. For example, numerical simulation results with minibasin settings by Lerch et al. (2006) show that progressively better sorted materials are deposited at the distal location than the updip proximal location.

Laboratory experiments of turbidity currents support the sedimentological trends from the outcrop observations and the numerical simulations. For example, the laboratory experiments by Brunt et al. (2004) in minibasin settings predict a downdip increase in sand/shale ratios. They also demonstrate that progressively greater proportions of coarser sediments are spilled downstream as the degree of confinement is reduced in an updip minibasin. The spilling of coarser sediments from the updip minibasin and progressive filling in the downdip minibasin is referred as the spill-and-fill model (e.g., Satterfield and Behrens, 1990; Winker, 1996).

We use the predictive trends provided by the spill-and-fill model to identify the downdip increase in sand/shale ratios and sorting in our study area, which has the similar depositional environment with channelized turbidites developed in minibasin settings. The following section briefly describes the sequence stratigraphic setting of our study area.

5.4 Sequence stratigraphic setting of the study area

We use a comprehensive dataset from channelized turbidite sequences, which were deposited in offshore Equatorial Guinea (Rio Muni basin), West Africa. Figure 5.1 shows the location of the study area. The dataset includes post-stack seismic data, well logs, digital core images and detailed core descriptions. In addition, thin-sections, XRD, SEM and laser particle size analysis data are available in selected intervals at key wells.

Figure 5.1: Location of the study area (red rectangle) in offshore Equatorial Guinea, West Africa.

The sandstones in our study area were mostly deposited within the confines of submarine canyons in minibasin settings, and they constitute the primary exploration targets (Dailly et al., 2002). The deformation associated with diapirism and faulting in Equatorial Guinea gave rise to minibasin settings, in which a series of channelized turbidites developed (Dailly et al., 2002). Submarine canyons are important conduits for the transport of coarse-grained sediment into the deep sea on most continental margins (Shepard and Dill 1966; Normark and Carlson 2003). Stacked successions of coarse-grained, high-density turbidity current deposits and related architectural elements of

submarine canyon fills often constitute significant petroleum reservoirs (Anderson et al., 2006).

Figure 5.2 shows our interpretation of the present-day seabed mapped from 3D post-stack, time-migrated seismic data. The map of the seabed shows prograding deltas on the continental shelf, fluid escape features (pock marks) and incisions by the submarine channels on the continental slope. These incisions can create ~200 m of vertical relief. The geometry of a minibasin and turbidite channel can be observed from the vertical seismic section (Figure 5.2), as well as from the composite seismic section (Figure 5.3).

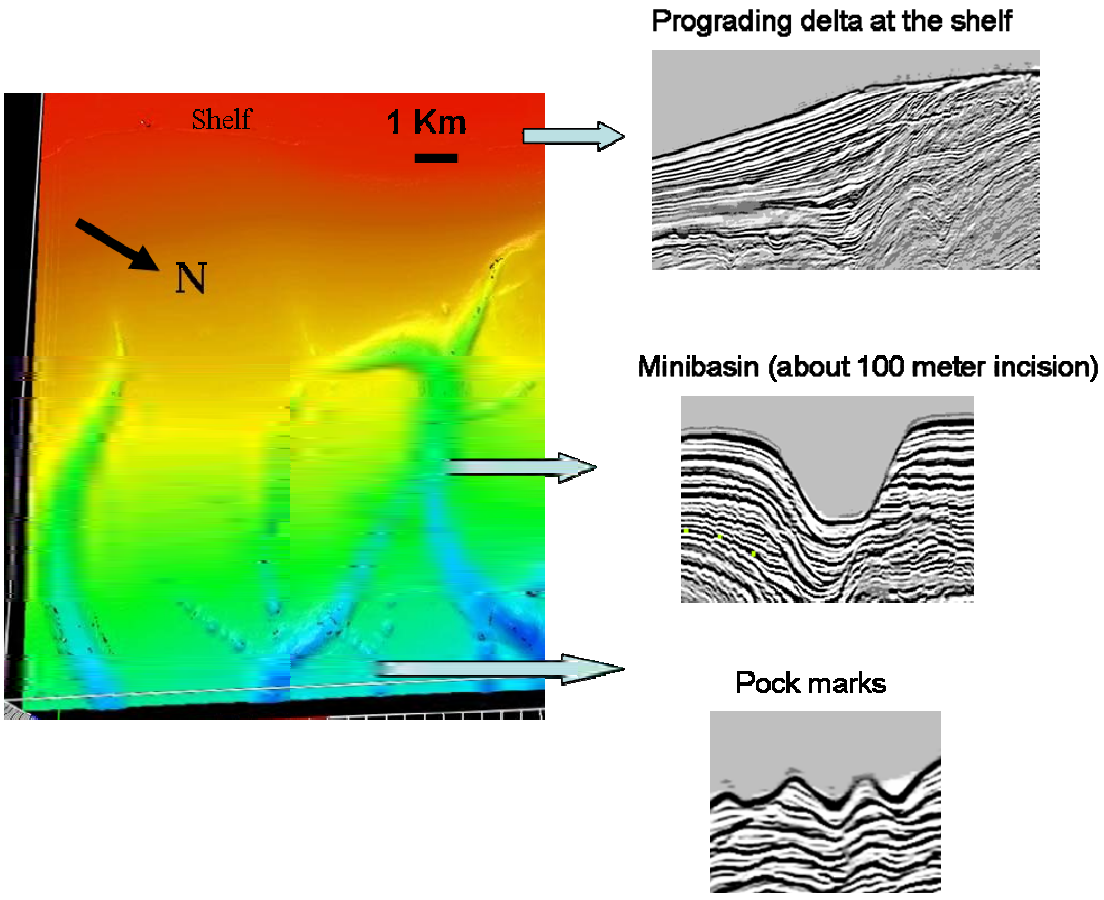

Figure 5.2: Seismic stratigraphic interpretation. Present-day seabed map, interpreted from 3D seismic data. Prograding deltas form on the continental shelf, and minibasins form on the continental slope. Note the geometry of a minibasin on vertical seismic section. The sediments deposited by turbidite channel within such a minibasin constitute exploration targets for potential reservoirs.

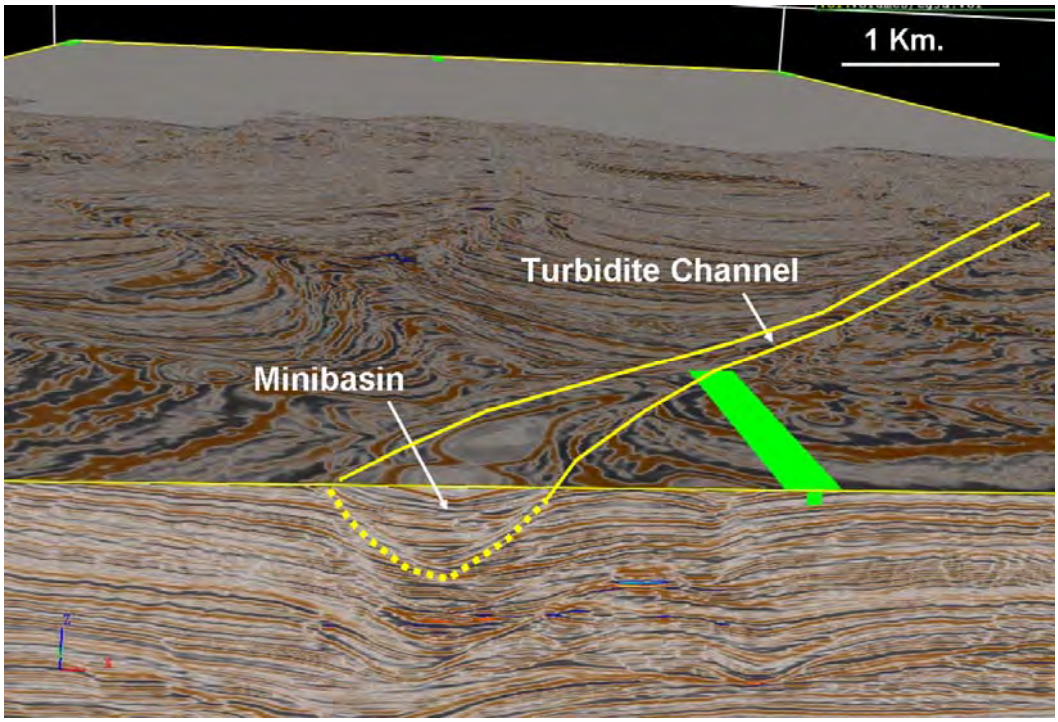

Figure 5.3: Seismic stratigraphic interpretation. The composite seismic section shows the minibasin topography along with a turbidite channel.

We select two wells from proximal to distal locations of a channelized turbidite sequence. The spatial locations of these wells are shown on an amplitude map in Figure 5.4. Well-B is the proximal well, and well-A is the distal well. Well-X is located away from the channel complex, and therefore not included in the present study. The amplitude map represents the maximum amplitudes extracted along an interpreted horizon (Top of uncemented, oil sand) over a search window of 8 ms. We can interpret this amplitude map to identify the spatial differences in channel confinement. For example, the channel is more confined at the proximal location, and it becomes relatively unconfined at the distal location.

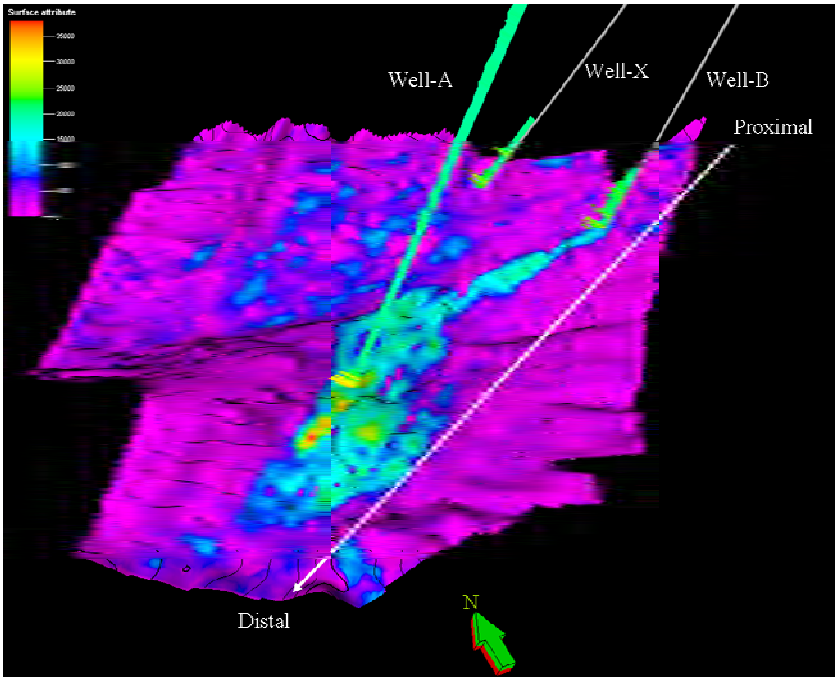

Figure 5.4: Amplitude map showing well locations in channelized turbidite deposits from the proximal to the distal location. The amplitudes were extracted along an interpreted horizon (Top of uncemented, oil sand) from full-stack seismic volume. Well-A is the distal well, and well-B is the proximal well. The white arrow represents the flow direction.

The log data from these wells show fining upward patterns, which is typical for a channelized turbidite sequence (Labourdette, 2007), indicating decrease in depositional energy vertically upward. An example of a fining upward sequence from well-A is shown in Figure 5.5. The fining upward sequence in the other well is from a similar depth interval (Figure 5.5). In both the wells, we observe a blocky sequence immediately below the fining upward sequence. The core descriptions confirm that the fining upward sequence is associated with uncemented lithofacies, and the blocky sequence is associated with carbonate cemented sandstones. In this chapter, we focus on spatial variations of sand/shale ratios and sorting of these fining upward, uncemented sandstones. The seismic response of blocky, carbonate cemented sandstones is discussed in Chapter 6.

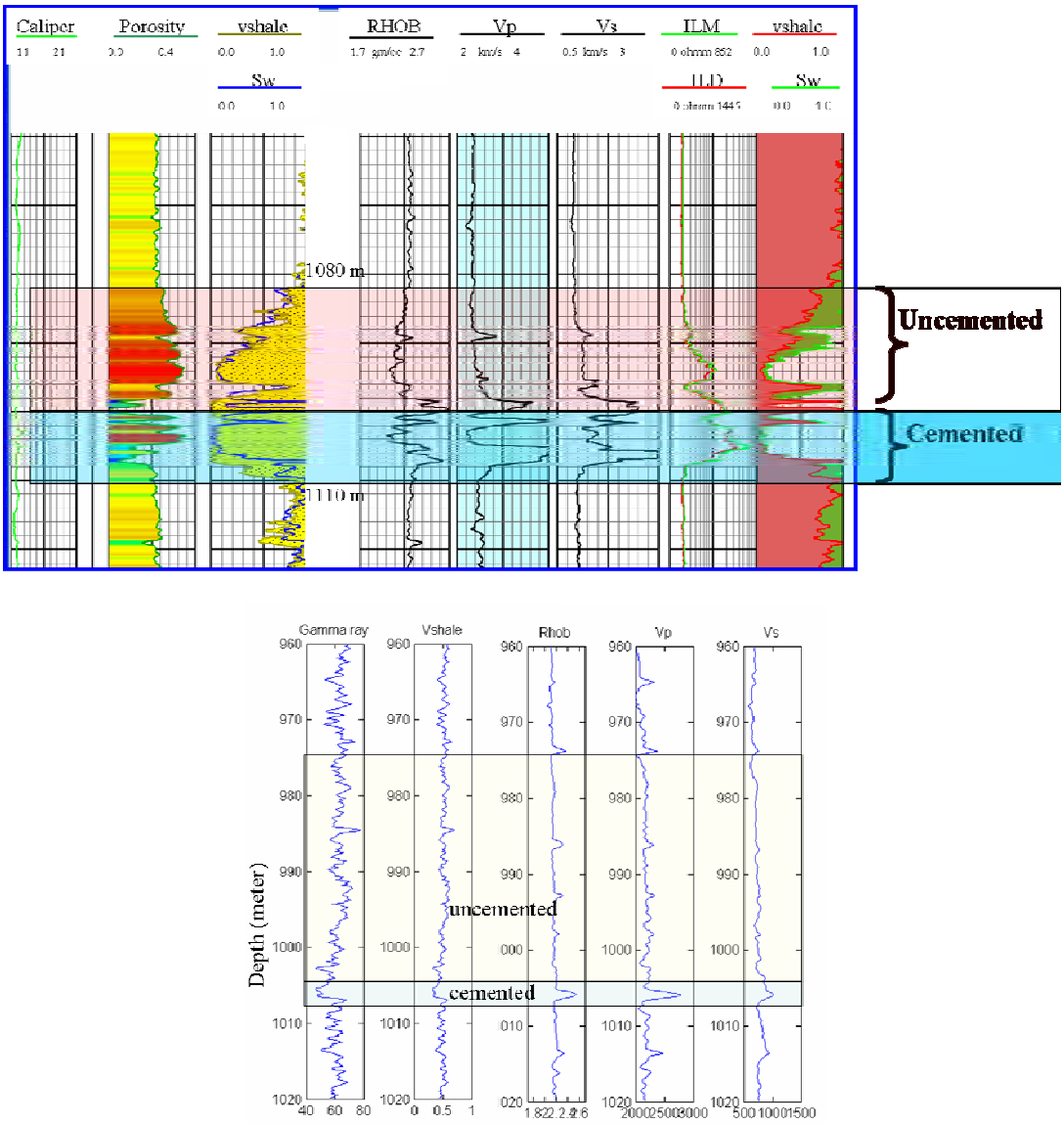

Figure 5.5: Well logs from well-A (top) and well-B (bottom) showing examples of fining-upward shaly sand sequence. The core descriptions confirm that the fining upward sequence is associated with uncemented lithofacies, and the underlying blocky sequence is associated with carbonate cemented sandstone.

It is important to recognize that the well log patterns alone cannot confirm the depositional environment (Emery and Myers, 1996). Fining upward patterns on well logs suggest multiple possible environments. For example, tidal channels, fluvial point bars, and turbidite channels all show characteristic fining upward patterns on well logs. In our study area, the fining upward patterns on well logs (Figure 5.5) along with the incision

geometry from seismic data (Figure 5.2 and Figure 5.3) suggest that the sediments were deposited in channelized settings. Core descriptions from the same study interval (Lowe, 2004) confirm that these fining upward and channelized sequences were deposited by high-density turbidity currents in submarine canyons.

Six lithofacies are recognized in the study area based on detailed core observations by Lowe (2004). The digital core images of different lithofacies are shown in Figure 5.6. The sediment characteristics and depositional settings of these facies are summarized in Table 5.1. The lithofacies in the present study correspond to the standard lithofacies in most deep-water studies with the exception that lithofacies 4 is diagenetic (carbonate-cemented sandstones) in all of the cores. The seismic signatures of lithofacies 4 are discussed in Chapter 6.

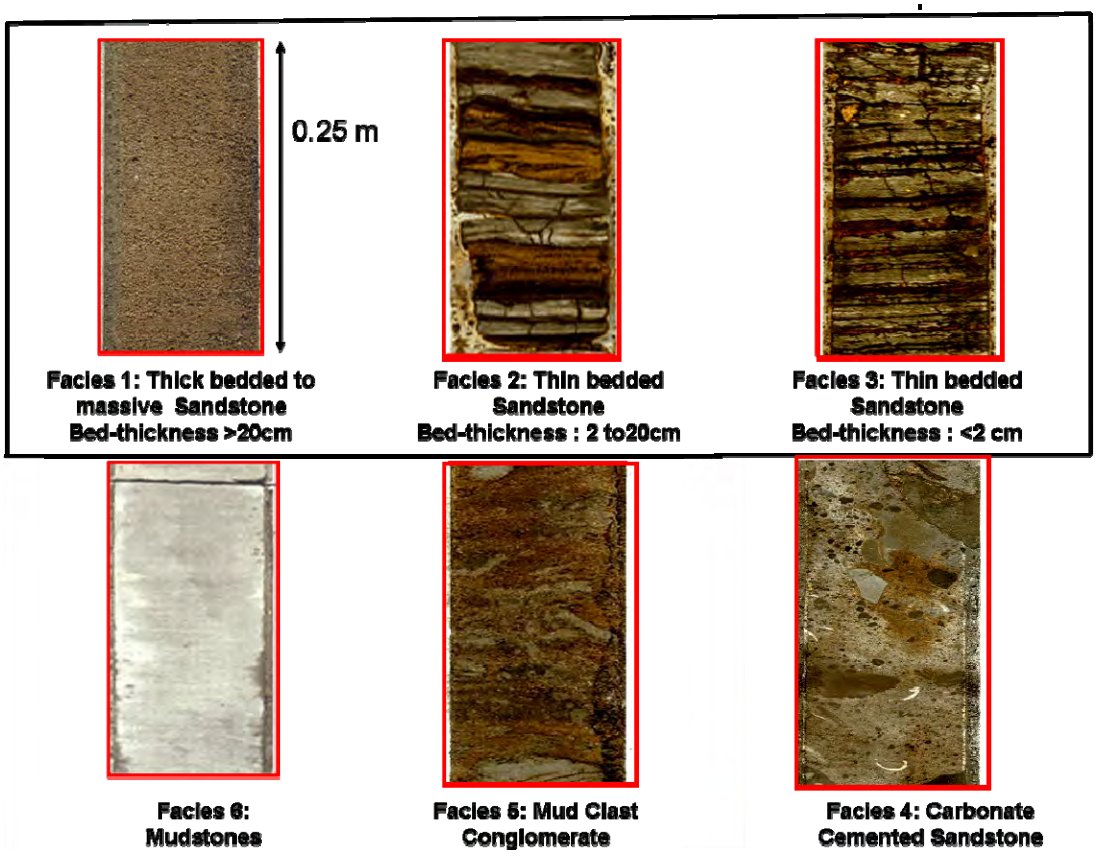

Figure 5.6: Six different lithofacies identified using digital core images from study area. Lithofacies 4, carbonate cemented sandstone, is diagenetic. The rest of the facies are depositional in origin.

The basic architecture of the lithofacies includes fining upward units of conglomerate (lithofacies 5) and coarse-grained, thick-bedded sandstone (lithofacies 1) inter-layered with large slump, slide blocks and debris flows. The slump and slide blocks are usually well developed at the base of coarse grained sections. These coarse grained sandstones (lithofacies 1) tend to grade upward into fine grained and thin bedded facies (lithofacies 2), and then to even finer grained and thinner bedded facies (lithofacies 3), and next to mudstone (lithofacies 6). Lithofacies 2, 3 and 6 show various intensity of bioturbation. In some cases, more than one cycle is present, suggesting either stacked smaller channel-fill units, or finer grained intervals between coarser grained units signifying slide or slump blocks.

The lithofacies succession within a fining upward sequence (Lithofacies 1, 2 and 3), show laminations on the cores. In the next section, we perform petrophysical analysis of these laminated facies succession to show variation in sand/shale ratios and porosity, and their effects on velocity and P-impedance.

Table 5.1: The lithofacies used in the present study. The sediments characteristics and depositional settings are summarized from the study by Lowe (2004).

Sediment characteristics and depositional setting of six lithofacies		
Lithofacies	Sediment characteristics	Depositional settings
Lithofacies-1: Thick-bedded to massive sandstone	Beds>20 cm thick	Coarse-sediment, high-density flow dominated systems including confined channels, slope gullies, proximal channel mouth/lobe (sheet sands), crevasse, proximal splay and interchannel avulsion units, high amplitude reflection packages (HARP)
Lithofacies-2: Interbedded, thin-bedded sandstone and mudstone	Beds 2-20 cm thick, >20% sandstone	Near channel levees and out-of-channel deposits, medial channel mouth/lobe accumulations, medial splay, HARP, and early channel abandonment
Lithofacies-3: Interbedded, thin-bedded sandstone and mudstone	Beds <2cm thick, usually <20% sandstone	Medial to distal levees and out-of-channel areas, distal lobes, distal splays, HARP, late channel abandonment, and basin plain
Lithofacies-4: Carbonate-cemented sandstone	Diagenetic	This is a diagenetic, not depositional lithofacies
Lithofacies-5: Conglomerate and breccia	30-60% mudstone clasts suspended within coarse to very coarse grained sandstone	Conglomerate composed of clasts coarser than small pebbles (2-3 cm in diameter), and virtually always confined to channels or crevasse units. Mudstone clasts can also be transported somewhat further downslope, beyond the channel mouth
Lithofacies-6: Mudstone	<10% sandstone interbeds	Interchannel or system abandonment muds (largely undisturbed). Mudstone deposited by mass movement is common in slope and base-of-slope settings, including slope channels, gullies and submarine canyons

5.5 Petrophysical analysis of well logs

In this section, we perform petrophysical evaluation of well logs using the Thomas-Stieber model (Thomas and Stieber, 1975). This particular model is useful to estimate net-to-gross (sand/shale ratios) and sand porosity in shaly sand sequences for different shale configurations, where the bed thickness is below well log resolution (Pedersen and Nordahl, 1999). In the Thomas-Stieber model, gamma ray response is modeled as a function of sand and shale porosity. The graphical solutions for net-to-gross and sand porosity are shown in Figure 5.7 for two different shale configurations: laminated shaly sand (Trend A) and dispersed shaly sand (Trend B).

It is important to note that the terminologies laminated and dispersed shale sands, which are familiar to a petrophysicist and a rock-physicist, are not commonly used in the Sedimentology literature (personal communication with Steve Graham). Please refer to the Table 1.1 in Chapter 1 for translating these terminologies to a sedimentologist.

In Figure 5.7, we assume that the porosity in the clean sand end member is 0.4, and the porosity in the shale end member is 0.2. The overlay of log data from well-A shows that the log data follow the trend predicted by the laminated shaly sand model. The net-to-gross gradually decreases from 1 to zero as shale laminations are progressively added to clean sandstones. Our results are consistent with a previous study by Florez (2005), who showed that shaly sand sequences from a deep-water environment in West Africa are laminated. The laminated nature of shaly sands in our study area along with the presence of thin beds is also confirmed by the digital core images. It is important to recognize the thin-bedded scenario and to choose an appropriate interpretation method based on shale configurations; otherwise the reservoir potential may be significantly misrepresented.

The laminated and dispersed shaly sand sequences show distinct signatures on the velocity-porosity crossplot. The velocity-porosity trends can be predicted from the Backus averages for the laminated scenario (Backus, 1962), and from the Marion-Yin model for the dispersed scenario (Marion et al., 1992). According to the Marion-Yin

model, when clay volume fraction is less than sand porosity, clay particles are assumed to be dispersed in the pore space of the load-bearing sand, and velocity increases with increasing clay content. In contrast, when clay volume fraction is greater than sand porosity, sand grains become suspended in the clay-rich matrix, and velocity decreases with increasing clay content.

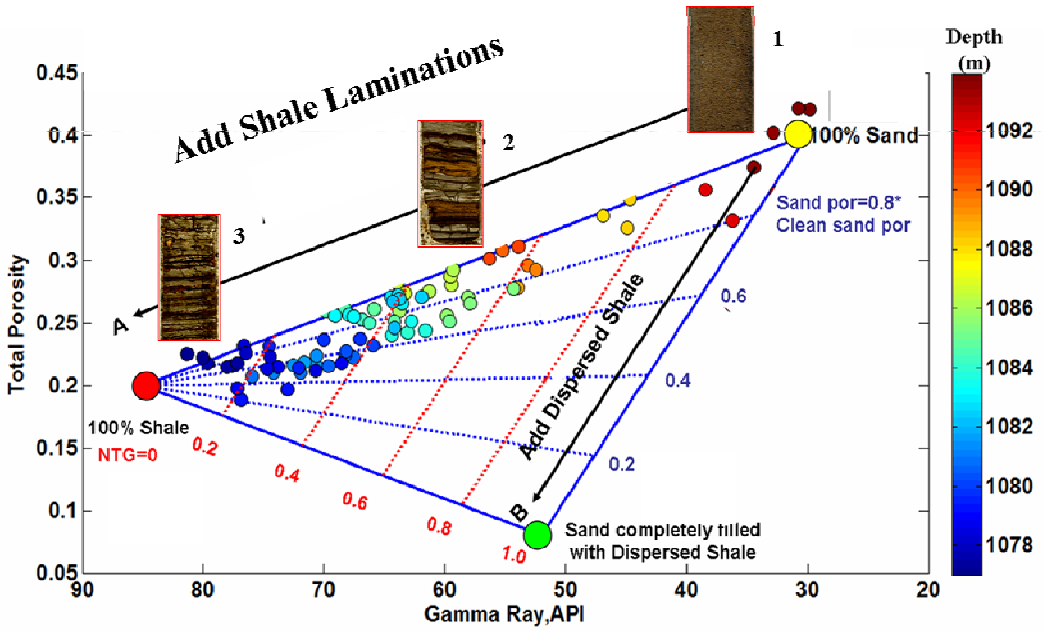

Figure 5.7: Total porosity vs. gamma ray using Thomas-Stieber model. The three end members represent 100% clean sand, 100% shale, and sand completely filled with dispersed shale. The graphical solutions for net-to-gross (NTG) and sand porosity (sand por) are shown for two different shale configurations: laminated shaly sand (Trend A) and dispersed shaly sand (Trend B). The texts in red indicate NTG values, and the texts in blue indicate sand porosity as a fraction of clean sand porosity. The log data is color-coded by depth, and represents a single fining-upward, shaly sand interval. The log data closely follow the trend predicted by the laminated shaly sand model.

In the present study, the velocity from the shaly sand sequence increases with increasing porosity, and the velocity-porosity trend closely follows the trend predicted by the laminar model, as shown in Figure 5.8. In this figure, the velocities represent those of 100% brine saturated rock, computed using the fluid substitution recipe by Katahara (2004) for laminated shaly sands. According to Katahara's fluid substation recipe, we perform fluid substitution only at the clean sand end member using the isotropic

Gassmann equations (Gassmann, 1951), and then linearly interpolate the other data points in the density-compressibility domain.

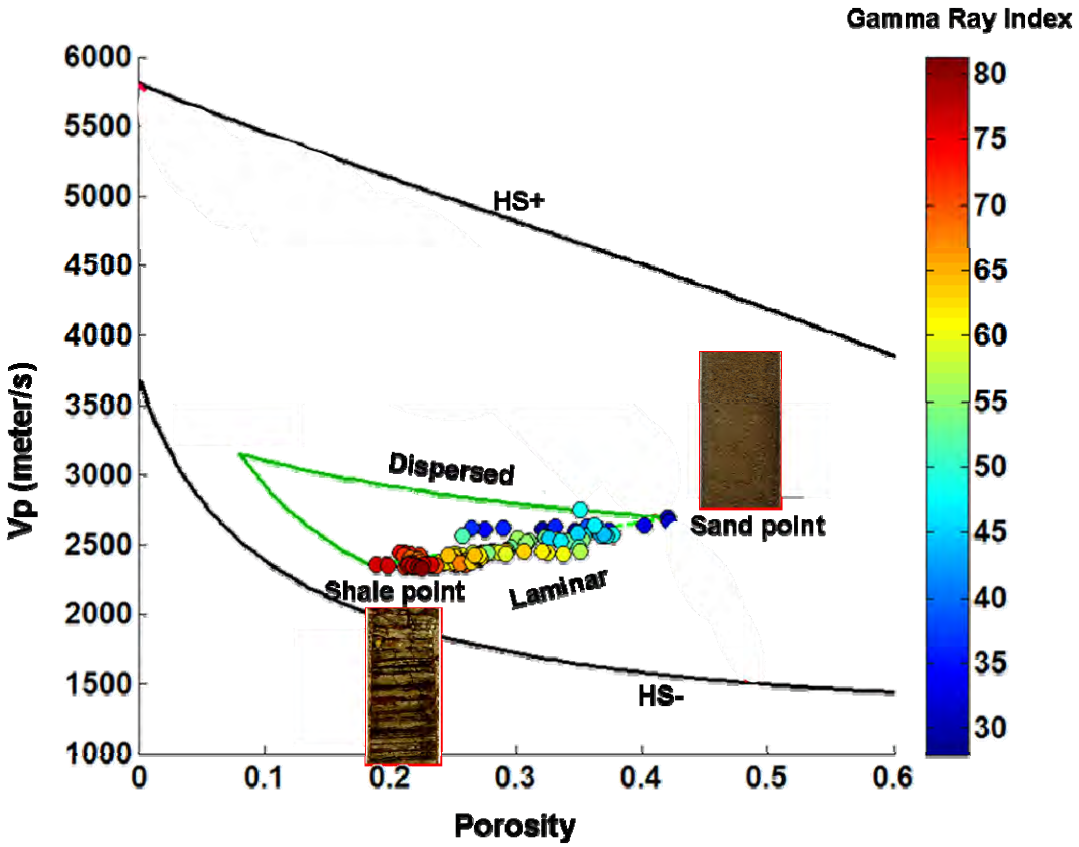

Figure 5.8: The trend of the laminated shaly sand sequence on the V_P-porosity crossplot. HS represents the Hashin-Shtrikman bounds for a mixture of quartz and water. HS+ is the upper bound and HS- is the lower bound. The data is color-coded by gamma-ray index, and represents a single fining-upward, shaly sand sequence. The data follow the trends predicted by the laminated shaly sand model. The porosity and velocity are progressively lowered as shale laminations are added to the sand end member.

The signatures of different lithofacies from this laminated shaly sand sequence on the P-impedance vs. porosity crossplot are presented in Figure 5.9. We observe that the P-impedance vs. porosity trend is very flat. The P-impedance changes only slightly for a huge change in porosity from 0.2 to 0.4. The porosity and P-impedance progressively decrease from the facies deposited in the confined channel (lithofacies 1), to the facies deposited in the near-channel levee (lithofacies 2), and then to the facies deposited in the

medial-distal levee (lithofacies 3). This plot illustrates a link between genetic facies succession in a channelized turbidite sequence with the P-impedance-porosity trend. The core descriptions show that sand/shale ratio and sorting vertically decreases within this fining upward sequence. In order to quantify the link between these depositional lithofacies succession with the P-impedance-porosity trend, we need to calibrate a suitable rock physics model with well data.

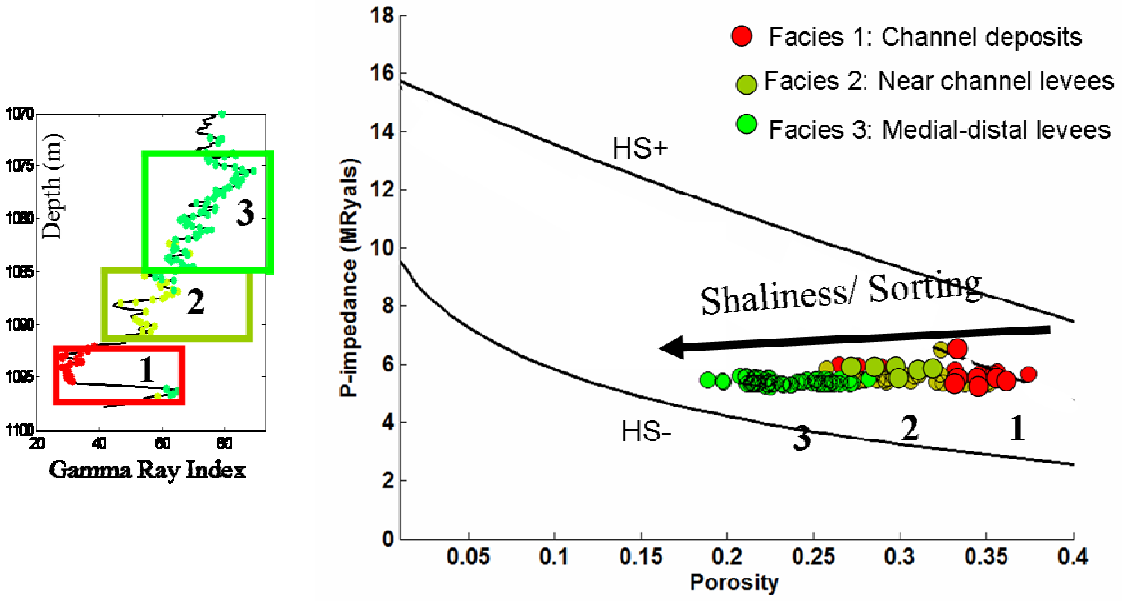

Figure 5.9: The signature of a fining upward, laminated shaly sand sequence on the P-impedance vs. porosity crossplot. Left: gamma ray log showing the facies succession. Right: P-impedance vs. porosity colorcoded by different lithofacies as identified from core descriptions. HS represents the Hashin-Shtrikman bounds for a mixture of quartz and water. HS+ is the upper bound and HS- is the lower bound. The P-impedance changes only slightly for a huge change in porosity from 0.2 to 0.4.

5.6 Calibration of rock physics models at the wells

In this section, we calibrate a suitable rock physics model for the uncemented, shaly sand sequence with the well data. We test the predictions of two different effective medium models against well data: the soft-sand model (Dvorkin and Nur, 1996) and the modified soft-sand model (discussed later in this section).

In the soft-sand model, the effective moduli at the well-sorted, high-porosity end

member (~40% for sandstones) are computed using the Hertz-Mindlin contact theory (Mindlin, 1949; Mavko et al., 1998). The Hertz-Mindlin contact theory provides the following expressions for the bulk (K_{HM}) and the shear (G_{HM}) moduli of a dense random pack of identical spherical grains, subjected to an effective pressure P (Mavko et al., 1998):

$$K_{HM} = \left[\frac{C^2(1-\phi_0)^2 G^2}{18\pi^2(1-\nu)^2} P\right]^{1/3} \tag{5.1}$$

$$G_{HM} = \frac{5-4\nu}{5(2-\nu)}\left[\frac{3C^2(1-\phi_0)^2 G^2}{2\pi^2(1-\nu)^2} P\right]^{1/3} \tag{5.2}$$

where ϕ_0 is the critical porosity (~40 % in sandstones), C is the coordination number (average number of grain contacts), and G and ν are the mineral shear modulus and Poisson's ratio. The elastic moduli at the zero-porosity end member are given by mineral moduli. In the soft-sand model, the effective elastic moduli of sand with porosities between zero and critical porosity are interpolated using the lower Hashin-Shtrikman bound (Mavko et al., 1998). The heuristic argument for this interpolation is that adding small grains in the pore space is the elastically softest way to add mineral. The lower bound, which is an iso-stress model for suspensions, is always the elastically softest way to mix multiple mineral phases. The soft-sand model is also referred as the friable sand model in literature, and has been demonstrated to capture the sorting trend of uncemented lithofacies (e.g., Gutiérrez et al., 2002; Avseth et al., 2005; Florez, 2005). Although the soft-sand model reasonably predicts the P-wave velocity in uncemented sands, this model overpredicts the S-wave velocity as shown by several studies (e.g., Goddard, 1990; Zimmer, 2003; Makse et al., 2004), due to the overprediction of shear modulus at critical porosity by the Hertz-Mindlin model.

In order to overcome the problem with shear wave prediction in the soft-sand model, usually the effective shear modulus at the critical porosity is divided by a correction factor (Avseth et al., 2006). This shear modulus correction factor is computed on a trial-

and-error basis, and is usually 2 in most of the uncemented sands (personal communication with Per avseth). In the modified soft-sand model, no shear modulus correction factor is necessary. This particular model computes effective elastic properties at the critical-porosity using the extended Walton model (Walton, 1987; Jenkins et al., 2005) coupled with empirical coordination number, pressure, and porosity relations (equations 5.5- 5.8; for details see Chapter 3). The extended Walton model represents a mixture of completely rough and smooth grains. The effective moduli of sand with porosities ranging between zero to the critical porosity (~40%) are computed using the same principle as in the soft-sand model, i.e., the moduli are interpolated using the lower Hashin-Shtrikman bound.

The Walton model (Walton, 1987) provides effective elastic moduli for two special cases: infinitely rough spheres (friction coefficient is very large) and ideally smooth spheres (friction coefficient is zero). Jenkins et al. (2005) combined the Walton's rough and smooth models to express the effective elastic moduli as follows:

$$\lambda_{eff}^{w} = \frac{C(1-\phi)}{5\pi}\frac{G}{(1-\nu)}\left[\frac{3\pi}{2}\frac{(1-\nu)}{(1-\phi)C}\frac{P}{G}\right]^{1/3}\frac{[2-\nu-2\alpha(1-\nu)]}{(2-\nu)} \tag{5.3}$$

$$G_{eff}^{w} = \frac{C(1-\phi)}{5\pi}\frac{G}{(1-\nu)}\left[\frac{3\pi}{2}\frac{(1-\nu)}{(1-\phi)C}\frac{P}{G}\right]^{1/3}\frac{[2-\nu+3\alpha(1-\nu)]}{(2-\nu)} \tag{5.4}$$

where ϕ is the porosity. Since the effective shear modulus (G_{eff}) of a granular aggregate is linearly proportional to tangential stiffness (see Chapter 3), it is possible to lower G_{eff} by assuming tangential stiffness is zero for some fraction of the grains. We use equations 5.3 and 5.4 to represent this scenario, where α represents the fraction of completely adhered contacts, and (1-α) represents the fraction of completely slipping contacts. We refer to this as the extended Walton model. When α is zero, we obtain the Walton smooth model, where all the grains have zero friction at their contacts. And, when α is equal to 1, we obtain the Walton rough model, which considers infinitely high friction at the grain contacts of identical spheres.

We use the extended Walton model with α = 0.6 to invert the coordination number (C) from measurements on dry, unconsolidated sandstones by Zimmer (2003). We choose this particular value of α because it provides realistic prediction of C for a random pack of grains. The relations between C-porosity and C-pressure are expressed as:

$$C_P(\phi) = (-2.338\text{e}-014)\phi^{9.099} + 14.45 \tag{5.5}$$

$$C_S(\phi) = (-1.798\text{e}-014)\phi^{9.099} + 11.02 \tag{5.6}$$

$$C_P(P) = (777.1)P^{0.001545} - 770.7 \tag{5.7}$$

$$C_S(P) = (-4.457)P^{-0.2724} + 9.401 \tag{5.8}$$

where C_P and C_S represent coordination numbers to predict V_P and V_S respectively. The porosity ϕ is in percentage, and P is the effective pressure in MPa. The velocity predictions using the soft-sand model and the modified soft-sand model in clean sands are compared in Figure 5.10. The V_P predictions are similar in both the models. The modified soft-sand model predicts lower V_S than the original soft-sand model. The V_S prediction by the modified soft-sand model is similar to the soft-sand model with a shear modulus correction factor of 2.

We apply the modified soft-sand model to represent the trend for sand/shale ratio by varying the quartz/clay ratio from zero to 1 for computing the effective elastic properties of the mineral aggregates. The density is computed using the arithmetic average and the bulk and shear moduli are computed using the Voigt-Reuss-Hill average (Hill, 1952). The mineral properties for quartz are bulk modulus= 36 GPa, shear modulus=45 GPa, and density=2.65 gm/cc. The mineral properties for clay are bulk modulus= 21 GPa, shear modulus=7 GPa, and density=2.58 gm/cc.

We apply the same modified soft-sand model to represent the trend for textural maturity, where porosity changes along a constant value of quartz/clay ratio. Several studies have heuristically found that interpolation using the lower Hashin-Shtrikman bound corresponds to sorting trend in unconsolidated sediments (e.g., Dvorkin et al., 1996; Avseth 2000; Florez 2005). The lower Hashin-Shtrikman bound is theoretically the

lowest elastic stiffness possible for a mix of multiple phases.

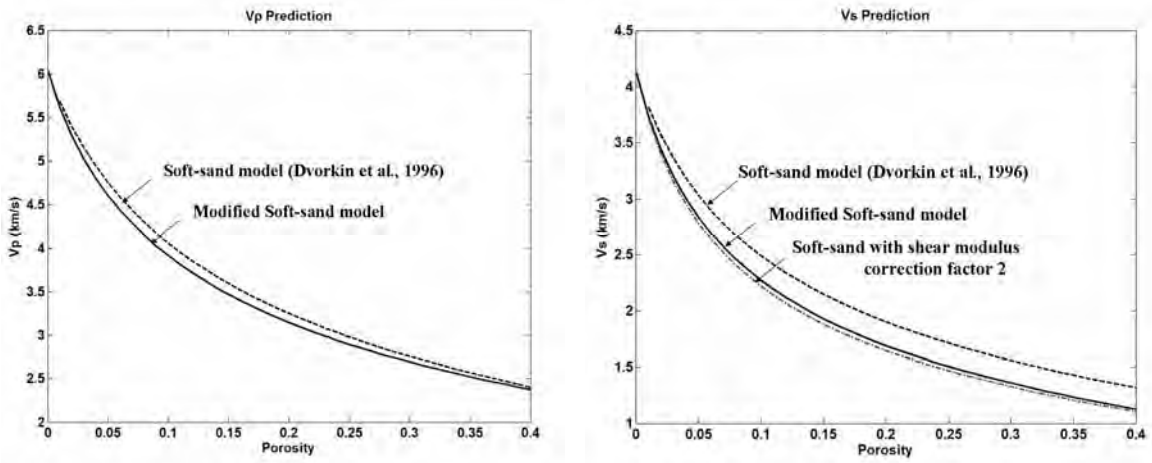

Figure 5.10: Comparisons of the velocity predictions by the soft-sand model and the modified soft-sand model. Left: V_P predictions, Right: V_S predictions. The V_P predictions are similar in both the models. The modified soft-sand model predicts lower V_S than the original soft-sand model. The V_S prediction by the modified soft-sand model is similar to the soft-sand model with a shear modulus correction factor of 2.

The P-impedance predicted by the modified soft-sand model for different quartz/clay ratios at different porosities are shown in Figure 5.11. In this plot, we also overlay the log data colorcoded by three different lithofacies. The sand/shale ratios successively decreases from channel sandstones (lithofacies 1), to the sandstones deposited in the proximal levee (lithofacies 2), and then to the sandstones deposited in the medial to distal levee (lithofacies 3). The original well log velocities and densities are transformed to represent those of 100% brine saturations using the fluid substitution recipe by Katahara (2004). The saturated P-impedance from the log data transect the clay contours ranging from 0 to 100 % clay content, and the transition from the sand-rich to the shale-rich facies shows a slight decrease in P-impedance for a large decrease in porosity from ~40% to ~20%.

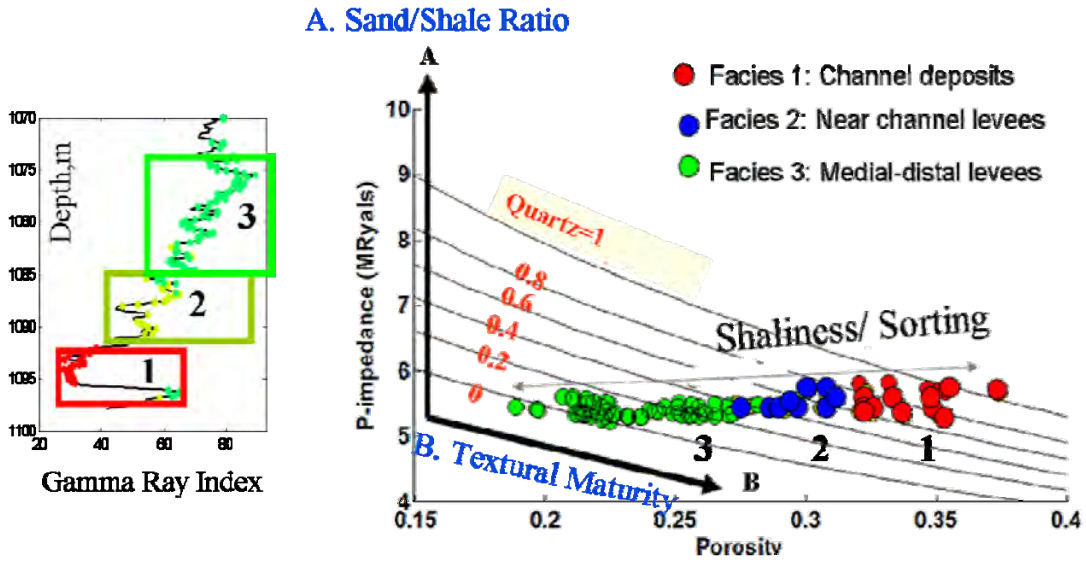

Figure 5.11: Left: gamma ray log showing the trend of shaliness for three different lithofacies. Right: P-impedance (Ip) vs. total porosity trends, color-coded by same three lithofacies deposited in a fining upward sequence. The grey lines represent P-impedance predicted by the modified soft-sand model for different quartz/clay ratios at different porosities. The values of quartz/clay ratio are shown in red. Trend A represents increasing sand/shale ratio, and Trend B represents improving textural maturity. Note that the saturated P-impedances transect the clay contours.

One important observation from Figure 5.11 is that sand/shale ratio and textural maturity have competing effects on P-impedance: increasing with sand/shale ratio and decreasing with textural maturity (sorting). In our study area, the sandstones which are texturally more mature also have a higher sand/shale ratio (lithofacies 1). As a result, we observe a slightly higher P-impedance in the sand-rich facies deposited within a channel (lithofacies 1) than the shale-rich facies deposited in the levee (lithofacies 2 and 3).

The rock physics models calibrated at these wells can be used to predict the sedimentological parameters, such as sand/shale ratios and sorting from seismic attributes. The next section will quantify the spatial variation of these sedimentological parameters by combining the modified soft-sand model and the spill-and-fill sequence stratigraphic model.

5.7 Quantify spatial trend of sedimentological parameters in sand-rich facies

We combine the spatial trends of sand/shale ratio and sorting as predicted by the spill-and-fill sequence stratigraphic model, and the P-impedance calibrated at the well locations to quantify the spatial trends of these sedimentological parameters away from the well locations. Specifically, we select lithofacies 1, which is the facies with the best reservoir quality, deposited in high-density turbidite-flow-dominated systems, including confined channels, slope gullies, and the proximal channel mouth. This facies is easily identifiable in well logs, since it is deposited at the base of a fining upward, turbidite channel.

The spatial trend of P-impedance vs. porosity in lithofacies 1 is shown Figure 5.12, along with the P-impedance predicted by the modified soft-sand model for different quartz/clay ratios at different porosities. For the purpose of comparing with real seismic signatures, we have plotted the log data with original fluid saturation. We observe that the same facies at the distal location has higher porosity and P-impedance than those at the proximal location. For example, the porosities are 0.30-0.35 at the proximal location, and 0.35-0.40 at the distal location. The P-impedances at the proximal and the distal locations follow the quartz/clay contour of 0.4 and 1, respectively. This plot can act as a template to interpret P-impedance in terms of porosity and sand/shale ratio.

According to the heuristic assumption in the modified soft-sand model, the downdip increase in porosity corresponds to an increase in textural maturity, e.g., sorting. The downdip increase in sorting can be explained by the spill-and-fill sequence stratigraphic model, which suggests that sorting improves along the transportation direction of sediments due to deflocculation processes by the turbidity current (e.g., Piper, 1978; Brunt et al., 2004; Lerch et al., 2006).

The modified soft-sand model also predicts that the downdip increase in P-impedance corresponds to an increase in sand/shale ratio. The downdip increase in sand/shale ratio can be explained by the spill-and-fill model, which suggests that progressively coarser

sand fractions (higher quartz content) spill from updip minibasin and fill into downdip minibasin.

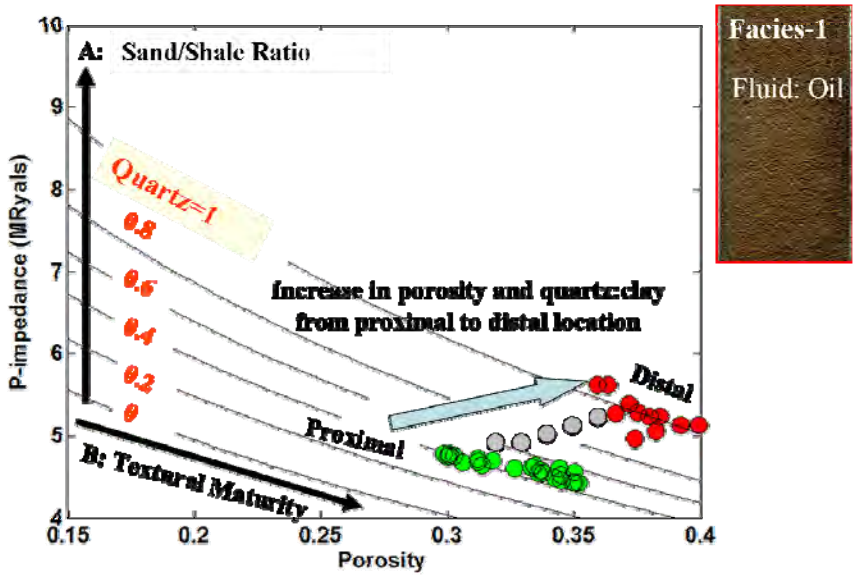

Figure 5.12: Spatial trend of sorting and quartz/clay ratios in sand-rich facies deposited at the base of the fining upward, channelized turbidite sequence (potential reservoir facies). The texts in red indicate the values for quartz/clay ratio in the modified soft-sand model. Trend A represents increasing sand/shale ratio, and Trend B represents improving textural maturity. Sorting and quartz/clay ratio increases from the proximal to distal locations giving rise to higher porosity and P-impedance.

We apply the template shown in Figure 5.12 for interpreting P-impedances in terms of sedimentological parameters away from the well locations. The P-impedances are obtained by inverting post-stack 3D seismic data using model-based inversion method in the Humpson Russel software. To build the initial model, we used three wells (shown in Figure 5.4) and four interpreted horizons. The map of inverted P-impedance extracted along the top of uncemented, oil sand is shown in Figure 5.13.

We use the template shown in Figure 5.12 in order to transform the map of inverted P-impedance to the map of porosity and sand/shale ratio (Figure 5.14). In this computation, porosity at the proximal well = 30%, porosity at the distal well = 40%, sand/shale ratio at the proximal well = 0.4, and sand/shale ratio at the distal well = 1. Since, the functional forms of spatial increase in porosity and sand/shale ratio from the proximal to the distal well is unknown, we assume them to be linear (grey circles in Figure 5.12).

Our modeling predicts a higher value of porosity (~40%) and sand/shale ratio (~1) in further distal locations within the confinement of channel, which may indicate future resource potential (Figure 5.14). It is important to note that this map of porosity or sand/shale ratio represents a single, possible realization. There is uncertainty due to data and our modeling assumptions. One can extend our deterministic approach, and include uncertainty to generate multiple realizations of porosity and sand/shale ratio maps.

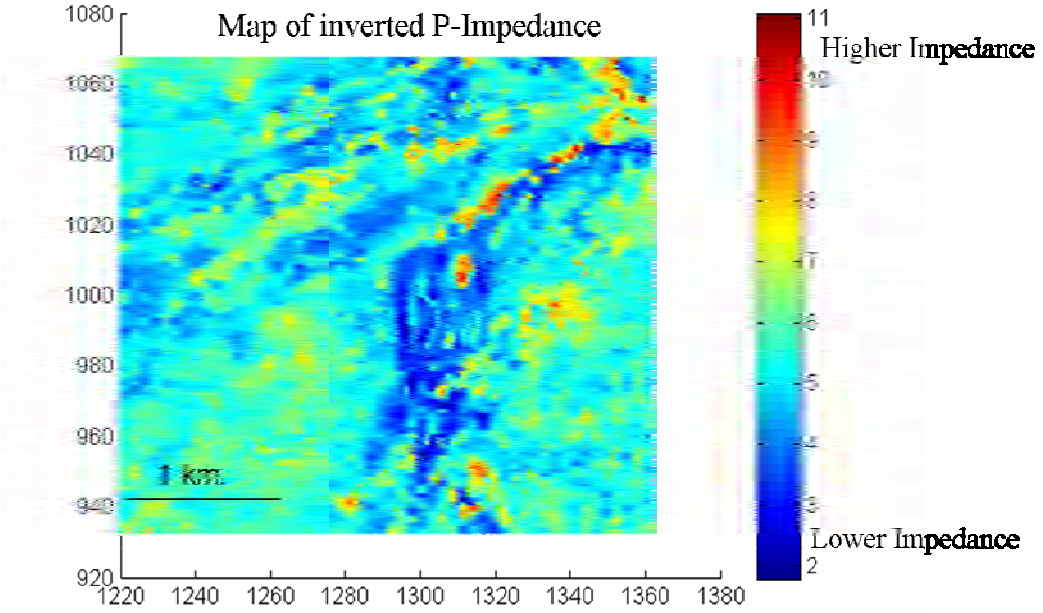

Figure 5.13: Map of inverted P-impedance along the interpreted horizon corresponding to the reflection from shale to uncemented, oil sand.

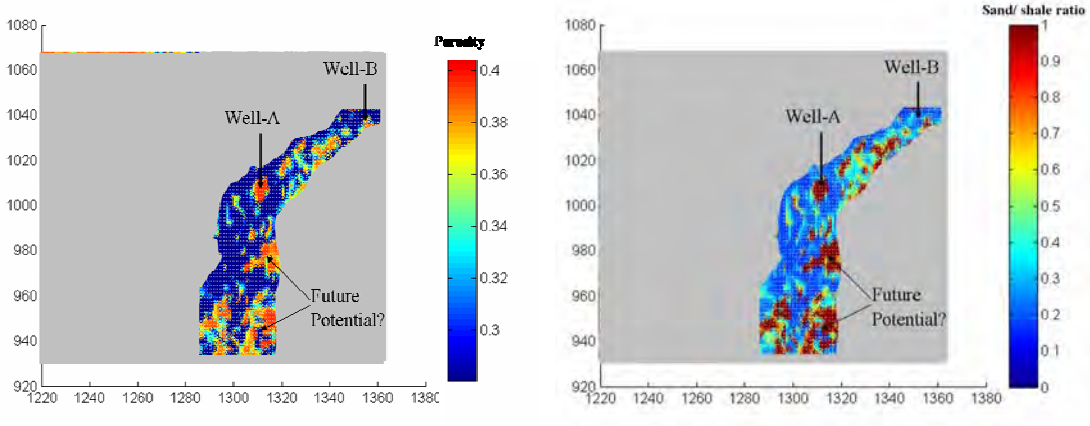

Figure 5.14: Map of porosity (left) and map of sand/shale ratio (right), computed from inverted P-impedance using the template shown in Figure 5.12.

5.8 AVO analysis combining sequence stratigraphy and rock physics model

5.8.1 AVO modeling at the proximal and the distal wells

The spatial changes in sand/shale ratio and sorting within the sand-rich facies (lithofacies 1) affect the AVO response. We compute the effective elastic properties using the modified soft-sand model, followed by Monte-Carlo simulations. Monte Carlo simulations account for a distribution of plausible values instead of single average values, and therefore help to avoid the flaw of averages (Mukerji et al., 2001). The input sedimentological parameters, such as quartz/clay ratio, are constrained by the calibrated rock physics model parameters at the wells. For example, the quartz/clay ratio is 0.4 at the proximal location, and 1 at the distal location. The fluid properties are assumed to be constant spatially (Sw=0.2, So=0.8, fluid bulk modulus=1.17 GPa, and fluid density=0.82 gm/cc). The velocities and densities in the overburden shale interval are obtained from the well logs. The AVO responses, e.g., P-to-P reflection coefficient (R_{PP}), intercept, and gradient are computed using isotropic Zoeppritz equation simplified by Aki-Richards (1979). Our modeling suggests distinct AVO responses in the proximal vs. the distal location (Figure 5.15). The modeling shows class IV response at both the locations, where the intercepts are negative and the gradients are positive. The magnitude of R_{PP} decreases with increasing offsets. However, the intercept is more negative and the gradient is more positive at the distal location.

The modeled AVO responses are validated with real seismic data at the well locations (Figure 5.16). We follow the reflection event from shale to uncemented, oil sand in three partial stack volumes (near offset stack: 0-18 degree, mid offset stack: 18-35 degree, and far offset stack: 35-45 degree). We observe class IV response, where reflection amplitude is negative and decreases its magnitude at the far offset. The magnitudes of reflection amplitudes are higher at the distal location.

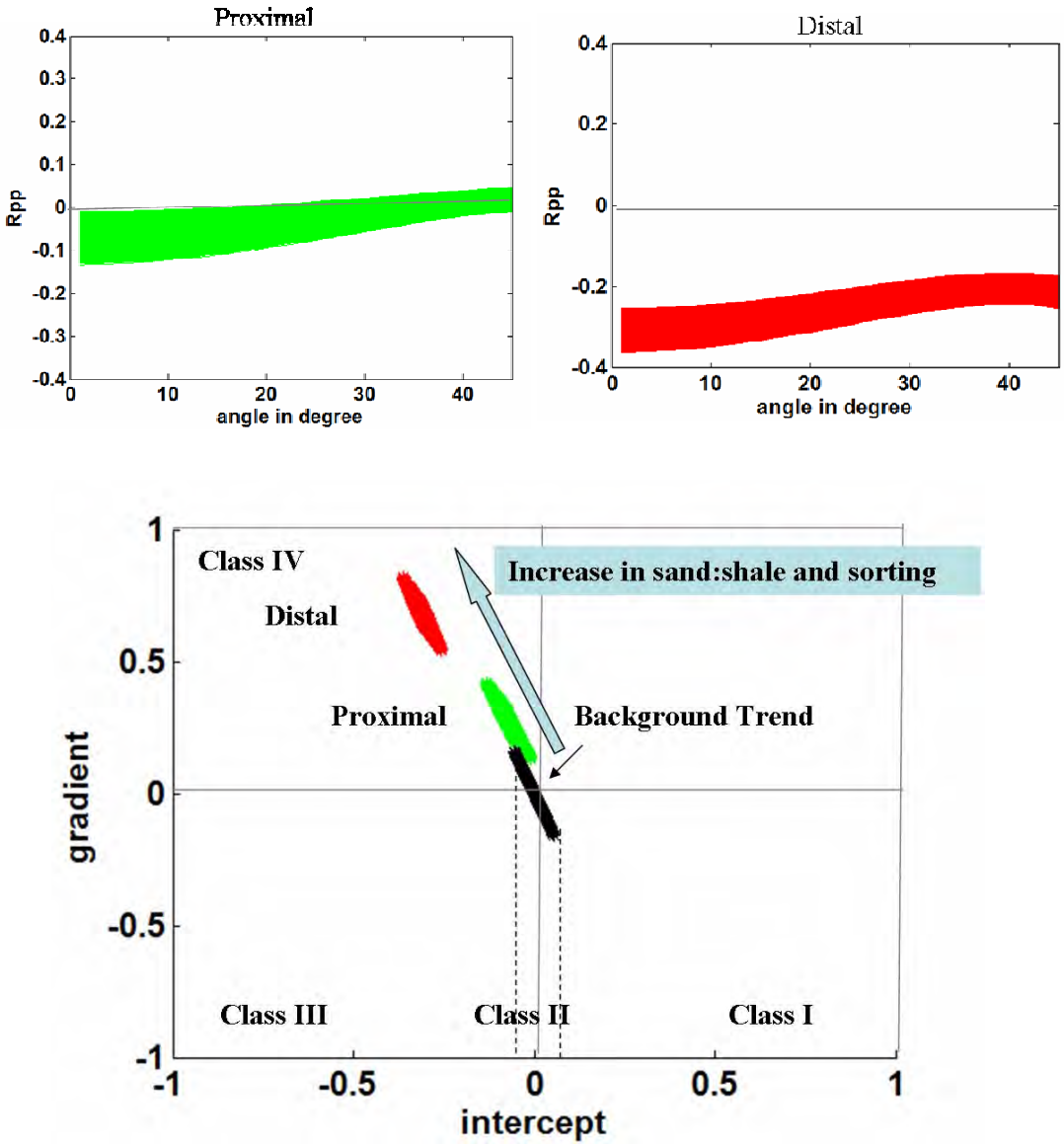

Figure 5.15: The spatial trend of sand/shale ratio and sorting in the AVO plane, using the calibrated rock physics model followed by Monte Carlo AVO simulations. Top: P-to-P reflection coefficient (R_{PP}) vs. incidence angle. Bottom: intercept vs. gradient. The background trend for shale-to-shale reflection is plotted in black points. The reflections from the shale to uncemented sands show class IV AVO response. The magnitudes of intercept and gradient increase from the proximal to the distal location with an increase in sand/shale ratio and sorting.

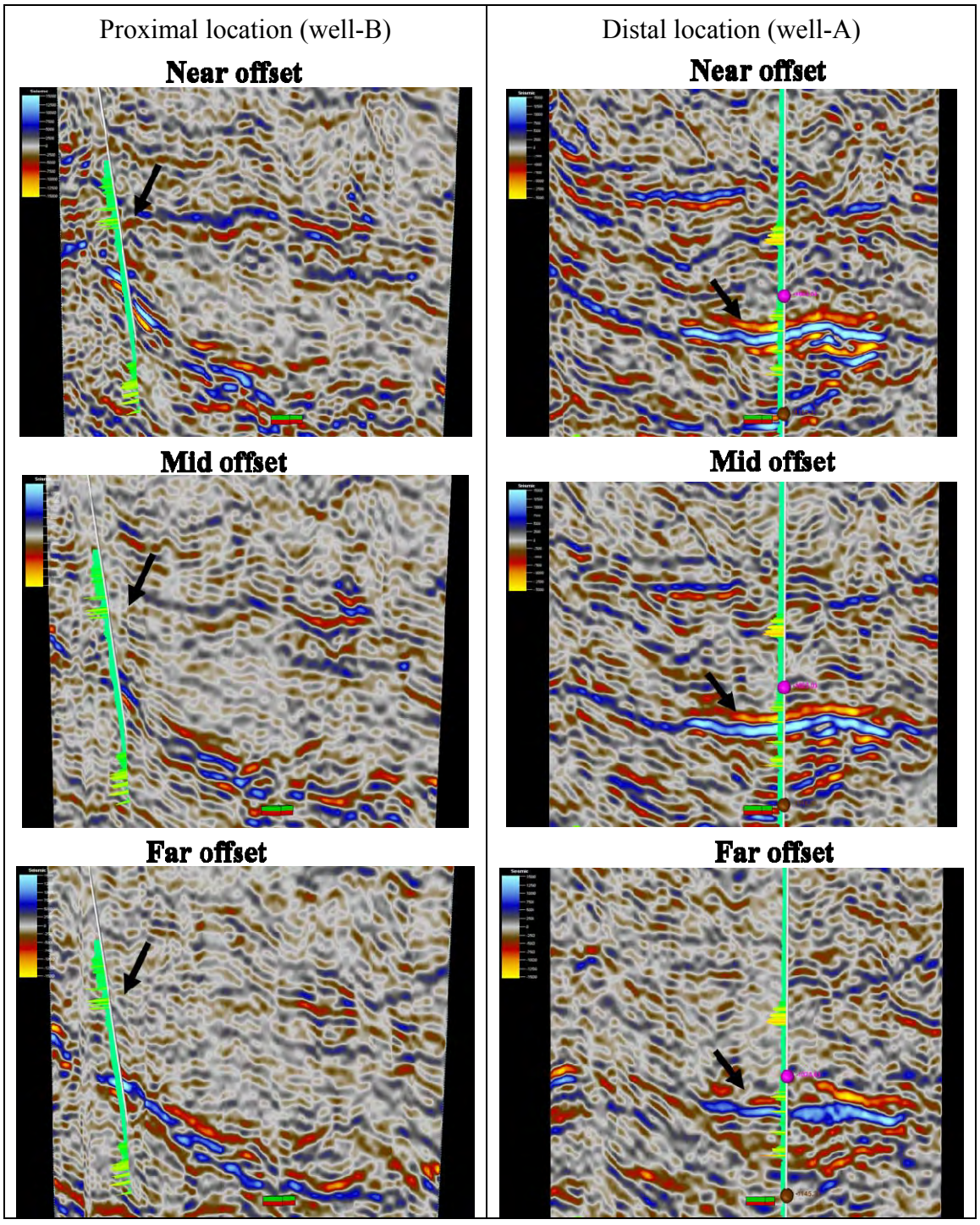

Figure 5.16: Seismic sections from three partial stack volumes demonstrate the class-IV AVO response for reflection from shale to uncemented sands (marked by black arrow in figures). Top: near offset stack (0-18 degree), Middle: mid offset stack (18-35 degree), and Bottom: far offset stack (35-45 degree). The well locations are shown in the seismic sections. Note that the observed AVO response from the data is consistent our modeling results.

The spatial changes in AVO signatures (Figure 5.15) can be attributed to an increase in sand/shale ratio and sorting in the channel sand (lithofacies 1) along the flow direction, as evident from the core observations. These trends can be used as a template to guide the interpretation of observed intercept and gradient from real seismic data. Since these trends incorporate the information from sequence stratigraphy, they can be used to predict the spatial variation in sedimentological parameters. But more than the qualitative trends, we can now make quantitative interpretations about sand/shale ratio and sorting based on the calibrated rock physics model.

5.8.2 Interpreting AVO attributes in terms of porosity and sand/shale ratio

We use the AVO modeling template (Figure 5.15) to guide the interpretation of observed intercept and gradient in terms of porosity and sand/shale ratio. First, we extract the amplitudes along the Top of uncemented, oil sands from three partial stack volumes (Figure 5.17). Within the confinement of the turbidite channel, the magnitude of amplitudes decreases with increasing offset (Class IV AVO). Next, we use these three amplitude maps as inputs in AVO forward modeling equations (Shuey, 1985) for computing AVO intercepts and gradients. The maps of intercepts and gradients are shown in Figure 5.18. We observe a higher negative intercept and a higher positive gradient at the distal well than the proximal well, and this observation is consistent with the template shown earlier in Figure 5.15.

The seismically derived AVO attributes (Figure 5.18) are scaled so that they match histograms of AVO attributes computed from the rock physics models. The scaled values of intercepts and gradients are shown in Figure 5.19, and cross-plotted in Figure 5.20. These values are now suitable to that the template from AVO modeling can be directly applied on them.

Finally, we apply the AVO modeling template to transform seismically derived and properly scaled AVO attributes into maps of porosity and sand/shale ratio (Figure 5.21). The spatial variation of porosity (sorting) and sand/shale ratio are carried from a

sequence stratigraphic model (spill-and-fill model), and quantified using the rock physics model (modified soft-sand model). Our modeling confirms high values of porosity (~40%) and sand/shale ratio (~1) at the distal well. In addition, our modeling predicts high values of porosity (~40%) and sand/shale ratio (~1) at the further downdip locations, which indicate future resource potentials. The results will be important for explorations in analog deep-water environments for deciding whether drilling a well in the downdip direction will be fruitful.

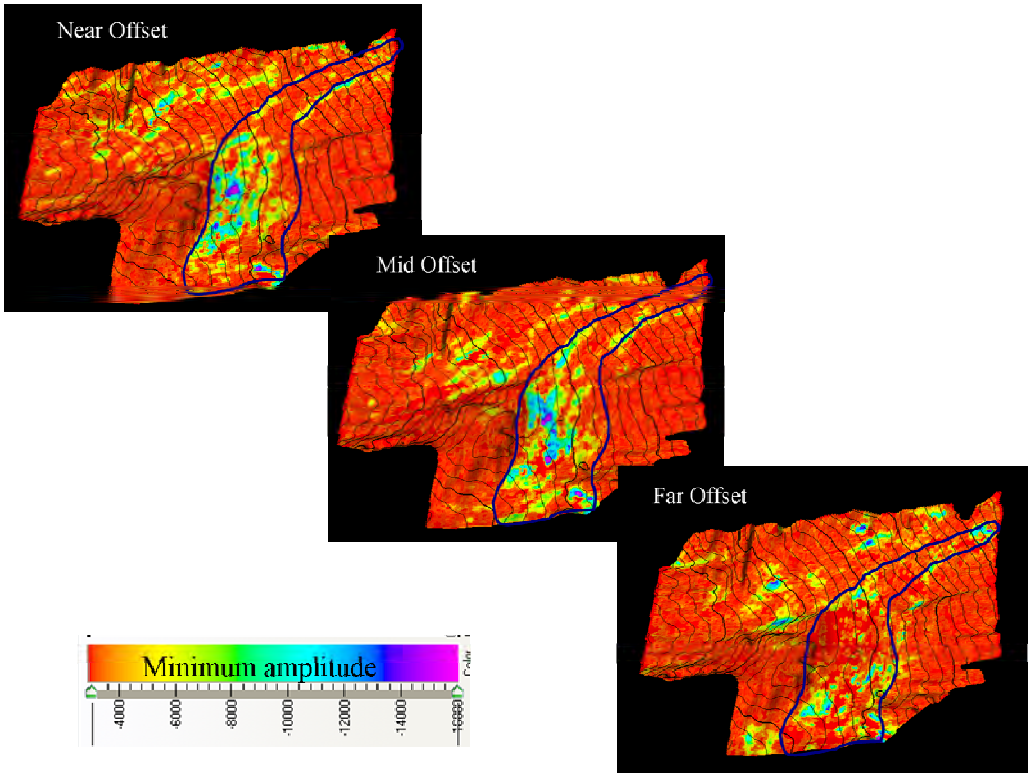

Figure 5.17: Amplitudes extracted along the Top of uncemented, oil sands from three partial stack volumes. The channel is highlighted as blue outline in these amplitude maps. Within the confinement of channel, the magnitude of amplitudes decreases with increasing offset (Class IV AVO).

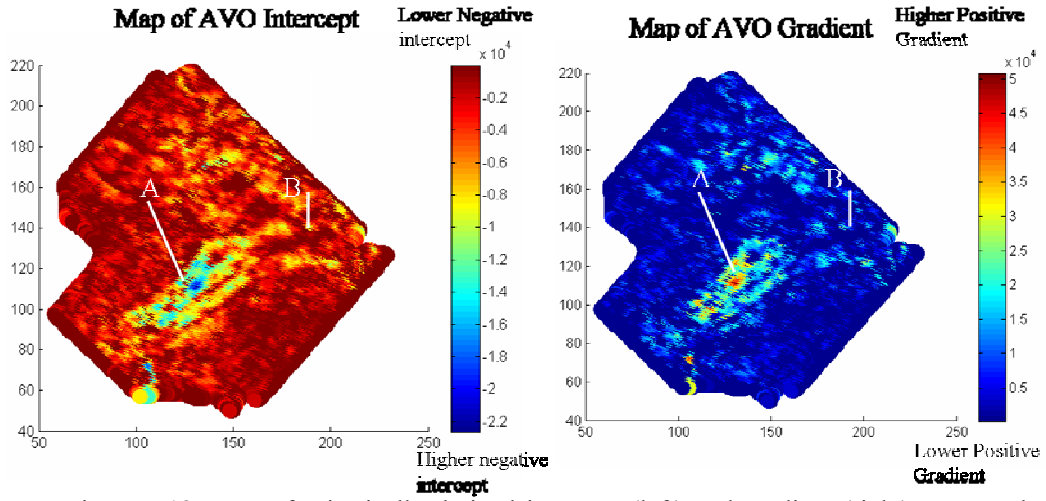

Figure 5.18: Map of seismically derived intercept (left) and gradient (right) computed using three amplitude maps extracted from partial stacks, shown in Figure 5.17. We observe a higher negative intercept and a higher positive gradient at the distal well (well A) than the proximal well (well B).

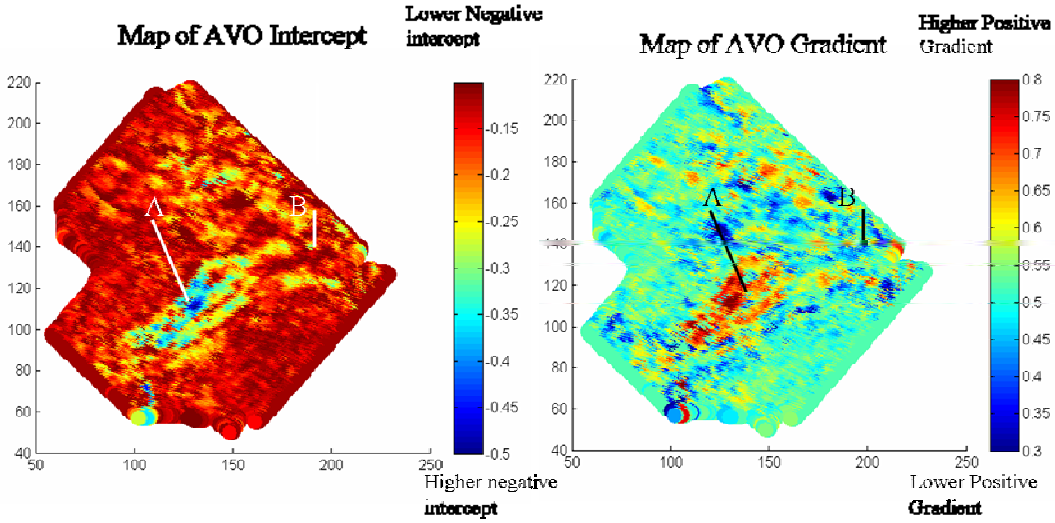

Figure 5.19: Scaled values of seismically derived AVO intercept (left) and gradient (right) for applying the template shown in Figure 5.15.

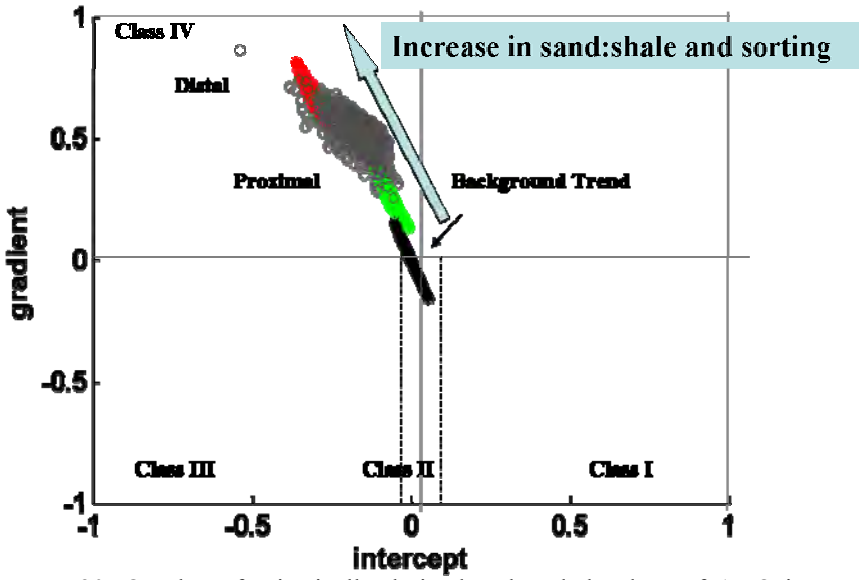

Figure 5.20: Overlay of seismically derived and scaled values of AVO intercepts and gradients on top of the template from AVO modeling. The AVO attributes are selected within the confinements of channel from the maps shown in Figure 5.19.

.

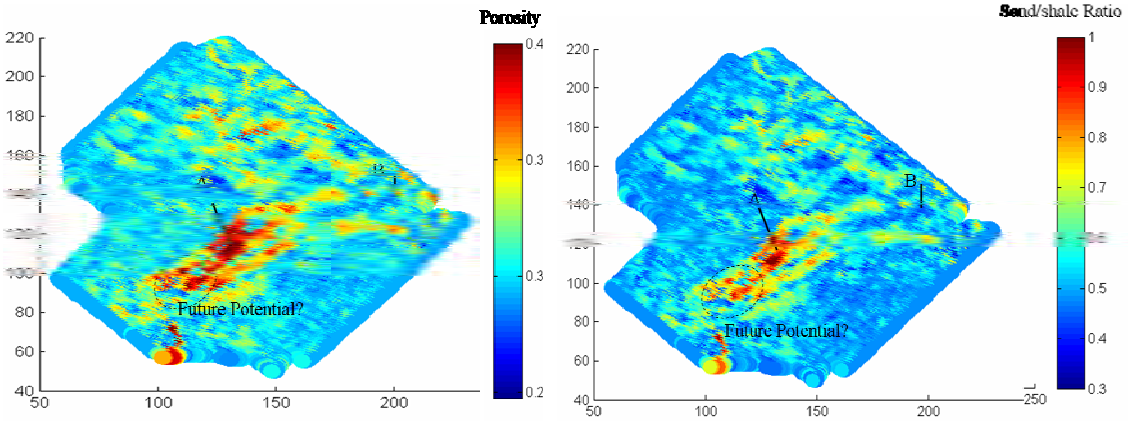

Figure 5.21: Possible map of porosity (left) and sand/shale ratio (right). The spatial variation of porosity (sorting) and sand/shale ratio are carried from sequence stratigraphy and quantified using the rock physics model (modified soft-sand model).

5.9 Conclusions

We have presented a methodology to quantify spatial trends of sedimentological parameters, such as sand/shale ratio and sorting, combining sequence stratigraphic interpretations and rock physics model calibrated at the wells. The method is applied to laminated, channelized, turbidite sand, deposited within minibasin settings in offshore

Equatorial Guinea, West Africa. The log data and core descriptions show an increase in sand/shale ratio and sorting from proximal to distal location. These observations are consistent with the spill-and-fill sequence stratigraphic model in the minibasins settings. We model the effective elastic properties of the uncemented, laminated, channel sands using the modified soft-sand model. Our modeling suggests that the spatial increase in sand/shale ratio and sorting corresponds to an overall decrease in P-impedance, intercept, and gradient. Thus, the trends of mineralogical composition (sand/shale ratio) and textural maturity (sorting) are carried through from sequence stratigraphy, to the AVO plane, via a rock physics model calibrated at the wells. The results are then applied to quantify porosity and sand/shale ratio from observed seismic attributes (inverted P-impedance and AVO attributes), away from the well locations. Our modeling predicts high values of porosity (~40%) and sand/shale ratio (~1) at the further downdip locations indicating future resource potentials. The research findings presented in this chapter can be directly applied for explorations in analog deep-water environments, and can improve the prediction of reservoir properties from seismic amplitudes away from the wells.

5.10 Acknowledgements

This work was supported by the Stanford Rock Physics and Borehole Geophysics project and DOE contract DE-FC26-04NT15506. We acknowledge Hess Corporation for providing the data, and thank Steve Graham, Don Lowe, Steve Uchytil, and Jim Hewlett for valuable discussions.

5.11 References

Aki, K., and Richards, P. G., 1979, Quantitative Seismology: W. H. Freeman and Co.

Anderson, K., Graham, S., and Hubbard, S., 2006, Facies, architecture, and origin of a reservoir-scale sand-rich succession within submarine canyon fill: insights from Wagon caves rock (Paleocene), Santa Lucia Range, California, U.S.A: Journal of Sedimentary Research, 76, 819-838.

Avseth, P., 2000, Combining rock physics and sedimentology for seismic reservoir characterization in North Sea turbidite systems: Ph.D. thesis, Stanford University.

Avseth, P., Mukerji, T. and Mavko, G., 2005, Quantitative Seismic Interpretation: Applying Rock Physics Tools to Reduce Interpretation Risk: Cambridge University Press.

Avseth, P. A. , A. J. van Wijngaarden, T. A. Johansen, and G. Mavko, 2006 , Seismic Fluid Prediction in Heterogeneous Reservoirs : 68th Meeting, EAGE, Expanded Abstracts , 127-130.

Bachrach, R., Dvorkin, J. and Nur, A., 2000, Seismic velocities and Poisson's ratio of shallow unconsolidated sands: Geophysics, 65, 559–564.

Backus, G.F., 1962, Long-wave elastic anisotropy produced by horizontal layering, J. Geophys. Res., 67, 4427-4441.

Bouma, A.H., 2001, Fine-grained submarine fans as possible recorders of long- and short-term climatic changes: Global and Planetary Change: 28, 85-91.

Braaksma,H., Kenter, J.A.M., Proust, J.N., Dijkmans, V., Hoek, T.V. and Drijkoningen, G.G., 2003, Controls on acoustic properties of upper siliciclastic rocks (Boulonnais, northern France): Geophysics, 68, 58-69.

Brown, A., Wright, R.M., Burkart, K.D., Abriel, W.L., 1984, Interactive seismic mapping of net producible gas sand in the Gulf of Mexico: Geophysics, 49, 6, 686-714.

Browne, G.H., and Slatt, R.M., 2002, Outcrop and behind-outcrop characterization of a late Miocene slope fan system, Mt. Messenger Formation, New Zealand: American Association of Petroleum Geologists, Bulletin, 86, 841–862.

Brunt, R., McCaffery,W., and Kneller, B., 2004, Experimental modeling of the spatial distribution of grain size developed in a fill-and-spill mini-basin setting: Journal of Sedimentary Research, 74, 438–446.

Castagna, J. P., 2001,Recent advances in seismic lithologic analysis: Geophysics, 66, 42-46.

Dailly, P., Lowry, P., Goh, K., and Monson, G., 2002, Exploration and development of Ceiba Field, Rio Muni Basin, Southern Equatorial Guinea: The Leading Edge, 21, 1140-1146.

Dvorkin, J. and Nur, A., 1996, Elasticity of high-porosity sandstones: Theory for two North Sea datasets: Geophysics, 61, 1363-1370.

Emery, D., and Myers, K., 1996, Sequence stratigraphy: Blackwell scientific publications, Inc.

Florez, J.M., 2005, Integrating geology, rock physics, and seismology for reservoir-quality prediction: Ph.D. Thesis, Stanford University.

Gassmann, F., 1951, Über die Elastizität poroser Medien, Vierteljahrsschrift der Naturforschenden Gesellschaft in Zürich, 96, 1-23.

Goddard, J.D., 1990, Nonlinear Elasticity and Pressure-Dependent Wave Speeds in Granular Media: Proceedings of the Royal Society of London. Series A, Mathematical and Physical Sciences, 430, 105-131.

Gutiérrez, M., Dvorkin, J., and Nur,A., 2002, Stratigraphy-guided rock physics: The Leading Edge, 21, 98-103.

Hill, R., 1952, The elastic behavior of crystalline aggregate: Proc. Phys. Soc., London A, 65, 349-354.

Jenkins, J., D. Johnson, L. La. Ragione, and H. Makse, 2005, Fluctuations and the effective moduli of an isotropic, random aggregate of identical, frictionless spheres: Journal of the Mechanics and Physics of Solids, 53, 197- 225.

Katahara, K., 2004, Fluid substitution in laminated shaly sands: SEG Expanded Abstracts, 23, 1718 -1721.

Labourdette, R., 2007, Integrated three-dimensional modeling approach of stacked turbidite channels: AAPG Bulletin, 91, 1603-1618.

Latimer, R., Davidson, R., 2000, An interpreter's guide to understanding and working with seismic-derived acoustic impedance data: The Leading Edge, 19, 242-256.

Lerch, C., Strauss, M., Meibur, E., Kneller, B., Glinsky, M., Kuzmin, S., Hall, B., 2006, Numerical Simulation of Turbidity Currents: A Progress Report on Development and Applications: AAPG Annual Convention, Search and Discovery Article #40209.

Lowe, D.R., 2004, Report on core logging, lithofacies, and basic sedimentology of Equitoral Guinea: Hess internatal report.

Makse, A., N. Gland, D. Johnson, and L. Schwartz, 2004, Granular packings: Nonlinear elasticity, sound propagation, and collective relaxation dynamics: Phys. Rev. E 70, 061302.

Marion, D., A. Nur, H. Yin, and D. Han, 1992, Compressional velocity and porosity in sand-clay mixtures: Geophysics, v. 57, p. 554-563.

Mavko, G., T. Mukerji and J. Dvorkin, 1998, The Rock Physics Handbook, tools for seismic analysis in porous media: Cambridge University press, New York, 329.

Mindlin, RD., 1949, Compliance of elastic bodies in contact: ASME Journal of Applied Mechanics, 71, A-259 -268.

Mulholland, J.W., 1998, Sequence stratigraphy: basic elements, concepts and terminology: The Leading Edge, 37-40.

Mukerji, T., Jorstad, A., Avseth, P., Mavko, G., and Granli, J. R., 2001, Mapping lithofacies and pore fluid probabilities in a North Sea reservoir: Seismic inversions and statistical rock physics, Geophysics, 66, 988-1001.

Neal, J., Risch, D. and Vail, P., 1993, Sequence stratigraphy- a local theory with global success: Oilfield review, 51-62.

Normak,W.R., and Carlson, P.R., 2003, Giant submarine canyons; is size any clue to their importance in the rock record?, in Chan, M.A., and Archer, A.W., eds., Extreme Depositional Environments; Mega End Members in Geological Time: Geological Society of America, Special Chapter 370, p. 175–190.

Pedersen, B.K. and Nordahl, K., 1999, Petrophysical evaluation of thin beds: a review of the Thomas-Stieber approach: Course 24034 Formation Evaluation 1, Semester report.

Piper, D.J.W., 1978, Turbidites, muds and silts on deep-sea fans and abyssal plains. In: Sedimentation in Submarine Canyons, Fans and Trenches (Eds D.J. Stanley and G. Kelling), 163-176.

Payton, C.E., 1977, Seismic stratigraphy- applications to hydrocarbon explorations: AAPG Memoir, 26, The American association of petroleum geologists, 516.

Posamentier, H.W., and Allen, G.P., 1993, Sequence stratigraphy and facies model of an incised valley fill: the Gironde estuary, France: Journal of Sedimentary Research, 63, 378-391.

Satterfield, W.M., and Behrens, E.W., 1990, A late Quaternary canyon/channel system, northwest Gulf of Mexico continental slope: Marine Geology, 92, 51–67.

Shepard, F.P., and Dill, R.F., 1966, Submarine Canyons and Other Sea Valleys: Chicago, Rand McNally, 381 p.

Stow, D.A.V., Bowen, A.J., 1980, A physical model for the transport and sorting of fine-grained sediment by turbidity currents: Sedimentology, v. 27, 31-46.

Thomas, E. C., and Stieber, S. J., 1975, The Distribution of Shale in Sandstones and Its Effect Upon Porosity: Trans. Of the 16th Annual Logging Symposium of the SPWLA paper T.

Wagoner, J.C.Van., Mitchum, R.M., Campion, K.M., and Rahmanian, V.D., 1990, Siliciclastic sequence stratigraphy in well logs, cores and outcrops: The American Association of Petroleum Geologists, Methods in Exploration Series, no. 7.

Walton, K., 1987, The effective elastic moduli of a random pack of spheres: J. Mech. Phys. Sol., 35, 213-226.

Winker, C.D., and Booth, J.R., 2000, Sedimentary dynamics of the salt-dominated continental slope, Gulf of Mexico: Integration of observations from the seafloor, near-surface, and deep subsurface, in Weimer, P., Slatt, R.M., Coleman, J., Rossen, N.C., Nelson, H., Bouma, A.H., Styzen, M.J., and Lawrence, D.T., eds., Deepwater reservoirs of the world, 20th Annual Research Conference Proceedings: Society of Economic Paleontologists and Mineralogists, Gulf Coast Section, 1059–1086.

Zeng, H., Beckus, M.M., Barrow, K.T and Tyler, N., 1996, Facies mapping from three dimensional seismic data: potential and guidelines from a tertiary sandstone-shale sequence model, Powderhorn field, Calhoun Country, Texas: AAPG Bulletin, 90, 16-46.

Zimmer, M., 2003, Seismic velocities in unconsolidated sands: Measurements of pressure, sorting, and compaction effects. Ph.D. dissertation, Stanford University.

Chapter 6
Impact of carbonate cement on seismic response: combining stratigraphy and rock physics

"All truths are easy to understand once they are discovered; the point is to discover them."
-- Galileo Galilei

6.1 Abstract

Reservoir quality in sandstone is often affected by the precipitation of carbonate cement and its subsequent dissolution. We present a quantitative link between carbonate cement and seismic impedance by combining stratigraphic cycles and rock-physics models. We find that the carbonate-cemented sandstones from deep-water Equatorial Guinea, West Africa, are sedimentologically extremely heterogeneous. For example, their mineralogy, grain-size, sorting, shaliness and cement volume vary considerably, even within a depth interval of ~60 meter. However, P-impedance is primarily controlled by cement volume. The variation in cement volume can be linked with two distinct

stratigraphic cycles: the fining-upward cycles and the coarsening-upward cycles, and these cycles exhibit distinct signatures on the P-impedance -versus- porosity crossplot. The carbonate-cemented sandstones from the fining-upward cycles are often associated with extensive cementation, resulting in lower porosity and higher P-impedance. In contrast, those from the coarsening-upward cycles are often associated with dissolution, resulting in higher porosity and lower P-impedance. The porosity and carbonate cement volume in different stratigraphic cycles are then used as constraints in the modified differential effective medium (DEM) model for predicting P-impedance -versus- porosity trends. The calibrated DEM model with well data shows an increase in P-impedance, intercept and gradient of class I AVO with an increase in carbonate cement volume. Our results can be useful to quantitatively interpret seismic attributes in carbonate-cemented sandstones for predicting reservoir quality.

6.2 Introduction

Carbonate diagenetic processes, i.e., cementation and dissolution, can degrade or enhance the reservoir quality of siliciclastic rock. For example, precipitation of extensive calcite cement during diagenesis can strongly modify the depositional porosity and permeability of a sandstone reservoir (Kantorowicz et al., 1987; Saigal and Bjørlykke, 1987; Bjørkum and Walderhaug, 1990; Morad, 1998). Carbonate cement may also make flow paths more tortuous, because it is commonly concentrated in layers or concretions rather than being uniformly distributed (McBride et al., 1995). These cemented zones often segment a reservoir into relatively isolated compartments, thereby creating barriers to lateral or vertical flow of hydrocarbons and formation waters (Kantorowicz et al., 1987). Although carbonate cements are generally considered to be negative factors for reservoir quality and fluid flow, often they increase rigidity of the sediments, enabling them to better withstand compaction from overburden stress (Pittman and Larese, 1991). The reservoir quality in carbonate-cemented sandstones improves by subsequent dissolution of carbonate cement that generates secondary porosity and enhances permeability.

Even though carbonate diagenesis can have a major impact on reservoir quality of siliciclastic rock, there is no example in the literature that quantifies the link between carbonate diagenesis and seismic impedance. We present a quantitative link between carbonate cement volume and seismic impedance by combining stratigraphic cycles and an appropriate rock physics model. We use an integrated dataset from the carbonate-cemented sandstone interval from deep-water Equatorial Guinea, West Africa. In our study area, although the carbonate-cemented sandstones are sedimentologically extremely heterogeneous, P-impedance is primarily controlled by cement volume. The variation in carbonate cement volume can be associated with two distinct stratigraphic cycles: the fining-upward cycles and the coarsening-upward cycles. We find that cemented sandstones from these two stratigraphic cycles show distinct signatures on the P-impedance -versus- porosity crossplot. The carbonate-cemented sandstones from the fining-upward cycles usually exhibit extensive carbonate cement, lower porosity and higher P-impedance. In contrast, those from the coarsening-upward cycles usually exhibit dissolution of cement and detrital grains, higher porosity and lower P-impedance.

In order to quantify the effects of cement volume and porosity on P-impedance, we test the predictions of porosity -versus- P-impedance trends by granular-medium models and differential effective-medium models against well data. Different granular-medium models have been shown to predict the effective elastic properties of quartz-cemented sandstones, such as the contact cement model (Dvorkin et al., 1996; Mavko et al., 1998), the constant cement model (Avseth et al., 2005), and the stiff-sand model (Gal et al., 1998). However, these models have not been tested rigorously for carbonate-cemented sandstones. Our study shows that these granular-medium models fail to predict the porosity-versus-P-impedance trend for the carbonate-cemented sandstones, but this trend can be reasonably predicted using the modified Differential Effective Medium Model (Mukerji et al., 1995). In this model, we constrained the input parameters, such as mineral end-points and porosity from interpretations of stratigraphic cycles.

In the remaining three sections of this paper we first present how P-impedance in carbonate-cemented sandstones is controlled by different sedimentological parameters,

such as mineralogy, sorting, shaliness and cement volume. Next we establish a link between carbonate cement volume and P-impedance by identifying stratigraphic sequences from well data. Finally, we test the predictions of effective medium models (granular-medium models as well as inclusion based models) to quantify the impact of carbonate cement volume on P-impedance, and AVO intercept and gradient.

6.3 Sedimentological parameters in carbonate-cemented sandstones and their impact on P-impedance

In this section, we identify how sedimentological variations within carbonate-cemented sandstones affect seismic impedance. We have used a comprehensive dataset from deep-water Equatorial Guinea, West Africa. The dataset contains measurements at different scales, such as 3D post-stack seismic data, well logs, cores, thin-sections, XRD, and grain-size data. The post-stack seismic and well logs from our study area, calibrated with core observations, show distinct signatures of carbonate cementation. For example, the seismic reflection shows that carbonate-cemented sandstones underlying uncemented sandstones can generate significant impedance contrast (Figure 6.1). These cemented sandstones are a seismically mappable event over a lateral distance of few kilometers, and therefore might act as a potential flow-barrier affecting reservoir quality.

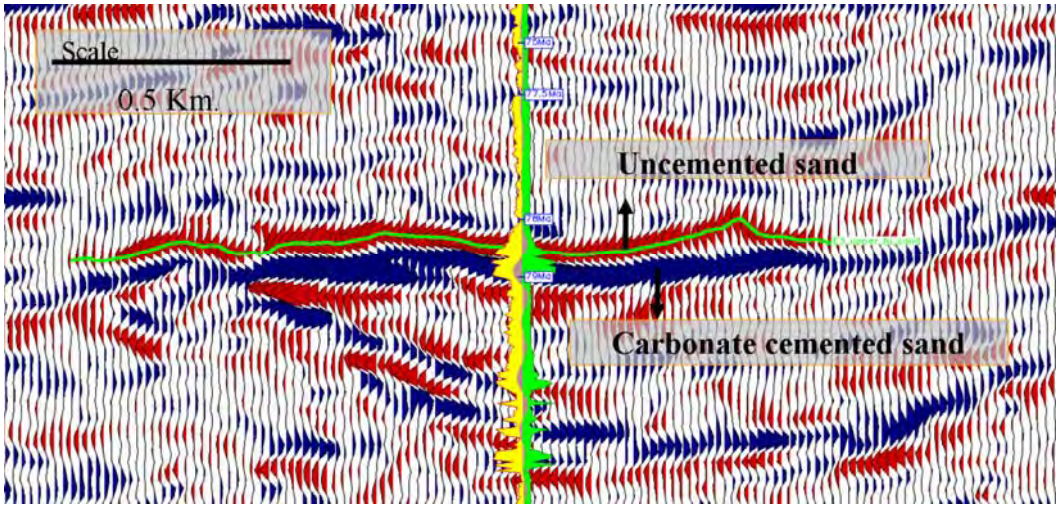

Figure 6.1: Post-stack, time-migrated seismic section from Equatorial Guinea, offshore West-Africa. The carbonate-cemented sandstones generate a strong reflection event when they occur beneath uncemented sands. The cemented interval is laterally persistent for several km and therefore might act as a potential flow-barrier affecting reservoir quality.

The well logs reveal that carbonate-cemented sandstones have distinctively higher velocity and P-impedance than uncemented lithofacies, i.e., thick bedded sand, thick-thin bedded sand, thin bedded sand, conglomerate and mudstone (Figure 6.2). These uncemented lithofacies are typical of any channelized turbidite sequence. They were identified based on grain-size, bed-thickness and sand-to-shale ratio from core observations by Lowe (2004).

We identify variations in multiple sedimentological parameters within the carbonate-cemented sandstone interval—mineralogy of cement, grain size and sorting, cement volume, and shaliness—and determine their impact on well log derived P-impedance. Mineralogy, sorting and shaliness have been reported to affect seismic velocities and impedances in uncemented sandstones (e.g., Avseth et al., 2000; Florez et al., 2004), and cement volume has been reported to affect seismic responses in quartz-cemented sandstones (Dvorkin et al., 1996). Therefore, in this study we test how these parameters impact seismic impedance in carbonate-cemented sandstones.

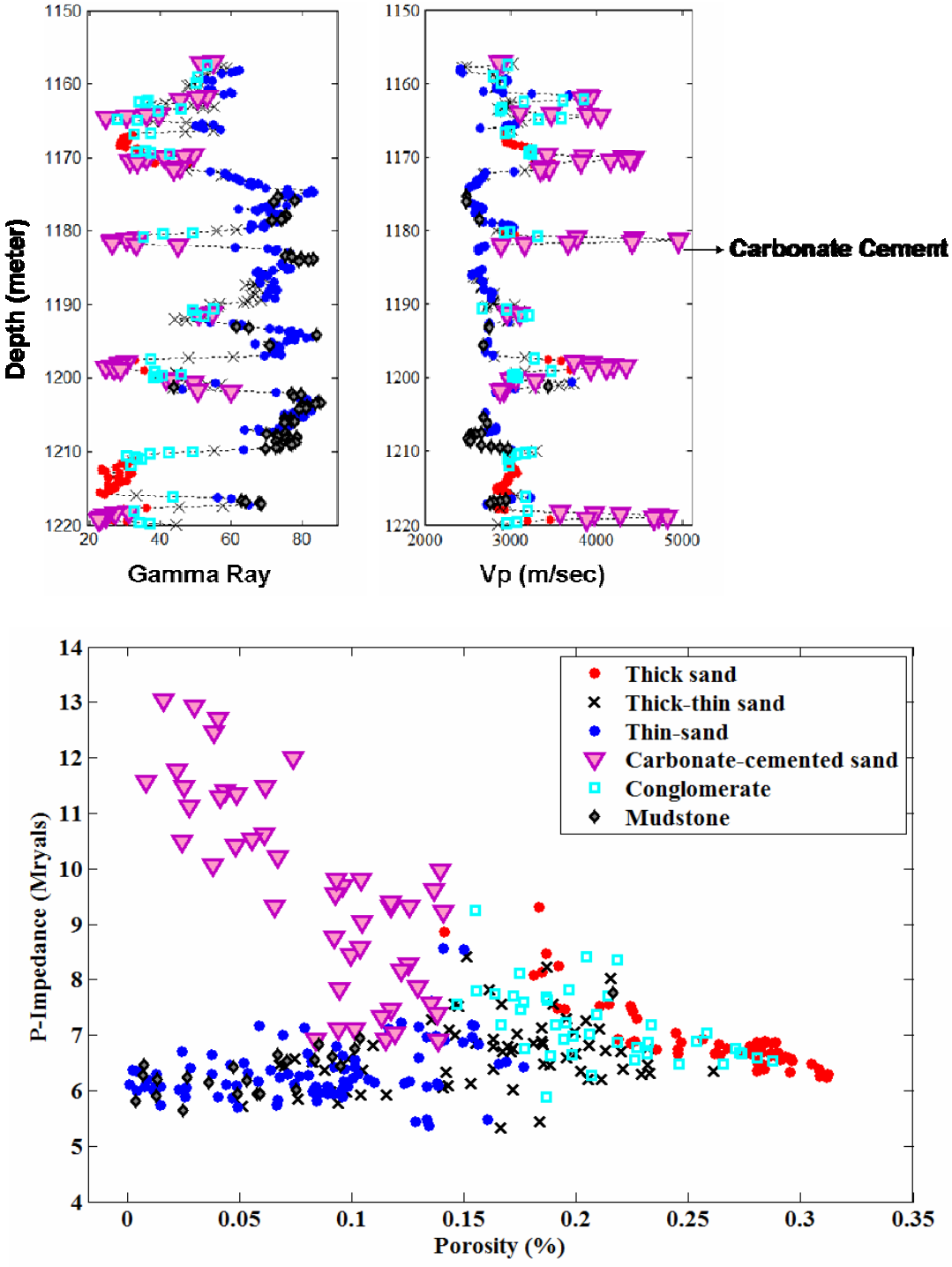

Figure 6.2: Distinct signature of carbonate-cemented sandstones in well logs. Top: well-log response containing cemented sand intervals. Bottom: P-impedance vs. total porosity color-coded by different facies. The carbonate-cemented sandstones (purple triangles) have higher V_P and P-impedance than other uncemented lithofacies.

6.3.1 Mineralogy of Cement

The XRD analysis of 11 samples from the carbonate-cemented sandstone interval show that carbonate cement mineralogy varies from Calcite (Ca-rich) to Ankerite (Mg-rich) (Figure 6.3). Calcite is the dominant cement mineralogy above depth 1181 meter, and ankerite is the dominant cement mineralogy below this depth. Ankerite is an intermediate product between calcite (the calcium-rich end member) and dolomite (the magnesium-rich end member). The other major phases in cemented sand include quartz, K-feldspar and plagioclase. There are trace amounts of pyrite, illite, smectite, kaolinite and chlorite.

Calcite and ankerite cements do not reveal distinct trends in the V_P-V_S and the I_P-porosity crossplot. Figure 6.4A shows the V_P/ V_S of carbonate-cemented sandstones from well logs color-coded by cement mineralogy. The velocities represent that of completely brine saturated rock, computed using Gassmann fluid substitution equations (Gassmann, 1951). The empirical V_P/V_S relations of Greenberg and Castagna (1992) for different lithologies, e.g., sandstone, shale, limestone and dolomite are also plotted in the same figure. The V_P/V_S of calcite cemented sandstone shows a slightly higher trend than predicted by the empirical relation for limestone. The V_P/V_S ratio of ankerite-cemented sandstones shows a large scatter. Figure 6.4B shows I_P-versus-porosity from the same well logs, color-coded by cement mineralogy. Ankerite-cemented sandstones have slightly higher intercept in the I_P-porosity crossplot compared to the sandstones rich in calcite cement.

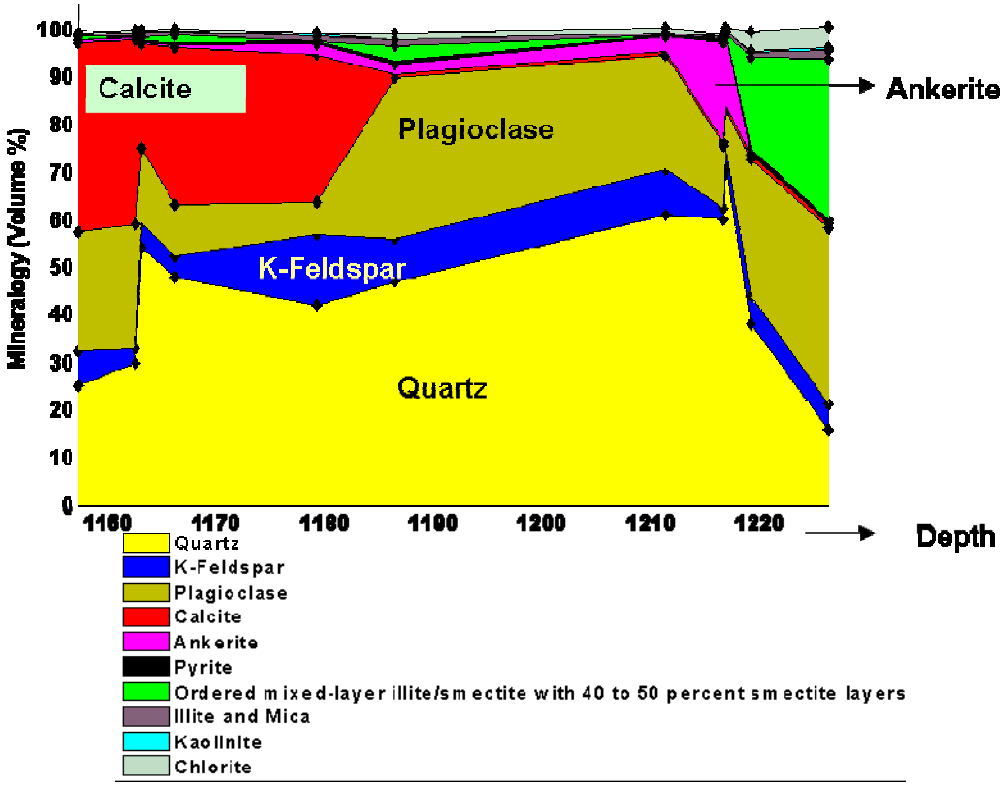

Figure 6.3: Two different mineralogies of carbonate cement: calcite and ankerite, as evident from XRD analysis of 11 samples from the carbonate-cemented sandstone interval. The dominant phases are quartz, K-feldspar and plagioclase with trace amounts of pyrite, illite, smectite, kaolinite and chlorite.

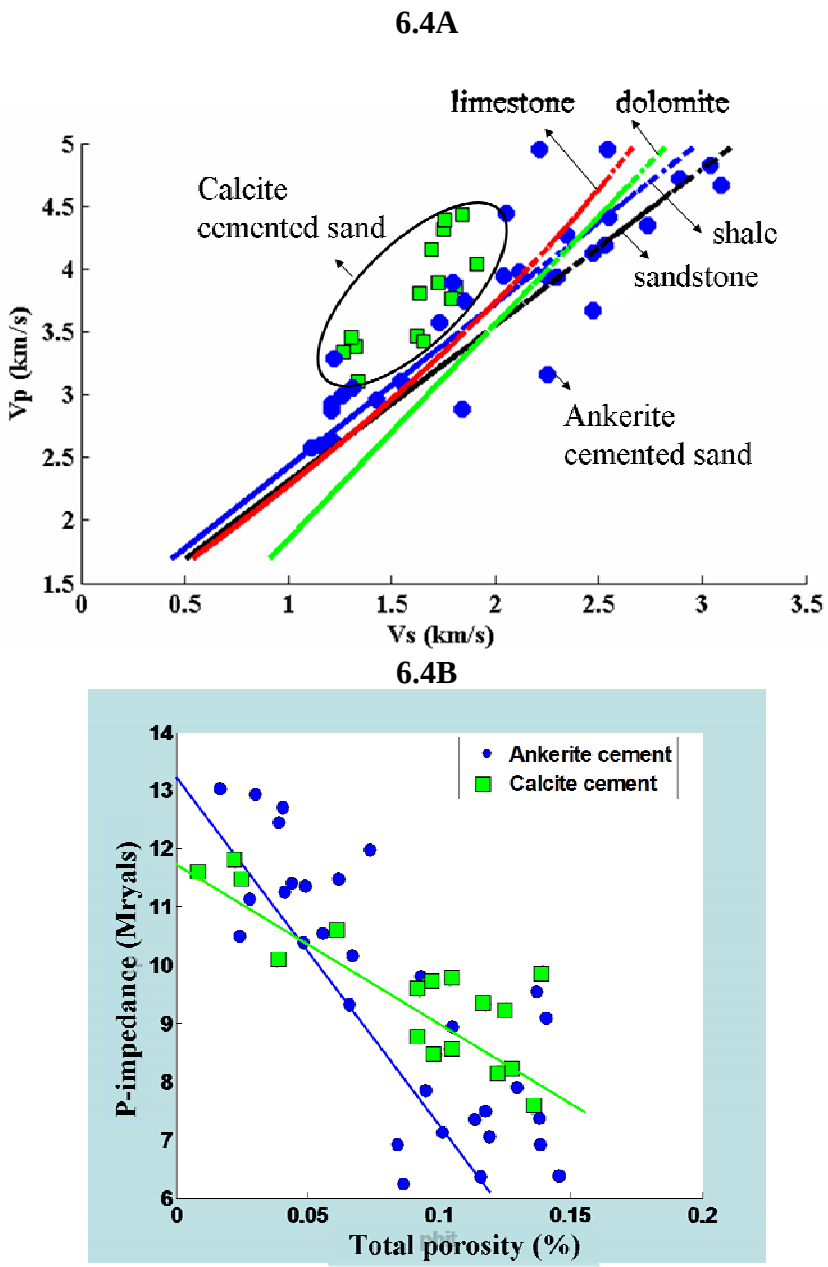

Figure 6.4: (A) Comparisons of the V_P/V_S of the carbonate-cemented sandstone from well logs with empirical V_P/V_S relations by Greenberg and Castagna (1992). The green rectangles are from the calcite interval, and blue circles are from the ankerite interval. The data show a wide range of scatter. (B) P-impedance vs. total porosity from well logs color-coded by cement mineralogy. Although the ankerite-cemented sandstones have slightly higher P-impedance than calcite-cemented sandstones, they do not display distinct trends.

6.3.2 Grain size and Sorting

Grain size and sorting are important attributes of sedimentary texture. Figure 6.5A shows grain size distribution obtained from laser particle size analysis (LPSA) of core samples. The grain-size is expressed in phi-scale (negative logarithm (base 2) of grain-size measured in millimeters). There are a number of quantitative definitions of sorting in the sedimentology literature (eg., Otto, 1939; Inman, 1957, Folk and Ward, 1957 and McCammon, 1962). We use the definition by Folk and Ward (1957) to compute the sorting coefficient:

$$Sorting\_coefficient = \frac{P_{84} - P_{16}}{4} + \frac{P_{95} - P_5}{6.6} \tag{6.1}$$

where P represents percentile of grain size in phi-scale. A higher value of sorting coefficient represents poor sorting, and a lower value represents better sorting.

We observe that grain-size and sorting have practically no influence on the porosity and P-impedance of carbonate-cemented sandstones. Figure 6.5B shows sorting coefficient-versus-grain size colorcoded by P-impedance. In this figure, the grey points indicate data from all the lithofacies within a sequence, while the colored points indicate data only from the carbonate-cemented sandstones. We observe an inverted 'V' pattern in the grain size-versus-sorting domain. Sorting is better for coarse and fine end-members of grain-size. The lowest sorting coefficient, 0.75, is observed for coarse sand. The sorting becomes poorer by mixing different grain-sizes. The sorting coefficient increases from 0.75 to 2.75 as fine fractions are added to the coarse fractions. Figure 6.5C shows the I_P-porosity crossplot color-coded by sorting coefficient. The variation in sorting does not provide any trend in the I_P-porosity crossplot. Although sorting has been previously reported to affect the I_P-porosity trend in uncemented sandstones from the same study area (Dutta et al., 2007), we find that this is not the case in carbonate-cemented sandstones.

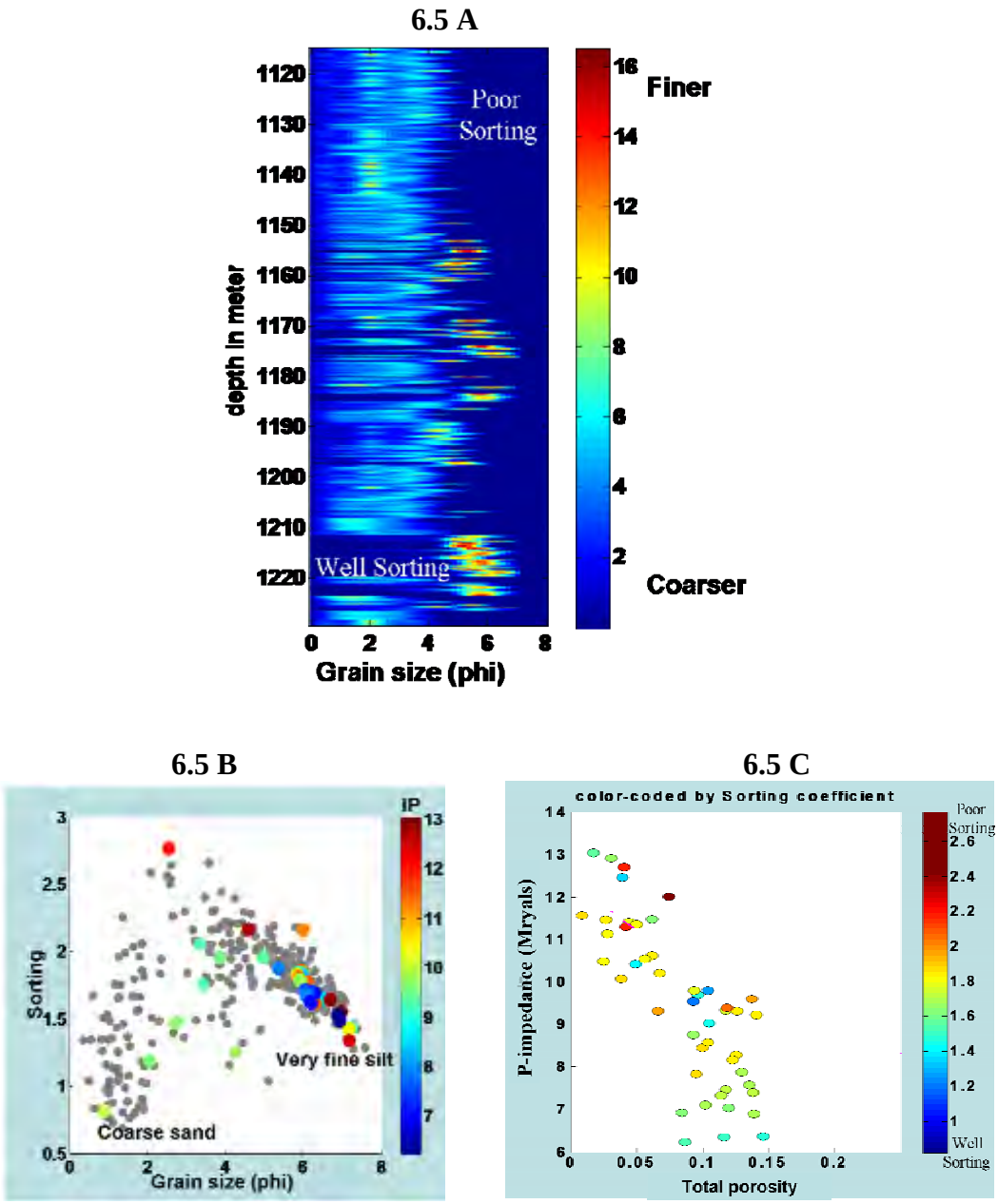

Figure 6.5: (A) Grain size distribution in carbonate-cemented sandstones from laser particle-size analysis data. A wider distribution in grain-size indicates poorer sorting. (B) Sorting coefficient vs. median grain size color-coded by P-impedance (IP). The grey points indicate data from the uncemented lithofacies in the same sequence, whereas the colored points indicate data from the carbonate-cemented sandstones. The data reveal an inverted 'V' in the grain size- sorting domain. Sorting is linked with grain-size (poorest sorting by mixing different grain sizes), but not with P-impedance. (C) P-impedance vs. total porosity color-coded by sorting coefficient shows that P-impedance is not affected by sorting.

6.3.3 Cement Volume

The cement volume in the carbonate-cemented sandstones is highly variable, as indicated by XRD analysis, and the P-impedance depends significantly on the amount of carbonate cement. Figure 6.6 shows three representative thin sections illustrating extensive variation in carbonate cement volume. When carbonate cements are present in higher volumes, they can occlude almost all the interparticle porosity. Dissolution and leaching reduces cement volume and creates secondary porosity. Extensive dissolution of cement leads to significant secondary porosity and interparticle macroporosity. The secondary porosity increases with an increase in degree of dissolution.

The carbonate cement volume significantly controls P-impedance, as shown in Figure 6.7. In this figure, the cement volume is obtained from XRD analysis at different depths, and P-impedance is from corresponding depths using well logs. We observe that P-impedance increases from 6 Mrayls to 13 Mrayls, with carbonate cement volume increasing from 2% to 36%.

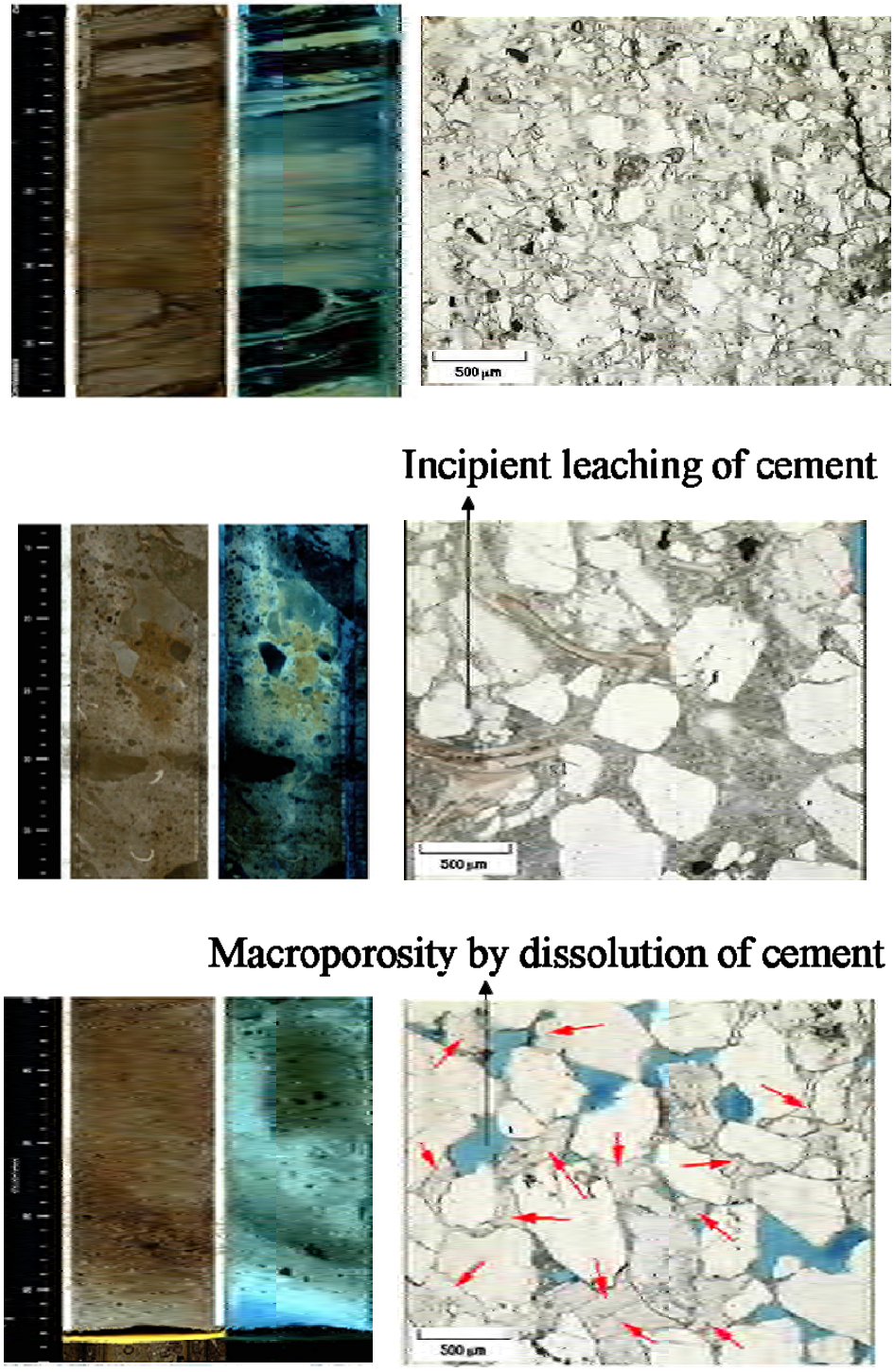

Figure 6.6: Core and thin-section evidence of extensive variation in carbonate cement volume. Core photos are in plain light and ultraviolet light. Top: extensive carbonate cementation occluding all interparticle pore space. Middle: incipient dissolution of carbonate cements creating a small secondary porosity. Bottom: dissolution of cements creating significant secondary porosity and macropores.

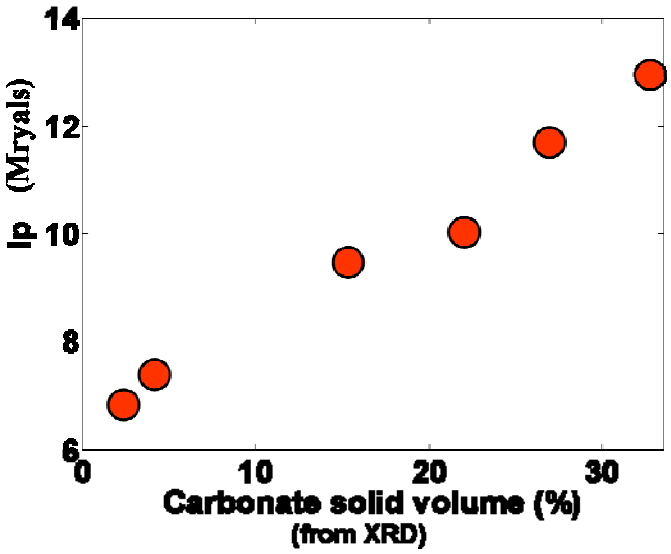

Figure 6.7: P-impedance (I_P) increases from 6 Mrayls to 13 Mrayls as carbonate cement volume increases from 2 to 36 %. The carbonate cement volume is obtained from XRD analysis, and I_P is obtained from corresponding depths at the well.

6.3.4 Shaliness

In order to understand the effect of shaliness on P-impedance, we crossplot P-impedance-versus-porosity and color-code the data using gamma-ray index. We assume that the gamma-ray index is an indicator of shaliness for these carbonate-cemented sandstones. The cemented sands with higher shaliness are associated with higher porosity (Figure 6.8). This observation contradicts the usual relationship between clay content and porosity: usually increasing shaliness adds clay in the pore-network and decreases porosity (e.g., Han et al., 1986). In order to explain this anomaly, and for an improved understanding of carbonate diagenesis from seismic impedance, we establish links between sequence stratigraphic cycles, carbonate diagenesis and seismic impedance.

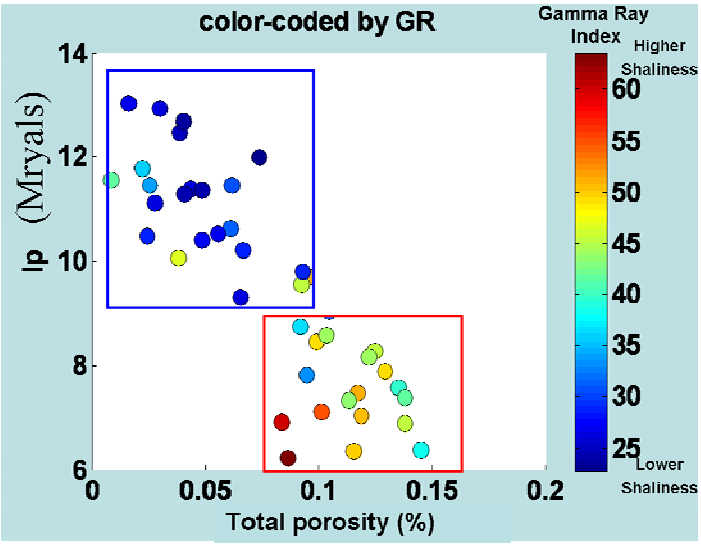

Figure 6.8: P-impedance (I_P) vs. total porosity color-coded by gamma-ray index, an indicator of shaliness in sandstones. The carbonate-cemented sandstones with higher shaliness are associated with higher porosity and lower I_P (highlighted in red rectangle). And, the carbonate-cemented sandstones with lower shaliness are associated with lower porosity and higher I_P (highlighted in red rectangle).

6.4 Links between stratigraphic cycles, carbonate diagenesis and seismic impedance

Seismic impedance in our study area can be linked with carbonate diagenesis (cementation and subsequent dissolution) by identifying the two basic stratigraphic cycles: the fining-upward cycles and the coarsening-upward cycles. We identify these cycles based on the patterns in gamma-ray logs (Figure 6.9 and Figure 6.10). Each fining-upward cycle on a gamma-ray log represents a transgression, and a flooding surface demarcates the maximum transgression, i.e., when the gamma-ray index reaches its maximum value (Figure 6.9). Similarly, each coarsening-upward cycle on the gamma-ray log represents a regression, and an incision surface demarcates the maximum regression, i.e., when the gamma-ray index reaches its minimum value (Figure 6.10).

The carbonate-cemented sandstones associated with the fining-upward and the coarsening-upward cycles reveal distinct signatures in the porosity-versus-I_P crossplot (Figure 6.9 and Figure 6.10). The sediments from the fining-upward cycles are usually associated with lower shaliness, lower porosity, and higher I_P (Figure 6.9). Those from

the coarsening-upward cycles exhibit higher shaliness, higher porosity, and lower I_P (Figure 6.10). The porosity is selectively enhanced (secondary porosity) in the carbonate-cemented sandstones when they occur below the incision surface. Such association of secondary porosity with incision surfaces and coarsening-upward cycles may explain why samples with relatively higher shaliness can have higher porosity.

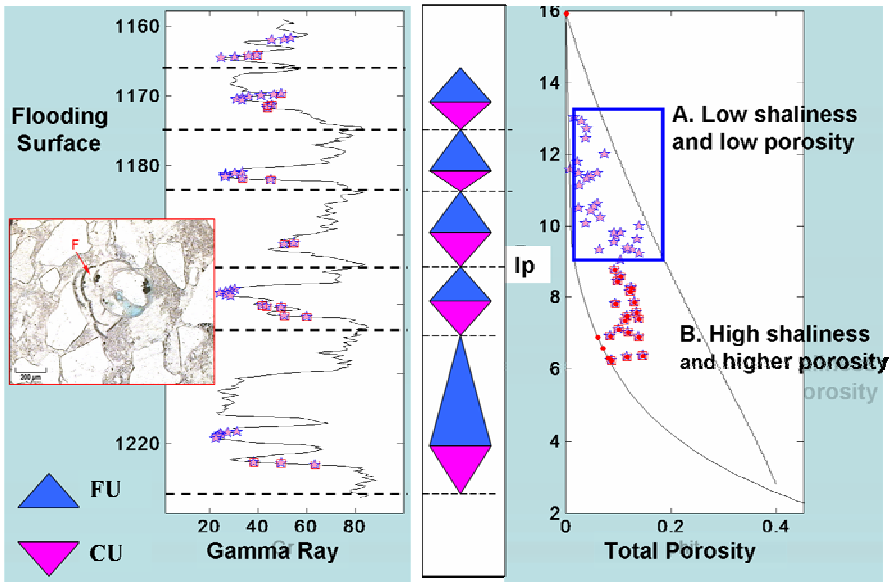

Figure 6.9: Left: Gamma ray log with para-sequences bounded by flooding surfaces. Each para-sequence is divided in two stratigraphic cycles: fining-upward (FU) and coarsening-upward (CU). The colored points indicate corresponding depths of carbonate cementation as evident from cores. Right: P-impedance (I_P) vs. total porosity from well logs with Hashin-Shtrikman upper and lower bounds computed for a composite of calcite and water. The sediments associated with fining-upward cycles show extensive cementation and exhibit higher I_P and lower porosity (data in blue rectangle). The thin-section shows carbonate cement (dark grey-color) and foraminifera (F) which probably acted as nucleation sites for cementation.

The variation in carbonate cement volume due to dissolution and evolution of secondary porosity are evident from the thin-sections. For example, the thin-sections from the fining-upward cycles exhibits extensive carbonate cementation with presence of bio-clast lags (Figure 6.9). These bio-clast lags could have acted as nucleation sites for carbonate cement. In contrast, thin-sections from the coarsening-upward cycles show evidence of dissolution at the margin of existing carbonate cement. The neighboring grains are commonly ragged, suggesting that they were bordered by cement prior to

dissolution. In order to quantify such variation in cement volume from seismic data, it is essential to identify an appropriate rock physics model.

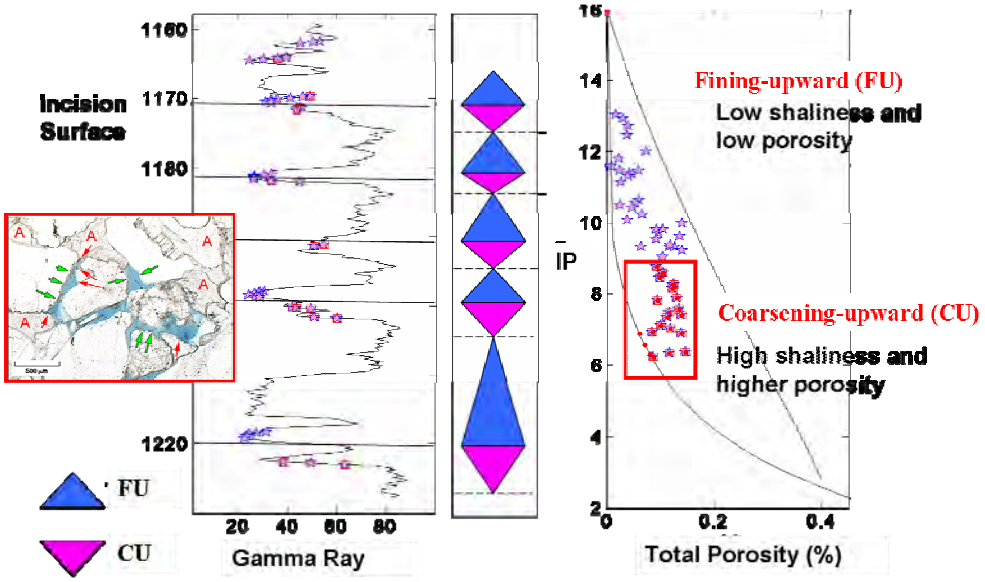

Figure 6.10: Left: Gamma ray log with incision surfaces. Right: P-impedance (I_P) vs total porosity plot. The sediments from coarsening-upward cycles are usually associated with dissolution of cement and detrital grains due to percolation of meteoric water, and exhibit lower I_P and higher porosity (data in red rectangle). In the thin-section, the margins of the ankerite cement (A) show evidence of leaching (red arrows), and the neighboring grains are ragged (green arrows), suggesting they were bordered by cement prior to dissolution.

6.5 Rock physics model for carbonate-cemented sandstones

In section 6.3, we showed that although carbonate-cemented sands are sedimentologically highly heterogeneous, P-impedance is primarily controlled by carbonate cement volume. Therefore, for quantifying the impact of carbonate cement volume on P-impedance, we attempt to identify an appropriate rock physics model. To do this, we test the P-impedance (I_P)-versus-porosity trends predicted by granular-medium models and inclusion models against well data.

6.5.1 Granular-Medium Models

The granular-medium models, which have been previously shown by other authors to predict effective elastic properties in quartz-cemented sandstones (e.g., Dvorkin et al.,

1996; Gal et al., 1998; Avseth el al., 2000), fail to predict I_P-versus-porosity trends in carbonate-cemented sandstones. The I_P-versus-porosity trends measured at the well in carbonate-cemented sandstones are shown in Figure 6.11, along with those predicted by three different granular-medium models. The modified upper and lower Hashin-Shtrikman bounds (Mavko et al., 1998) computed for a mixture of calcite and water are also plotted in the same figure.

The contact cement model (Dvorkin et al., 1996) does not fit the data through entire porosity range (magenta line in Figure 6.11). The identification of the stratigraphic cycles reveals that this model fits the I_P-porosity trend of carbonate-cemented sands deposited during the fining-upward cycles only.

The stiff-sand model (Gal et al., 1998) overpredicts the I_P-porosity trend of the carbonate-cemented sand (green line in Figure 6.11). This model can be modified to fit the data if we lower critical porosity from 40 % to 15 %. We call this the modified stiff-sand model in this paper (blue line in Figure 6.11).

The constant cement model (Avseth et al., 2000) with 1% constant cement fit the I_P-porosity trend in the data reasonably well (red line in Figure 6.11). However, the constant cement model assumes that impedance increases due to poor sorting while the cement volume remains constant. This assumption is not valid for carbonate-cemented sandstones from our study area; we have demonstrated earlier that sorting as well as cement volume vary considerably in a small depth interval (<100 meter), and it is not sorting but cement volume that controls P-impedance. Therefore, although the constant cement model reasonably predicts the I_P-porosity trend, this model appears to fit the data for the wrong sedimentological reasons.

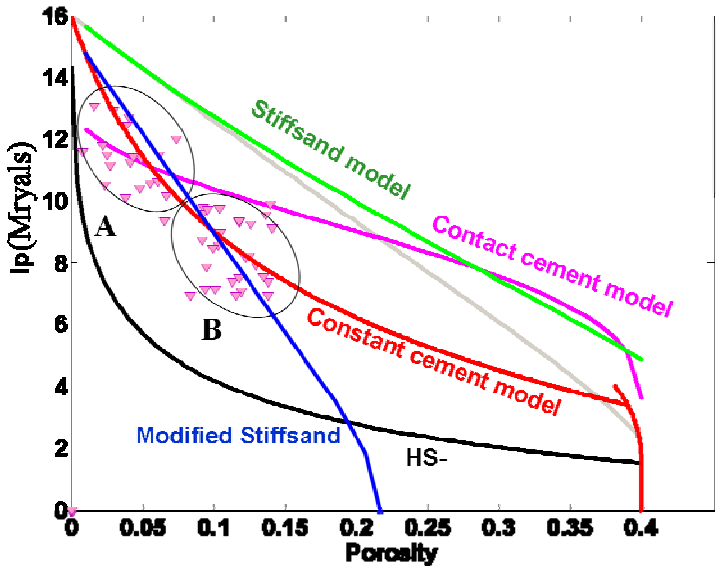

Figure 6.11: Comparisons of P-impedance (I_P) and porosity of carbonate-cemented sandstone with those predicted by existing granular-medium models for cemented sandstones. The clusters A and B represent data from the fining-upward cycles and coarsening-upward cycles, respectively. The contact cement model (magenta line) does not fit the data from cluster B. The constant cement model with 1% constant cement (red line) fits both the clusters A and B, but it violates variation in carbonate cement volume exhibited by these sandstones. The stiff-sand model (green line) overpredicts I_P. In order to fit data using the stiff-sand model, one has to assume unrealistically low critical-porosity (15%). This prediction is labeled as the Modified Stiffsand (blue line).

6.5.2 Inclusion Models

The granular-medium models described earlier are mostly applicable for medium-high porosity sands. Inclusion based models, such as the differential effective medium (DEM) models are valid for low porosity rocks, and might be appropriate for these low porosity carbonate-cemented sandstones. The predictions of I_P-porosity trends using the modified DEM model (Mukerji et al., 1995) with 40% percolation porosity are shown in Figure 6.12. The effective moduli at the mineral end-points are computed by adding dry pores in the background matrix, followed by Gassmann fluid substitution (Gassmann, 1951). The minerals in background matrix are constrained by sequence stratigraphic interpretations. For example, we consider high carbonate cement volume (40% calcite and 60% quartz) in the fining-upward cycles, and low cement volume (2% calcite, 20% clay and 78% quartz) in the coarsening-upward cycles. Such a modeling approach can geologically represent the carbonate diagenesis process associated with different

stratigraphic sequences. The model for the fining-upward cycles is valid in the lower porosity regime (0-8%), and the model for the coarsening-upward cycles is valid in the higher porosity regime (9-15%). We require a higher aspect ratio to fit the mean clusters of data from the coarsening-upward cycles. This possibly indicates a stiffer and rounder pore shape due to dissolution.

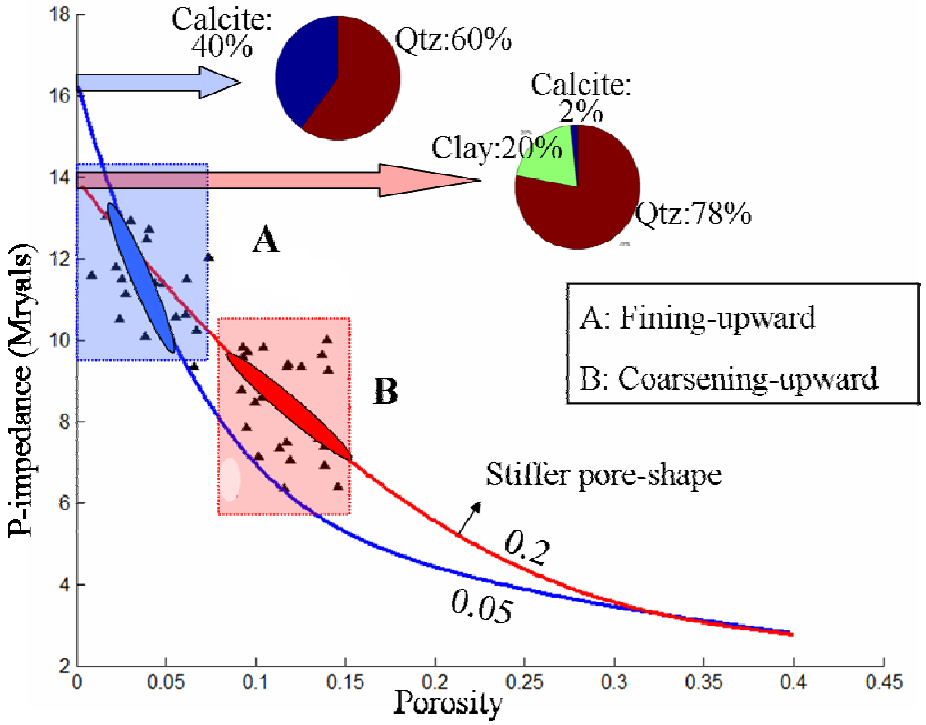

Figure 6.12: DEM modeling constrained by sequence stratigraphy. The P-impedance (I_P)-versus-porosity trends from the fining-upward and the coarsening-upward sequences are predicted using the Modified DEM model with mineral end-point as shown in figures. A higher aspect ratio is required to fit the mean cluster of data from coarsening-upward sequences, possibly indicating a rounded stiffer pore-shape due to dissolution.

The rock physics models, calibrated with well data, can be useful to interpret seismic impedance in terms of carbonate cement volume. For example, Figure 6.13 shows the map of inverted P-impedance and the map of carbonate cement volume at the base of a turbidite sequence. The P-impedances are obtained from model-based inversion of post-stack seismic volume in the Humpson Russel software, followed by the histogram matching with the well-log impedances. The inverted P-impedances are then used to

compute the carbonate cement volume using the modified DEM models, which were earlier calibrated with well data from the fining-upward and the coarsening-upward cycles.

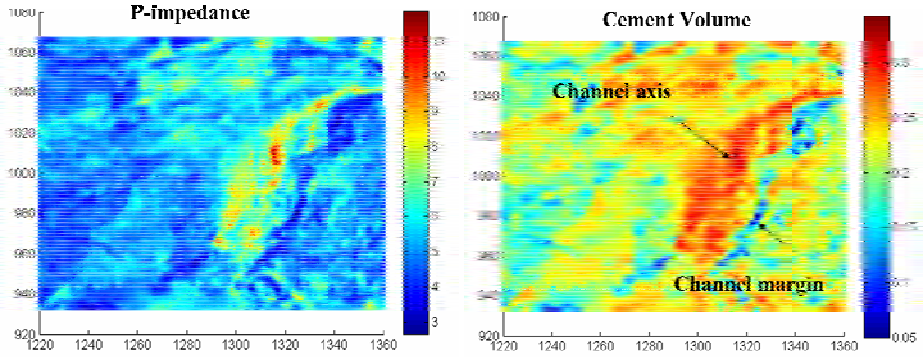

Figure 6.13: Quantify carbonate cement volume from seismic impedance. Left: P-impedance inverted from post-stack seismic volume. Right: carbonate cement volume quantified from the inverted P-impedance using modified DEM models calibrated with well data. Note the higher cement volume (~30%) in the channel axis in contrast to the lower cement volume (~5%) in the channel margin.

The map of carbonate cement volume (Figure 6.13) reveals important characteristics of carbonate diagenesis in channelized turbiditie environment. We observe a higher cement volume (~30%) in the channel axis compared to a lower cement volume (~5%) in the channel margin. Our observations are in agreement with other outcrop studies from channelized environments (e.g., Dutton et al., 2002; Dutton, 2008; Hall et al., 2004), where carbonate cements are preferentially more abundant in the sand-rich, coarser grained deposits at the axes of the sandstone bodies than in the finer grained deposits along the margins. Such spatial preference of carbonate cementation implies that the initially high-permeability architectural elements from the base of turbidite sequences tend to be associated with a higher cement volume, and therefore provides valuable predictability about fluid flow during production.

6.6 AVO response: modeling and comparing with data

We perform Monte Carlo AVO simulations with well log velocities and densities from the lithofacies containing uncemented sands and carbonate cemented sandstones,

and then compute intercept and gradient. Instead of a single point, it shows a scatter of data points (Figure 6.14). The reflection from uncemented sand to carbonate-cemented sandstones show distinct deviation from the background trend, and demonstrate class-I AVO response. The carbonate-cemented sandstones from the fining-upward cycles exhibit higher magnitudes of intercept and gradient. This agrees with the AVO modeling results using rock physics models (Figure 6.14), where the rock physics models were calibrated with well data from two distinct stratigraphic cycles. Our modeling quantitatively explains the increase in intercept and gradient with an increase in carbonate cement volume.

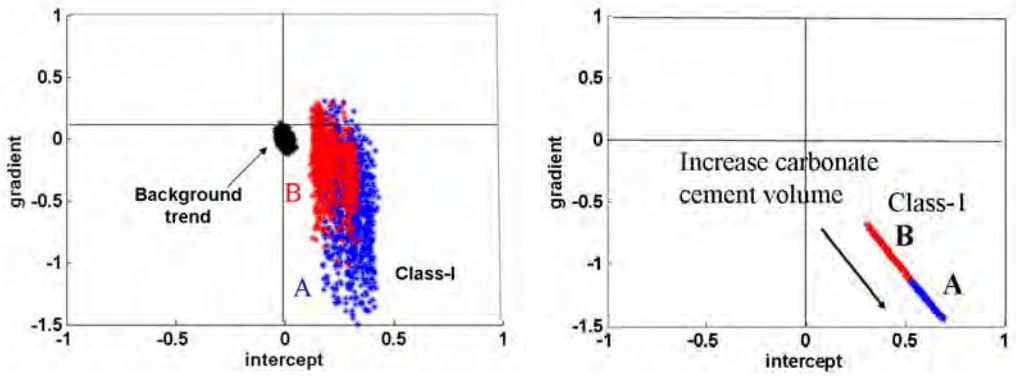

A=Fining-upward B=Coarsening-upward

Figure 6.14: Left: Monte Carlo AVO modeling using well logs. Right: Monte Carlo AVO modeling using rock physics models calibrated with well data from two distinct system tracts.

The modeled AVO responses are consistent with real seismic data (Figure 6.15). We follow the reflection event in three partial stack volumes (near offset stack: 0-18 degree, mid offset stack 18-35 degree, and far offset stack 35-45 degree). We observe class I response, where reflection amplitude is positive and decreases its magnitude at the far offset.

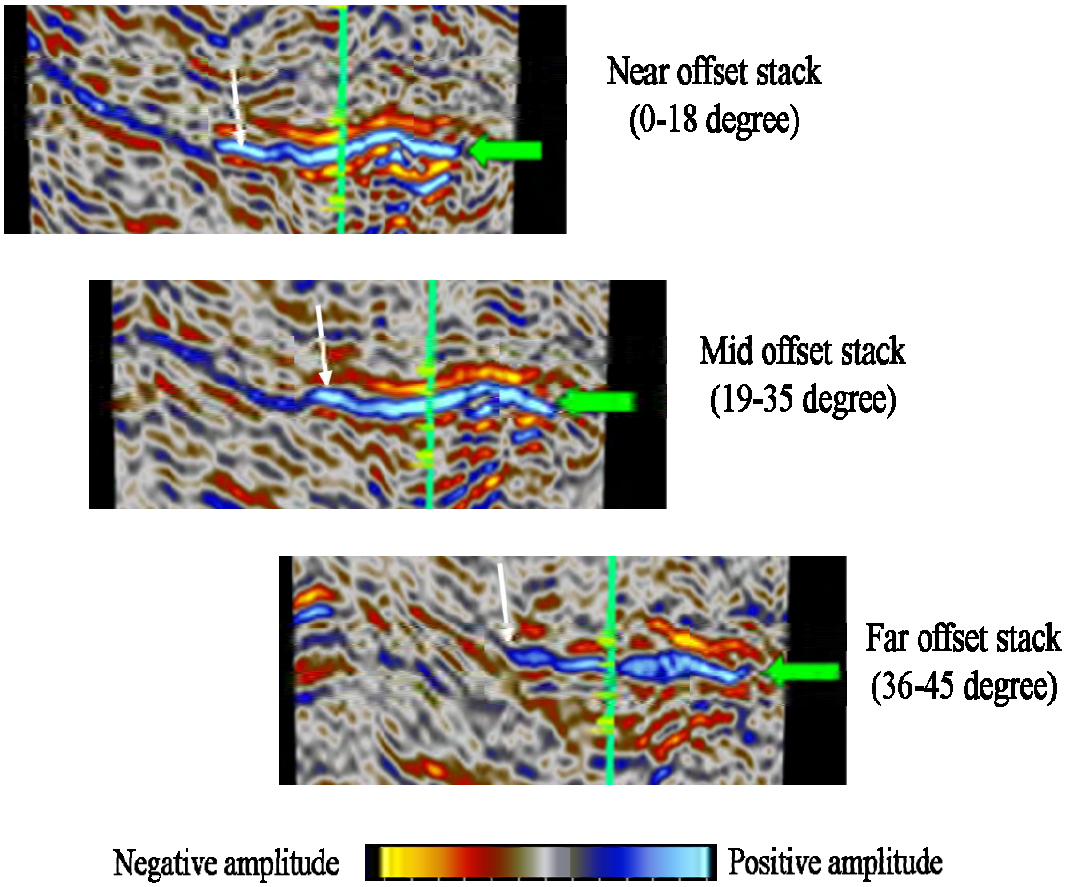

Figure 6.15: Seismic section from three partial stack volumes demonstrate the class-I AVO response for reflection from uncemented sands to carbonate cemented sandstones (marked by green arrow in figures). Top: near offset stack (0-18 degree), Middle: mid offset stack (18-35 degree), and Bottom: far offset stack (35-45 degree). The well is shown in the seismic sections. The reflection amplitude is positive and it dims with increasing offset. Note that the observed AVO response from the data confirms our modeling results.

6.7 Discussion

Our study shows that distinct clusters in the P-impedance- porosity crossplot can be linked with sequence stratigraphic cycles (Figure 6.9 and Figure 6.10). For example, porosity is selectively enhanced when the carbonate-cemented sandstones belong to the regressive or coarsening upward cycles. The dissolution of the margins of carbonate cements and neighboring grains are evident from thin-sections. Such dissolution and secondary porosity explains relatively lower P-impedance in these samples.

The development of secondary porosity can be the result of aluminosilicate and/or

carbonate dissolution (Surdam et al., 1984). Such dissolution significantly increases the mobility of aluminum, and the aluminum can be transported as an organic complex in carboxylic acid solutions. These carboxylic acid solutions have the capability of destroying carbonate grains and cements, and thereby enhancing porosity. The experiments by Surdam et al. (1984) also demonstrate that aluminimsilicate or carbonate dissolution is the natural consequence of the interaction of organic and inorganic reactions during progressive diagenesis. The degree of porosity enhancement depends on several factors, such as ratio of organic to inorganic matter, the initial composition of the organics, the sequences, rates and magnitude of diagenetic reactions, fluid flux, and sand/shale geometry.

In order to quantify the effects of carbonate cement volume on P-impedance, it is essential to identify an appropriate rock physics model. Different granular-medium models, such as the contact cement model, the constant cement model, and the stiff-sand model, have been shown useful for predicting effective elastic properties in quartz-cemented sandstones. However, these models fail to predict the effective elastic properties (e.g., P-impedance) in carbonate-cemented sandstones (Figure 6.11). Carbonate cements are sedimentologically more heterogeneous, and also show a very different morphology than silica cements. Cements can be placed in two major categories based on their morphology and spatial relationship to framework grains: rim cements and occluding cements. Rim cements, such as quartz overgrowths, exhibit a regular relationship to framework grain boundaries. Occluding cements, such as carbonate cements, fill pores with no preferred relationship to grain surfaces. Figure 6.16 shows a thin-section image of carbonate cement (occluding) from our study area in West Africa, and quartz cement (rim) from the North Sea studied by Avseth et al (2000).

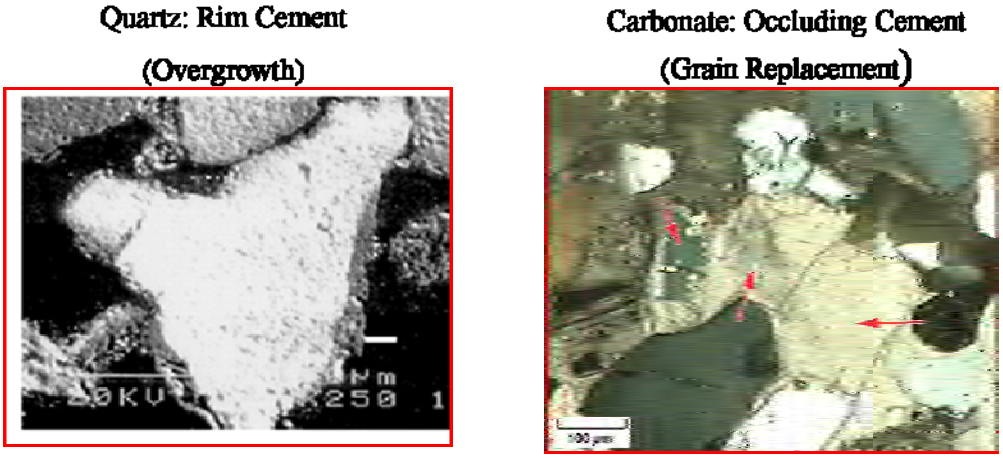

Figure 6.16: Two major categories of cement based on their spatial relationship to framework grains: quartz cements from the North Sea studied by Avseth (2000) (left), and carbonate cements from our study area in West Africa (right). The morphology of carbonate cement is distinct from siliciclastic cement. Carbonate cements occlude the pore network, and siliciclastic cements form coatings or rims around framework grains.

The differences in cement morphology as evident from the thin-sections may suggest why conventional rock physics models for quartz-overgrowth do not always fit data in carbonate-cemented sandstones. In addition, these granular-media models are only applicable for a very low cement volume (1-3%) and medium- to high-porosity sandstones. Our dataset shows a much lower porosity range (0 to 15 %) due to extensive carbonate cementation with cement volume ranging from 0 to 36%.

6.8 Conclusion

We demonstrate how carbonate cement volume can be quantitatively interpreted from P-impedance by integrating sequence stratigraphic cycles and appropriate rock physics models. We find that the carbonate-cemented sandstones, deposited in deep-water Equatorial Guinea from West Africa, are sedimentologically extremely heterogeneous. Their grain-size, sorting, mineralogy, clay-content and cement volume vary considerably within a depth interval of ~60 meter. However, P-impedance is primarily controlled by cement volume. The variation in cement volume can be associated with two different stratigraphic cycles: the fining-upward cycles and the coarsening-upward cycles.

Sediments associated with these two stratigraphic cycles reveal distinct signatures in the P-impedance-versus-porosity domain. The carbonate-cemented sandstones from the fining-upward cycles exhibit lower shaliness, lower porosity and higher P-impedance. In contrast, those from the coarsening-upward cycles exhibit higher shaliness, higher porosity and lower P-impedance. This establishes a link between the sequence stratigraphic cycles and P-impedance in carbonate-cemented sandstones.

The carbonate cements differ from siliciclastic cements in terms of cement morphology and sedimentological heterogeneity. This poses a challenge to apply common rock physics models for quartz-cemented sandstones to predict I_P -versus-porosity trends for the carbonate-cemented sandstones. We have demonstrated that the modified DEM model constrained by stratigraphic interpretations can be useful for predicting P-impedance -versus- porosity trends and AVO signatures. Our results suggest that combining stratigraphic cycles and rock physics models can be useful to quantify reservoir quality associated with carbonate cementation and subsequent dissolution from seismic impedance.

6.9 Acknowledgements

This work was supported by the Stanford Rock Physics and Borehole Geophysics project and DOE contract DE-FC26-04NT15506. We acknowledge Hess Corporation for providing the data, and thank Steve Graham, Don Lowe, Steve Uchytil, Jim Hewlett and Tiziana Vanorio for valuable discussions.

6.10 References

Avseth, P., 2000, Combining rock physics and sedimentology for seismic reservoir characterization in North Sea turbidite systems: Ph.D. thesis, Stanford University.

Avseth, P., T. Mukerji, and G. Mavko, 2005, Quantitative Seismic Interpretation: Applying Rock Physics Tools to Reduce Interpretation Risk: Cambridge University Press.

Berner, R.A., 1980, Early Diagenesis: A Theoretical Approach: Princeton University Press.

Berryman, J.G., 1995, Mixture Theories for Rock Properties: A handbook of physical constants, T.J. Athrens,ed. American Geophysical Union, Washington, D.C., 205-228.

Bjørkum, P. A., and O. Walderhaug, 1990, Geometrical arrangement of calcite cementation within shallow marine sandstones: Earth-Science Reviews, 29, 145–161.

Carvalho, M.V.F., L.F. De Ros, N.S. Gomes, 1995, Carbonate cementation patterns and diagenetic reservoir facies in the Campos Basin Cretaceous turbidites, offshore eastern Brazil: Marine and Petroleum Geology, 12, 741–758.

Dutta, T., T. Mukerji, and G. Mavko, 2007, Quantifying spatial trend of sediment parameters in channelized turbidite, West Africa: SEG Expanded Abstracts, 26, 1674-1679.

Dutton, S.P., D.W. Christopher., B.J. Willis., D. Novakovic., 2002, Calcite cement distribution and its effect on fluid flow in a deltaic sandstone, Frontier Formation, Wyoming: AAPG Bulletin, 86, 2007-2021.

Dutton, S.P., 2008, Calcite cement in Permian deep-water sandstones, Delaware Basin, west Texas: Origin, distribution, and effect on reservoir properties: AAPG Bulletin, 92, 765-787.

Dvorkin, J. and A. Nur, 1996, Elasticity of high-porosity sandstones: Theory for two North Sea datasets: Geophysics, 61, 1363-1370.

Folk, R., 1964, A review of grain-size parameters: Sedimentology, 6, 73-93.

Folk. R.L., and W.C. Ward, 1957, Brazos river bar, a study in the significance on grain-size parameters: Journal of sedimentary petrology, 27, 3-27.

Flórez-Niño, J.M, 2005, Integrating geology, rock physics, and seismology for reservoir quality prediction: Ph.D. thesis, Stanford University.

Gal, D., J. Dvorkin, and A. Nur, 1998, A Physical Model for Porosity Reduction in Sandstones: Geophysics, 63, 454-459.

Gassmann, F., 1951, Uber die elastizitat poroser medien: Veirteljahrsschrift der Naturforschenden Gesellschaft, 96, 1-23.

Giles, M. R., 1997, Diagenesis: a quantitative perspective: Boston, Kluwer Academic Publishers.

Greenberg, M.L., and J.P. Castagna, 1992, Shear-wave velocity estimation in porous rocks: Theoretical formulation, preliminary verification and application: Geophysical Prospecting, 40, 195-209.

Hall, J.S., P. Mozley., J.M. Davis., N.D. Roy., Environments of formation and controls on spatial distribution of calcite cementation in Plio-Pleistocene fluvial deposits, New Mexico, USA : Journal of Sedimentary Research, 74, 643-653.

Han, D., A. Nur, and D. Morgan, 1986, Effects of porosity and clay content on wave velocities in sandstones: Geophysics, 51, 2093-2107.

Inman, D.L., 1952, Measures of describing the size distribution of sediments: Journal of sedimentary petrology, 22, 125-145.

Kantorowicz, J. D., I. D. Bryant, and J. M. Dawans, 1987, Controls on the permeability and distribution of carbonate cements in Jurassic sandstones: Bridport Sands, southern England, and Viking Group, Troll field, Norway, in J. D. Marshall, ed., Diagenesis of sedimentary sequences: Oxford, Blackwell, 103–118.

Ketzer, J.M., S. Morad, R. Evans, and I.S. Al-Aasm, 2002, Distribution of diagenetic alterations in fluvial, deltaic, and shallow marine sandstones within a sequence stratigraphic framework: Evidence from the Mullaghmore Formation (Carboniferous), NW Ireland: Journal of Sedimentary Research, 72, 760-774.

Ketzer, J.M., S. Morad, A. Amorosi, 2003, Predictive clay cementation in a sequence stratigraphy framework. In: Worden, R., S. Morad, (Eds.), Clay Cementation in Sandstones, International Association of Sedimentologists Special Publication, 34, 42–59.

Ketzer, J.M. and S. Morad, 2006. Predictive distribution of shallow marine, low-porosity (pseudomatrix-rich) sandstones in a sequence stratigraphic framework--example from the Ferron sandstone, Upper Cretaceous, USA: Marine and Petroleum Geology, 23, 29-36.

Loutit, T.S., J. Hardenbol, P.R. Vail, G.R. Baum, 1988, Condensed sections: the key to age determination and correlation of continental margin sequences. In: Wilgus, C.K., Hastings, B.S., Kendall, C.G.St.C., Posamentier, H.W., Ross, C.A., Van Wagoner, J.C. (Eds.), Sea-Level Changes: An Integrated Approach. Soc. Econ. Paleontol. Mineral., Spec. Publ. 42, 183–213.

Lowe, D.R., 2004, Report on core logging, lithofacies, and basic sedimentology of Equitoral Guinea: Hess internatal report.

Mansurbeg, H., Mohamed A.K. El-ghali, S. Morad, P. Plink-Bjorklund, 2006, The impact of meteoric water on the diagenetic alterations in deep-water, marine siliciclastic turbidites: Journal of Geochemical Exploration, 89, 254-258.

Mansurbeg, H., S. Morad, A. Salem, R. Marfil, M.A.K. El-ghali, J.P. Nystuen, M.A. Caja, A. Amorosi, D. Garcia, A. La Iglesia, 2008, Diagenesis and reservoir quality evolution of palaeocene deep-water, marine sandstones, the Shetland-Faroes Basin, British continental shelf: Marine and Petroleum Geology, 25, Issue 6, 514-543.

Mavko, G., T. Mukerji and J. Dvorkin, 1998, The Rock Physics Handbook, tools for seismic analysis in porous media: Cambridge University press, New York, 329.

McBride, E. F., K. L. Milliken, W. Cavazza, U. Cibin, D. Fontana, M.D. Picard, and G.G. Zuffa, 1995, Heterogeneous distribution of calcite cement at the outcrop scale in Tertiary sandstones, northern Apennines, Italy: AAPG Bulletin, 79, 1044–1063.

McCammon, R.B., 1962, Efficiencies of percentile measures for describing the mean size and sorting of sedimentary particles: J. Geol., 70, 453-465.

Morad, S., 1998, Carbonate cementation in sandstones: distribution patterns and geochemical evolution, in S. Morad, ed., Carbonate cementation in sandstones: International Association of Sedimentologists Special Publication, 26, 1–26.

Morad, S., J.M. Ketzer, F. De Ros, 2000, Spatial and temporal distribution of diagenetic alterations in siliciclastic rocks: implications for mass transfer in sedimentary basins: Sedimentology, 47, 95–120.

Mukerji T., J.G. Berryman, G. Mavko, and P.A Berge, 1995, Differential effective medium modeling of rock elastic moduli with critical porosity constraints: Geophysical Research Letters, 22, 555–558.

Otto, G.H., 1939, A modified logarithmic probability graph for the interpretation of mechanical analyses of sediments: Journal of sedimentary petrology, 9, 62-76.

Pittman, E. D., and R. E. Larese, 1991, Compaction of Lithic Sands: Experimental Results and Applications: AAPG Bulletin, 75, 1279- 1299.

Saigal, G. C., and K. Bjørlykke, 1987, Carbonate cements in clastic reservoir rocks from offshore Norway—relationships between isotopic composition, textural development and burial depth, in J. D. Marshall, ed., Diagenesis of sedimentary sequences: Oxford, Blackwell, 313–324.

Surdam, R.C., S.W. Boese, and L.J. Crossey, 1984, The chemistry of secondary porosity, in McDonald, D.A., and R.C. Surdam, eds., Clastic Diagenesis: AAPG Memoir, 37, 127-150.

Taylor, K.G., R.L. Gawthorpe, and J.C. Vanwagoner, 1995, Stratigraphic Control on Laterally Persistent Cementation, Book-Cliffs, Utah: Journal of the Geological Society, 152, 225-228.

Taylor, K.G., R.L. Gawthorpe, C.D. Curtis, J.D. Marshall, and D.N. Awwiller, 2000, Carbonate Cementation in a Sequence-Stratigraphic Framework: Upper Cretaceous Sandstones, Book Cliffs, Utah-Colorado: Journal of sedimentary research, 70, 360-372.

Walderhaug, O., and P.A. Bjorkum, 1992, Effect of Meteoric Water-Flow on Calcite Cementation in the Middle Jurassic Oseberg Formation, Well 30/3-2, Veslefrikk Field, Norwegian North-Sea: Marine and Petroleum Geology, 9, 308-318.

Chapter 7
Acoustic Velocities Depend on Time-Temperature Index: Hypothesis Testing

"The mere formulation of a problem is far more essential than its solution, which may be merely a matter of mathematical or experimental skills. To raise new questions, new possibilities, to regard old problems from a new angle require creative imagination and marks real advances in science"

-- Albert Einstein

7.1 Abstract

We test the hypothesis that acoustic velocities of rock depend on time and temperature index (TTI). Our study is motivated by the observations that temperature and time play significant roles in controlling the rock and fluid properties in many sedimentary basins. TTI, an important organic thermal maturity indicator, is directly linked with oil and gas generation. However, existing rock physics models (theoretical,

empirical, and numerical) do not relate seismic velocities and time-temperature index (TTI). In this chapter, we investigate whether TTI can be empirically related to seismic velocities. For this, we perform basin and petroleum system modeling at a well location in a deep-water petroleum system at Rio Muni Basin, West Africa. The TTI obtained from numerical modeling are then compared with velocities measured at the same well location. We find that both V_P and V_S increase exponentially with TTI. The results presented in this chapter can be useful to predict TTI, and thereby thermal maturity, from observed velocities at the similar depositional settings.

7.2 Introduction

Time-temperature index (TTI) serves as an indicator of thermal maturity (Lopatin 1971; Waples 1980). Our motivation to investigate the relation between TTI and acoustic velocities originates from several studies depicting that reservoir qualities (e.g., porosity and permeability) depend on temperature and time (e.g., Bjørkum, 1996; Ehrenberg et al., 1989; Nadeau et al., 2002).

Magoon (2004) have shown that thermal maturation of organic matter is primarily controlled by temperature and time, rather than by pressure. Overpressure in many sedimentary basins typically starts developing at about 60^o C and reaches near-lithostatic fracture pressures at about 120^o C (Ehrenberg, 1993). In addition, chemical compaction is controlled by temperature and time. For example, quartz cement volume increases with temperature (Bjørkum, 1996; Bjørkum et al., 1988). The transformation of smectite to illite is a temperature-sensitive reaction. The pervasive fibrous illitization leads to dramatic reduction of permeability beyond ~120^o C (Ehrenberg et al., 1989; Nadeau et al., 2002). Moreover, it is generally accepted that effective petroleum biodegradation over geological timescales generally occurs in reservoirs with temperatures below 80° C (Wilhelms, 2001). The rock subjected to temperature higher than ~80^o C is usually sterilized and prevents biodegradation even when uplifted in lower temperature regime (Wilhelms, 2001). Although there are reported exceptions of ideal temperature windows, identification of such thermal windows may be useful to predict reservoir quality in

frontier basins.

Existing rock physics models (theoretical, empirical, and numerical) do not provide any explicit relationship between seismic velocities and TTI. TTI can be correlated with vitrinite reflectance, another indicator of thermal maturity, as demonstrated by several researchers (Waples, 1980; Goff, 1983; Horvath et al., 1986; Yukler, 1987; Baric et al., 1991). The focus of the present chapter is to test our hypothesis that acoustic velocities of rock depend on TTI. We perform basin and petroleum system modeling at a well location in a deep-water petroleum system at Rio Muni Basin, West Africa. The TTI obtained from basin modeling are then compared with velocities measured at the same well location. Our study shows that both V_P and V_S increase exponentially with increasing TTI.

7.3 Definition of Time-Temperature Index (TTI)

The relationship between temperature and the rate of chemical reactions is given by Arrhenius equation (equation 7.1):

$$K = A\exp(-E_a/RT) \tag{7.1}$$

where K is the reaction rate, A is a constant called the frequency factor, E_a is the activation energy, R is the Universal Gas Constant, and T is the absolute temperature in degree Kelvin. The Arrhenius equation suggests that reaction rates should increase exponentially with temperature, so that a 10^o C rise in temperature causes the reaction rate to double (Allen and Allen, 1996).

Lopatin (1971) borrowed the above assumption about reaction rate from the Arrhenius equation, and developed the time-temperature index (TTI) as an indicator of thermal maturity of rock. The Lopatin method involves superimposing a 10^o C isotherm grid on a burial history curve. The amount of time a rock unit resides on each 10^o C interval is then used to calculate interval TTI. Finally, the interval TTI is cumulatively summed along its burial history curve to obtain the TTI of present day. The Lopatin approach was evaluated by Waples (1980), who changed the original TTI values for

different stages of oil generation using an empirical correlation with vitrinite reflectance. The Lopatin and Waples modification has since been widely used for predicting thermal maturity of petroleum source rocks. The expression of TTI according to Lopatin and Waples is as follows:

$$TTI = \sum_{n_{\min}}^{n_{\max}} r^n \Delta t^n \tag{7.2}$$

where, Δt^n is the time interval (in Ma) that the rock spent in the nth temperature interval, $n_{\min}$ and $n_{\max}$ are the minimum and maximum values of the index n, and r is an arbitrary number describing the exponential dependence. The model assumes that the maturation rate is exponential in temperature and linear in time for a particular interval of temperature and time—both are reasonable assumptions (Palumbo et al., 1999). After empirical calibration tests, the optimum value for the factor r is found on borehole data to be r=2 (Waples 1980). TTI values calculated from Lopatin-Waples reconstructions commonly agree with other maturation parameters commonly used by petroleum geochemists, such as vitrinite reflectance (Vetö and Dövényi, 1986).

The primary assumption in the Lopatin-Waples method is that reaction rate doubles for every 10^o C rise in temperature. However, this assumption is not valid for the entire temperature range. At higher temperature, the reaction rate slows down and does not double for 10^o C temperature rise (Robert, 1988). Therefore, Lopatin-Waple method tends to overestimate thermal maturity at higher temperature.

7.4 Time-temperature index (TTI) and reservoir quality

Reservoir qualities (porosity and permeability) are controlled by temperature and time along with other parameters, such as, effective stress, mineralogy, sedimentary texture (sorting, angularity, grain-roundedness, and grain-sphericity), clay content, position of clay in pore-network, and diagenetic cements (Allen and Allen, 1996). In this section, we show specific examples from literatures where temperature and time play significant

roles in controlling the rock and fluid properties.

1. Thermal maturity of organic matter

It is widely agreed that thermal maturation of organic matter is primarily controlled by temperature and time, rather than by pressure (Magoon, 2004; Allen and Allen, 2006). This leads to formation of well-defined oil and gas windows in a sedimentary basin. Worldwide siliciclastic basins can be modeled using an idealized thermal window in which about 90 percent of the world's oil and gas resources are found between the 60^{o} and 120^{o} C isotherms (Bjørkum, 1996). TTI is an important thermal maturity indicator that can be correlated with oil and gas windows. Important TTI values are: 15-onset of oil generation; 75-peak oil generation; 160-end oil generation; 160-onset of wet gas generation; 1500- end wet gas generation; 1500- onset of dry gas generation; 65,000- end dry gas (Allen and Allen, 2006).

2. Overpressure in different basins

In many sedimentary basins, overpressure in sealed pressure compartments starts at different depths. However, the temperatures where they occur are very similar. Ehrenberg (1993) showed that overpressure typically starts developing at about 60^{o} C and reaches near-lithostatic fracture pressures at about 120^{o} C in Mid-Norwegian shelf.

3. Chemical compaction

Chemical compaction (precipitation of new materials in pore network) strengthens the rock framework and reduces porosity and permeability of rock. Contrary to mechanical compaction, chemical compaction is controlled by temperature and time rather than by pressure (Bjørkum, 1996; Leder and Park, 1986). At temperatures below about 70^{o} C, mechanical compaction is the dominant factor for porosity loss, and porosity loss can be modeled as a function of effective pressure. At temperatures above about 60^{o} to 80^{o} C, porosity loss can be modeled as a function of thermo-chemical reactions. For example, Bjørkum et al. (1988) show that quartz cement volume increases from zero to 20% with increase in temperature from 70^{o} to 170^{o} C, and the corresponding porosity in sandstones

decreases from 22% to 2% due to quartz cementation. Furthermore, several studies have shown that temperature acts as one of the major controlling factors for pressure solution (e.g., Bjørkum, 1996; Bjørlykke et al., 2009; Houseknecht, 1984; Renard et al., 1997).

4. Smectite to illite transformation

The transformation of smectite to illite is a temperature sensitive reaction. The pervasive fibrous illitization leads to dramatic reduction of permeability beyond ~120^{o} C (Ehrenberg and Nadeau, 1989; Nadeau et al., 2002). Thus the shales affected by illitization are prone to overpressure development, and the illitization can be correlated with the thermal window from 120^{o} to 150^{o} C (Ehrenberg and Nadeau, 1989; Ehrenberg, 1990).

5. Biodegradation

Biodegradation is usually a common phenomenon in oil reservoirs, and it increases with temperature. It is generally accepted that effective petroleum biodegradation over geological timescales occurs in reservoirs with temperatures below 80° C (Connan, 1984; Wilhelms, 2001). The rocks subjected to temperature higher than ~80° C are usually sterilized by heating and prevents biodegradation even when uplifted into lower temperature regimes (Wilhelms, 2001).

The above examples suggest that temperature and time can play significant roles predicting rock and fluid properties. Although there are reported exceptions of ideal thermal windows in these examples, identification of such thermal windows may be useful to predict thermal maturity and reservoir quality in frontier basins. The simulation of thermal history of a sedimentary basin is discussed in the next section.

7.5 Petroleum System Modeling: A Brief overview

Petroleum system modeling reproduces the thermal history of a sedimentary basin. They are useful to characterize petroleum systems, including extent and timing of petroleum generation, migration and accumulation (Magoon and Dow, 1994). Figure 7.1 shows various processes involved in petroleum system modeling. The basin processes are

modeled from the past to the present using inferred starting conditions (Welte et al., 1997). The key input parameters in 1D basin modeling are present thickness and age of rock units at the well, information about hiatus (eroded thickness and erosion age), lithologies and physical properties of rock units, and petroleum system essential elements (source rock, reservoir rock, overburden rock and seal rock). The boundary conditions are: present and past water depths, basal heat flow and sediment-water interface temperatures. Geochemical data on source rock, such as the type and amount of organic matter and the kinetics for the conversion of kerogen to petroleum are also required.

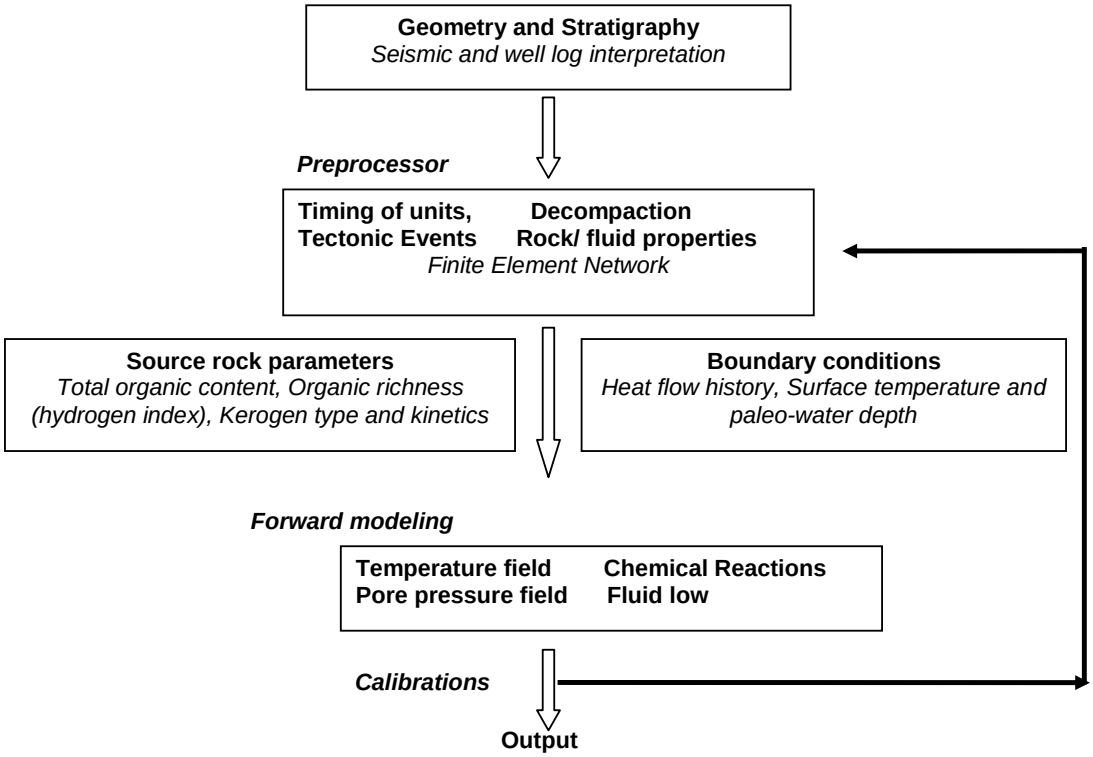

Figure 7.1: A schematic workflow for numerical modeling of the geohistory of petroleum systems. Petroleum system modeling refers to numerical modeling of the generation, migration, and accumulation of petroleum through geologic time.

The processes in a petroleum system (i.e., generation, migration and accumulation of petroleum) are simulated through discrete time steps. Each time step in a petroleum

system model consists of a framework of calculations that are required to generate the input for the next simulation time step. For example, the calculated temperature at each time step during burial of a source rock is required to determine the volumes of generated hydrocarbon. The time and space dependent differential transport equations needed for modeling and the finite element methods used for their solutions can be found in the literature (e.g., Hantschel and Kauerauf, 2009).

The typical output for each time event includes rock unit thickness after decompaction, porosity, pressure, temperature and thermal maturity at different depths, generated volume of petroleum, expulsion efficiency, migration pathways and accumulated volume of petroleum.

7.6 Petroleum System Modeling: Example from Rio Muni basin

7.6.1 Overview of Rio Muni basin

We use the Lopatin-Waples (Lopatin 1971; Waples 1980) method implemented in the Petromod software to compute TTI as an output of 1D modeling of the Rio Muni basin, West Africa. The Rio Muni basin is one of a series of Early to middle Cretaceous rift segments that underlie the Atlantic coast of West Africa (Dailly et al., 2002). The basin shows strong similarities in stratigraphy and play possibilities with the adjacent hydrocarbon basins of West Africa and, in particular, to northern Gabon (Dailly et al., 2001 and 2002). The Sergipe-Alagoas basin of Brazil provides a direct analog to the Rio Muni basin which is located in a conjugate position on the opposite side of the Atlantic Ocean (Turner, 1995; Mohriak et al., 2000; Lawrence et al., 2002). According to Dailly et al. (2002), the deepening of the Rio Muni basin in the late Aptian-early Albian culminated in major transgression and deposition of an organic-rich mudstone succession. These facies range from lagoonal to marine and represent the main source rock interval for the basin. Following the onset of post-rift subsidence, the Albian and younger sequence were deformed. This deformation was associated with diapirism and folding in the base of slope area, creating minibasin topography. A series of channelized turbidites were developed in the mini-basins. The channels dominate the Upper

Cretaceous and constitute the main exploration target. Subsequent burial of the basin by a thick Tertiary section pushed the Albian source rock into the oil kitchen in the deep-water area where expulsion is interpreted to be active into the Recent. This is the overall setting for source rock and reservoir rock in the Rio Muni basin based on the study by Dailly et al. (2002).

7.6.2 Well log interpretation to identify chronostratigraphic units and lithofacies

We use well logs from the Rio Muni basin for 1D petroleum system modeling. The first task is to identify the chronostratigraphic units from the well-logs. We divide the entire petroleum system into 20 chronostratigraphic rock units. The depositional age of each rock unit is obtained from paleontological data. The interpretation of paleontological data is beyond the scope of our research, and we used information provided by Hess Corporation. The chronostratigraphic units are shown at the well (Figure 7.2). The top and the base of each chronostratigraphic unit are used to compute their present thickness at the well location.

Next, we identify the lithofacies from well log interpretation to assign lithology to each chronostratigraphic unit. We identify 7 different facies: shale, shaly-sand, shaly-silt, sandy-shale, sandy-silt, sandstone and cemented calcite. Different lithofacies are identified based on gamma ray, density, sonic and neutron logs. Table 7.1 summarizes the age, present thickness and generalized lithology at the well location. Each facies is characterized by an initial porosity which decreases exponentially with increase in effective stress. The initial porosity of shale, shaly-sand, shaly-silt, sandy-shale, sandy-silt, sandstone and cemented calcite are 65 %, 57%, 59%, 52%, 50%, 42 % and 5 % respectively. We consider an empirical porosity-depth trend (Sclater and Christie, 1980) to model porosity loss with depth. The original porosity, present-day thickness and porosity-depth curves are used to generate the decompacted thickness of each rock units. The decompacted thickness is obtained from the following mass-balance equation:

$$(1-\phi_N)T_N = (1-\phi_0)T_0 \tag{7.3}$$

where, ϕ_0 is the original porosity, ϕ_N is the porosity at any depth computed using ϕ_0 and porosity-depth curves, T_0 is the present-day thickness of rock units measured at the well location, and T_N is the decompacted thickness of the rock units.

We consider that each lithofacies has different thermal conductivity which decreases with increase in temperature. We used the default values of thermal conductivity provided in the Petromod software. For example, the thermal conductivity of sandstone facies in our model decreases from 3.12 W/M/K to 2.64 W/M/K for temperature rising from 20^o C to 100^o C. For the same temperature change, the thermal conductivity in shale decreases from 1.98 W/M/K to 1.91 W/M/K. The thermal conductivity is an important parameter in our modeling, since, the conductive heat flow is linearly proportional to thermal-conductivity and inversely proportional to geothermal gradient (Fourier's heat law for conduction). In the present modeling, we consider heatflow only due to static heat conduction, which is the major contributor to the total heat transfer in subsurface. Transient heat conduction, convection, and radiogenic heat generation are not considered in our model.

7.6.3 Identify essential petroleum system elements

There are four essential elements in a petroleum system: source rock, reservoir rock, seal rock, and overburden rock. In our study area, the source rock is of Albian age. The reservoir rock consists of turbidite sandstones. The top and base of turbidite reservoir are shown at the well (Figure 7.2). The sediment columns above source rock occur as overburden and contribute to the thermal maturity of source rock. The essential petroleum system elements in our modeling are tabulated in Table-7.1.

Table 7.1: Present thickness, age, lithology, and petroleum system element information for the chronostratigraphic units in our petroleum system model.

Age of Interval (Ma)	Depth (meter)			Deposition Age		Lithology	Petroleum System Elements
	Top	Base	Present thickness	From (Ma)	To (Ma)		
Sediment Surface			0				
10.5 to 0	0	560	560	10.5	0	Shale	Overburden
12.5 to 10.5	560	650	90	12.5	10.5	Shale	Overburden
16.5 to 12.5	650	650	0	16.5	12.5	Shale	Overburden
55 to 16.5	650	797	147	55	16.5	Shale	Overburden
T/K boundary	797	844	47	67	55	Shale	Overburden
71 to 67	844	862	18	71	67	Shale	Seal
75 to 71	862	986	124	75	71	ShaleSand	Reservoir
76 to 75	986	986	0	76	75	ShaleSilt	Reservoir
77.5 to 76	986	1011	25	77.5	76	SandShaly	Reservoir
78 to 77.5	1011	1075	64	78	77.5	SandSilty	Reservoir
79 to 78	1075	1108	33	79	78	Sandstone	Reservoir
79.5 to 79	1108	1315	207	79.5	79	Cemented calcite	Overburden
80 to 79.5	1315	1369	54	80	79.5	Shale	Seal
85 to 80	1369	1407	38	85	80	Sandstone	Reservoir
88.5 to 85	1407	1480	73	88.5	80	Cemented calcite	Overburden
90 to 88.5	1480	1514	34	90	88.5	Shale	Overburden
U. Albian	1514	1540	26	96.5	90	Shale	Source Rock
Aptian	1540	1570	30	107.5	96.5	Shale	Underburden

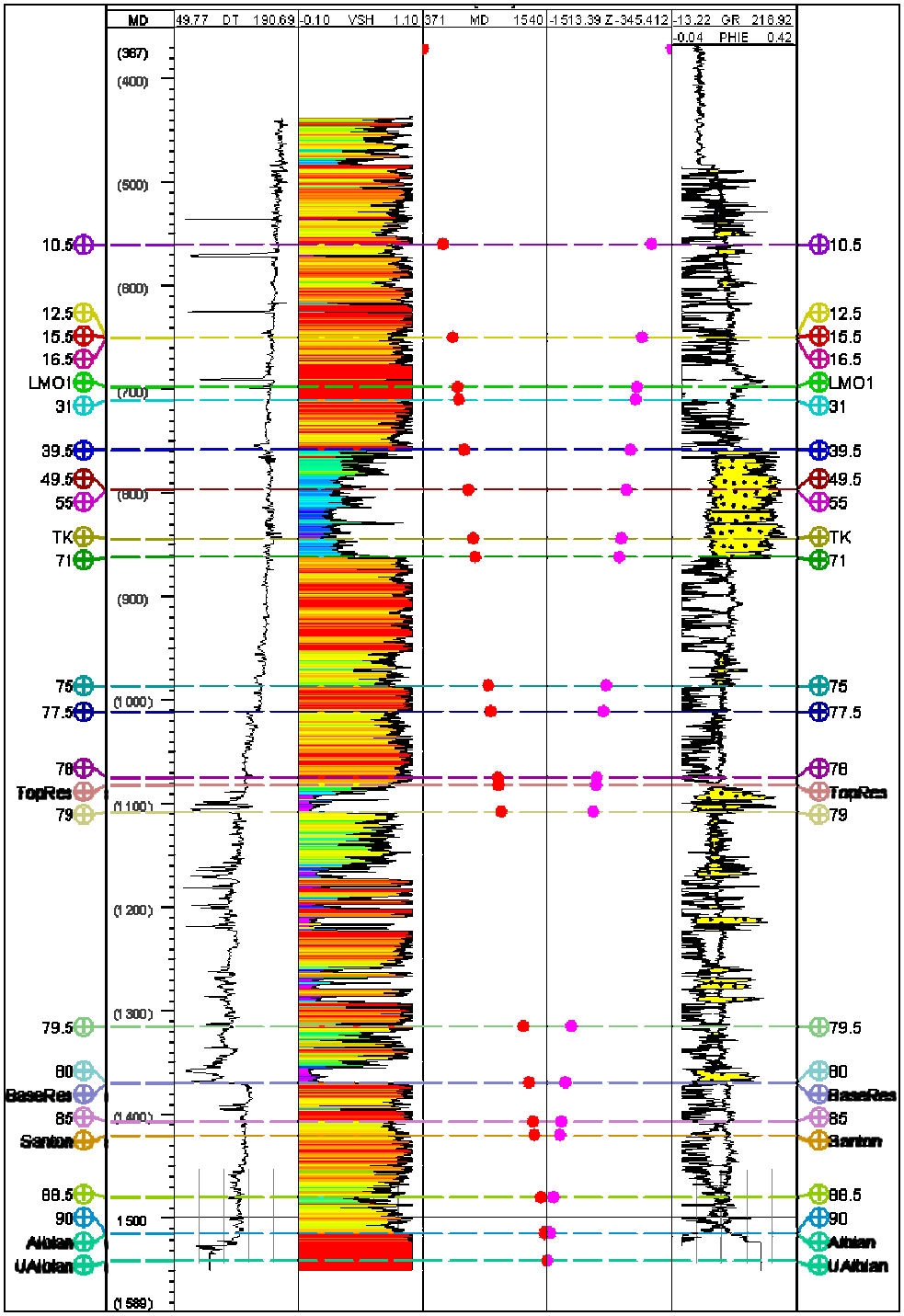

Figure 7.2: Well log showing age and thickness of layers. Top and base of reservoir are identified on the well. Source rock is of Albian age.

7.6.4 Specify source rock properties

The source rock properties are important parameters in modeling the thermal maturity of organic matter in a sedimentary basin. A source rock contains sufficient organic matter of suitable chemical composition to biogenically or thermally generate and expel petroleum (Magoon, 2004). The higher the TOC or concentration of carbon in organic matter, the richer is the source rock. Other important source rock parameter is hydrogen-index (HI) which is a measure of source rock quality. The higher the HI, the better is the source rock quality (Peters and Cassa, 1994). For example, HI greater than 600 (mgHC/g TOC) expel mostly oil (Type-1 organic matter), HI greater than 300 (mgHC/g TOC) and less than 600 expel mostly oil with some gas (Type-2 organic matter), HI between 200 and 300 expel some light oil but mostly gas (Type-3 organic matter), and HI between 50 and 200 is just natural gas (Type-4 organic matter). Both TOC and HI can be obtained from geochemical measurements. However, in the absence of such measurements, we estimate TOC from geophysical measurements (resistivity and sonic logs) and HI from an analog basin. In our numerical model, we borrow the HI from the Gabon basin in West Africa which has similar play structure with the Rio Muni basin (Dailly et al., 2002). We assign HI to be 600 in our modeling. The kinetics describe the rate of thermal decomposition of kerogen to petroleum and can be derived from empirical laboratory experiments or field observations (Pepper and Covri, 1995; Dieckmann, 2005). We use kinetics proposed by Behar et al., (1997) for Type-1 organic matter. The source rock properties used in our numerical modeling are shown in Table 7.2.

Table 7.2: Age, Present thickness, Total organic carbon, Hydrogen index and kinetics selected in the source rock of the Rio Muni basin, West Africa. The source rock parameters contribute to the thermal maturity of organic matter.

Age	**Thickness (meter)**	**Total organic carbon (wt %)**	**Hydrogen index (mgHC/g TOC)**	**Kinetics**
Albian	90	3	600	Behar et al (1997) for Type-1 organic matter

Compute total organic carbon (TOC) from Resistivity and Sonic logs

We use the following expressions given by Passey et al. (1990) to compute total organic carbon (TOC) from resistivity and sonic logs.

$$\Delta \log R = \log_{10}[\frac{R}{R_{ns}}] + k(S - S_{ns}) \tag{7.4}$$

where, Δlog R is curve separation, R is measured formation resistivity (ohmm), R_{ns} is resistivity of non-source shales (ohmm), S is sonic log reading (usec/ft), S_{ns} is sonic log reading in non-source shales (usec/ft), and K is a scale factor which is usually -0.02.

TOC is calculated using:

$$TOC = (\Delta \log R)10^{(2.297 - .1688 LOM)} \tag{7.5}$$

where, TOC is total organic carbon in weight percent, and LOM is the level of organic maturity. In practice, LOM is obtained from a variety of sample analyses (e.g., vitrinite reflectance, thermal alteration index), or from estimates of burial and thermal history. If LOM is incorrectly estimated, the absolute TOC values will be somewhat in error, but the vertical variability in TOC will be correctly represented (Passey et al., 1990).

The above ΔlogR technique (Passey et al., 1990) provides a practical method for calculating TOC from well logs. This is useful when geochemical measurements are not available. Passey's method employs the overlaying of a properly scaled sonic transit time curve on a resistivity curve (preferably from a deep reading tool). In water-saturated, organic-lean rocks, both the curves respond to variations in formation porosity and can be overlain. However, a separation between two curves occurs in organic-rich intervals resulting from two effects: the sonic curve responds primarily to the presence of low-density, low-velocity kerogen, while the resistivity curve primarily responds to the formation fluid. This separation, ΔlogR, is computed using equation 7.4. The TOC in organic-rich interval is next computed using equation 7.5.

In order to compute TOC in our study area, we first identify the organic-lean shale

interval. The well log responses in this interval are shown in Figure 7.3. The resistivity and sonic log readings at this non-source interval are then used to compute Δlog R using equation 7.4. Next, we identify the organic-rich Albian source rock interval (Figure 7.4) and compute TOC using equation 7.5 assuming LOM value to be 10 for Type-1 organic matter. The computed TOC of the source-rock is ~ 3.

The TOC computed from the well logs represent the TOC of the present-day. Ideally, we should reconstruct the TOC to obtain the values at the age when the source rock was deposited (Peters et al., 2005). In this chapter, we skip this step of TOC reconstruction due to insufficient geochemical measurements.

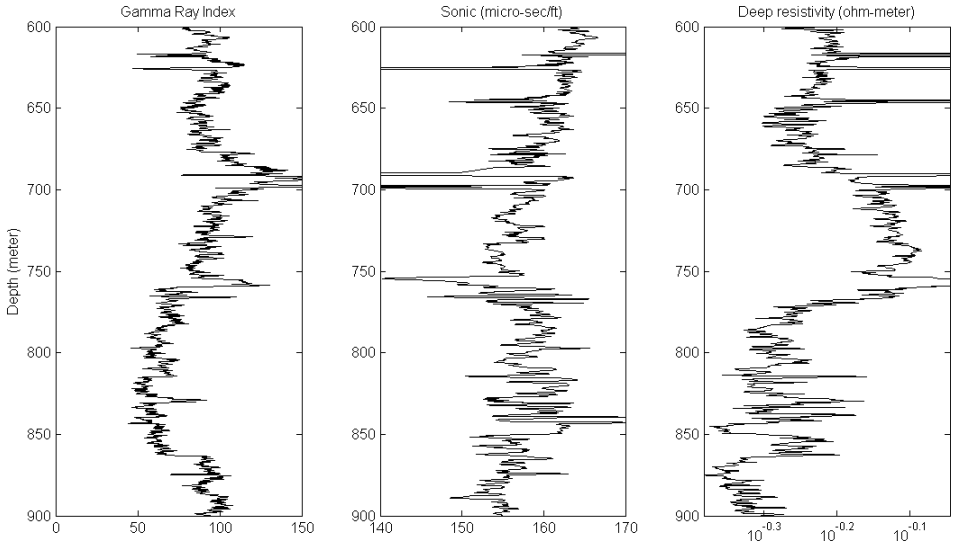

Figure 7.3: The well logs in the non-source shale interval. The sonic and resistivity log readings from this interval are used as inputs in equation 7.4 for computing Δlog R.

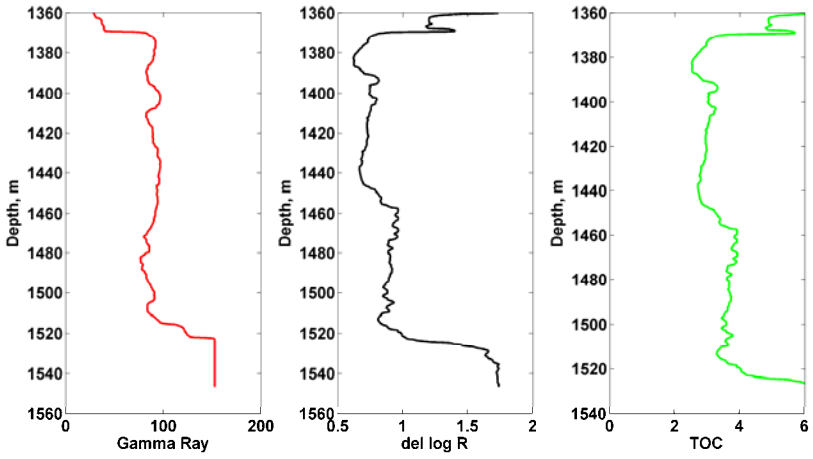

Figure 7.4: The gamma ray response, Δlog R, and TOC in organic-rich Albian source rock interval. TOC is computed in this shale interval using equation 7.5.

7.6.5 Boundary conditions

The three essential boundary conditions in petroleum system modeling are: (1) paleo-water depth (2) sea-water interface temperature and (3) heat flow throughout geologic time. We specify these boundary conditions throughout the geologic age from 120 Ma to present-day. The paleo-water depth is held constant at 70 meter in our model. This value represents the average depth, computed using the clinoform geometry and lateral progradation as observed from seismic data. The paleosurface to present-day surface temperatures are obtained using the Petromod software, where the relationships are based on an empirical study by Wrygala (1989). Figure 7.5 shows the global mean surface temperature variation as a function of latitude and time based on Wygrala (1989). The solid dark line in this figure represents the sediment-water interface temperature during deposition of sediments in the study area. In most of the sedimentary basins, the average heatflow values are 60-70 mW/m2; the heatflow is low (~50 mW/m2) in passive margin basins, and very high (~80 to ~100 mW/m2) in rift-basins and back-arc basins (Allen and Allen, 2006). Since, the Rio Muni basin is a rift basin, we consider a higher heatflow values. We consider the heatflow decreases from 90 to 75 mW/m2 over a geologic period from 120 Ma to present.

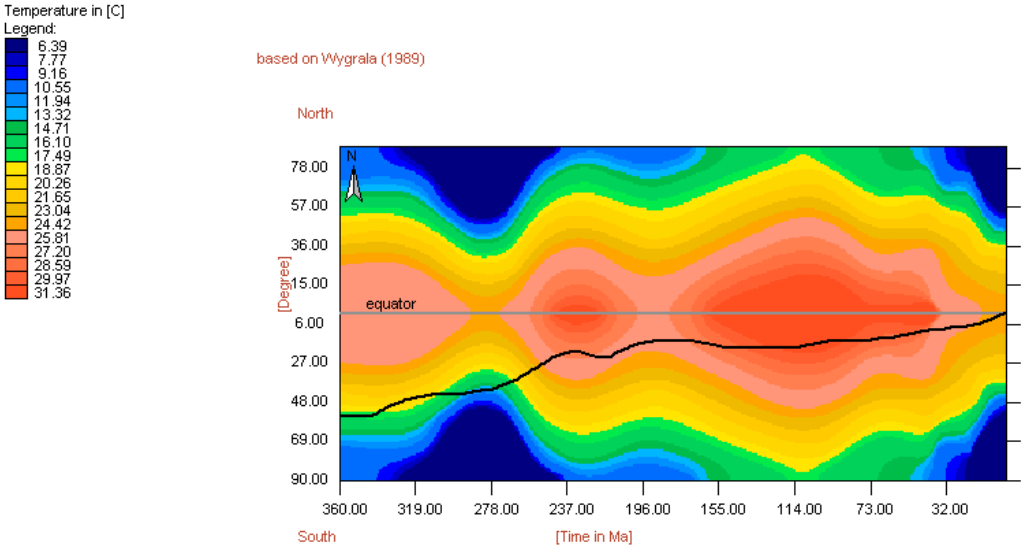

Figure 7.5: Global mean surface temperature variation is obtained as a function of latitude and time based on Wygrala (1989) in the Petromod software. The solid dark line depicts the sediment-water interface temperature in our model during deposition of sediments in the Rio Muni basin, West Africa.

7.6.6 Simulation results of thermal history

After specifying the input parameters and the boundary conditions, we simulate the thermal history of the basin using finite element modeling as implemented in the Petromod software. The progressive maturity of organic matter in the source rock interval is shown in Figure 7.6. Based on our modeling, the oil window and the gas window are predicted at ~10 Ma and ~5 Ma, respectively. Although the source rock was deposited in Albian, it generated hydrocarbon only ~10 Ma ago until the thick Tertiary overburden were deposited and pushed the source rock to the oil kitchen. The simulated temperature and TTI throughout the geologic time from 120 Ma to present are presented in Figure 7.7.

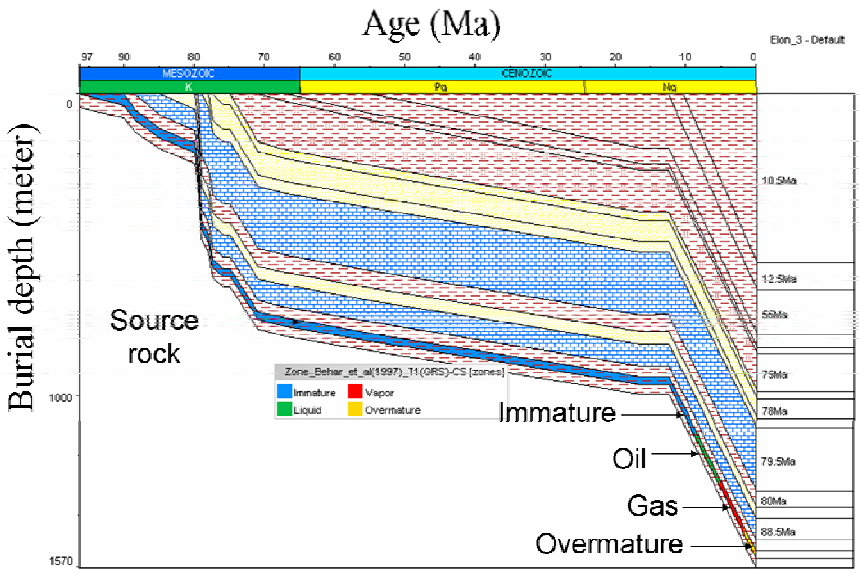

Figure 7.6: 1D burial history diagram at the well location. The source rock interval is highlighted by organic matter with different maturity and generated fluid: immature organic matter (blue), oil (green), gas (red), and overmature organic matter (yellow).

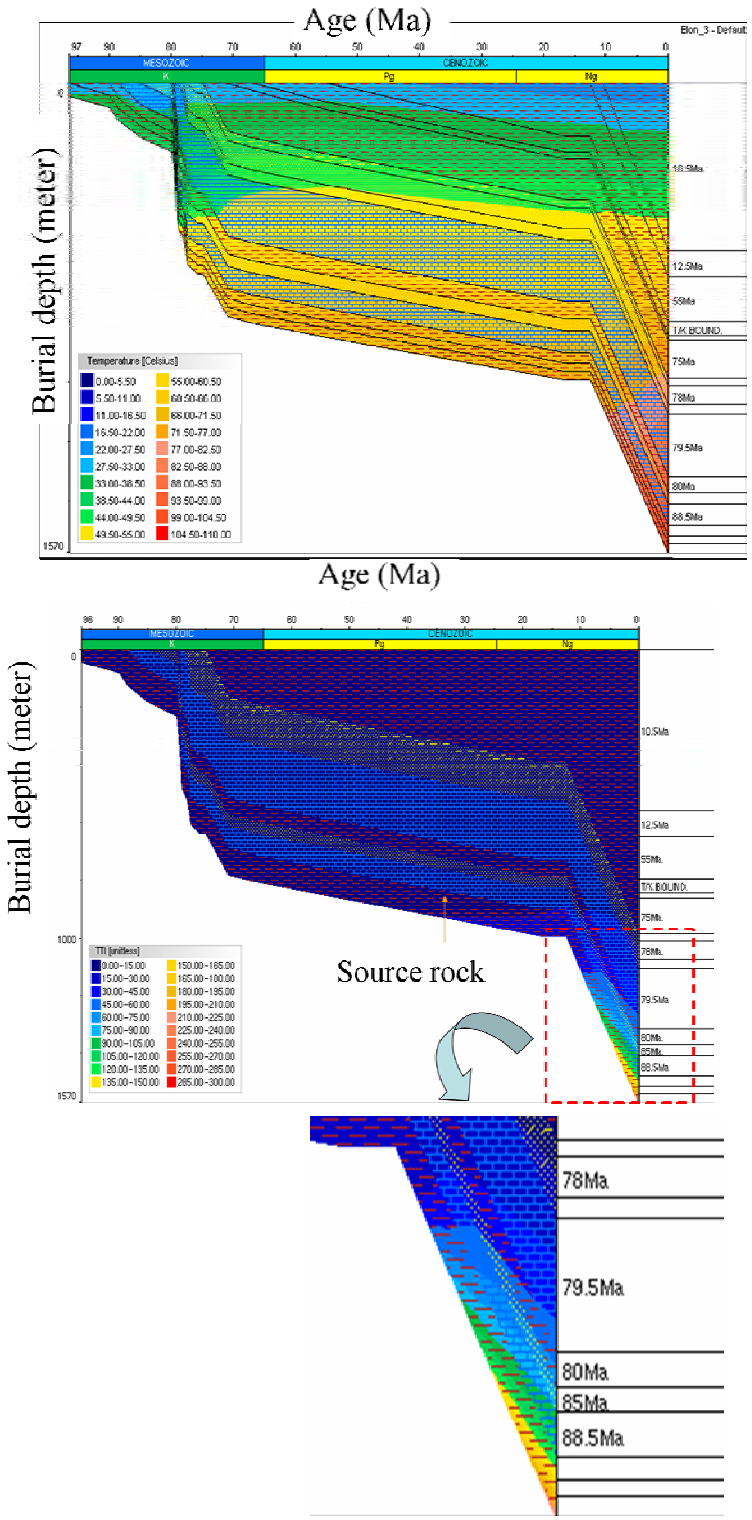

Figure 7.7: 1D burial history diagram at the well location color-coded by Temperature (top) and TTI (bottom). The TTI values are computed in the Petromod software using equation 7.2.

7.7 Relationship between TTI and acoustic velocities

In this section, we present the relationship between TTI and acoustic velocities. The TTI values at the well location are obtained from 1D petroleum system modeling discussed in previous section. These TTI values are then plotted against the compressional (V_P) and the shear velocities (V_S) measured at the well. Figure 7.8 shows the plots of V_P versus TTI, and V_S versus TTI. We find that both V_P and V_S increase with TTI. We fit a general exponential equation of the following form:

$$f(x) = a\exp(bx) + c\exp(dx) \tag{7.6}$$

where, x is TTI and $f(x)$ is velocity as function of TTI. The exponential fits of velocities are shown in Figure 7.8 along with 95 % confidence bounds. The coefficients of the exponential fits (and 95% confidential bounds) for V_P (kilometer/sec) versus TTI using equation 7.6 are as follows:

a= 2.548 (2.138, 2.958)

b= 0.0004934 (-0.000434, 0.001421)

c= -0.7916 (-1.222, -0.3611)

d= -0.05831 (-0.1291, 0.0125)

where, the values within bracket represent 95% confidence bounds. The R-square of the fit is 0.7.

The coefficients of the exponential fits (and 95% confidential interval) for V_S (kilometer/sec) versus TTI using equation 7.6 are as follows:

a= 1.053 (0.744, 1.361)

b= 0.0009603 (-0.0006577, 0.002578)

c= -0.4972 (-0.815, -0.1793)

d= -0.04791 (-0.1154, 0.0196)

The R-square of the fit is 0.7.

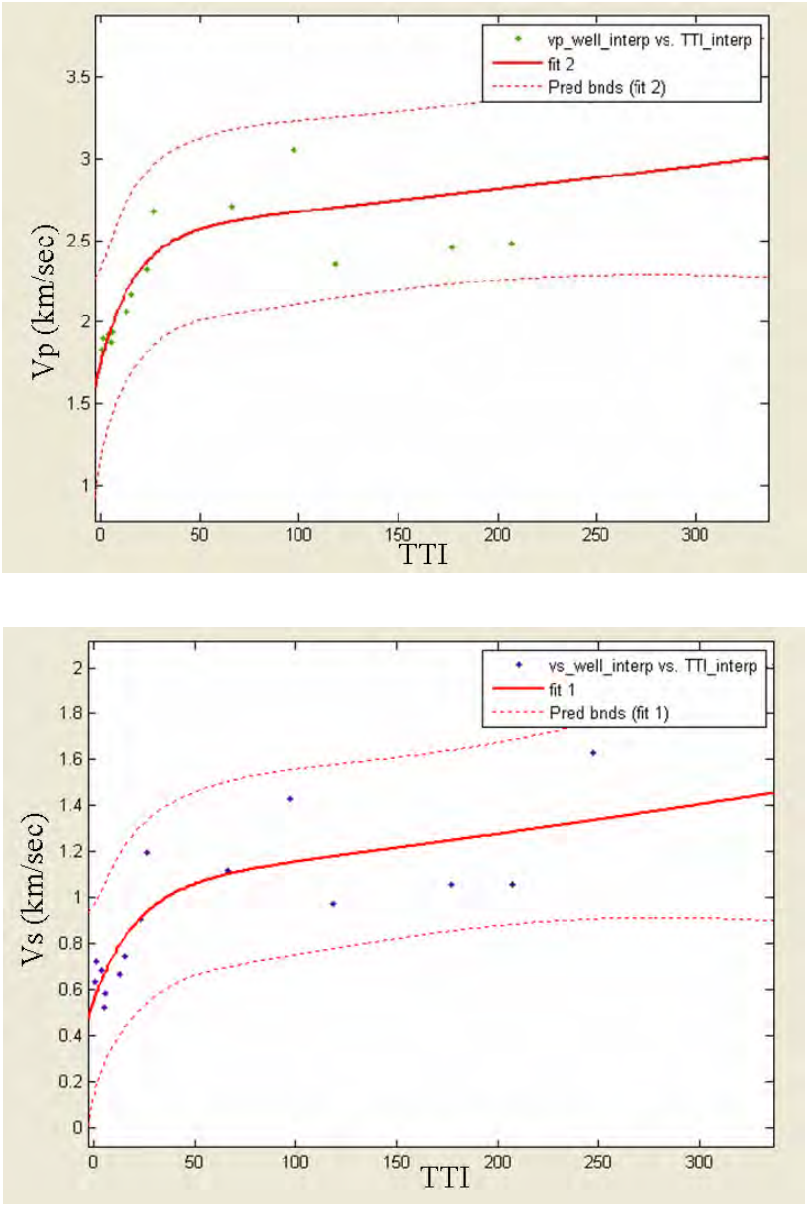

Figure 7.8: V_P vs. TTI (top) and V_S vs. TTI (bottom) with exponential fits to the data (solid line). The 95 % confidence bounds are shown in dashed line.

TTI can be expressed in terms of Vp and Vs as follows:

$$TTI = 0.00233 \exp(4.012 V_P) \tag{7.7}$$

$$TTI = 0.5708 \exp(4.528 V_S) \tag{7.8}$$

where Vp and Vs are in kilometer/sec. Equations 7.7 and 7.8 can be useful to predict TTI

from seismic velocities.

7.8 Conclusion

We test the hypothesis that acoustic velocities of rock depend on temperature and time index (TTI). TTI is an important thermal maturity indicator that can be correlated with oil and gas window, and factors affecting reservoir quality (e.g., overpressure, chemical compaction). However, existing rock physics models (theoretical, empirical, and numerical) do not provide any explicit relationships between seismic velocities and TTI. In this chapter, we attempt to find an empirical-numerical relation between TTI and seismic velocities. For this, we perform petroleum system modeling at a well location in deep-water petroleum system at the Rio Muni Basin, West Africa. The TTI values from numerical modeling are then compared with velocities measured at the same well location. We find that both V_P and V_S increase with TTI and a general exponential equation fits the data reasonably well. Our modeling results can be useful to predict TTI and thereby thermal maturity from observed velocities at the frontier analog basins.

Our study lays preliminary foundation linking acoustic velocities with TTI. Future research can involve: (1) compute seismic velocities using facies-specific theoretical rock physics model, and then compare those velocities with TTI obtained from basin modeling; (2) extend the 1D basin simulation to 2D and 3D simulations using maps of chronostratigraphic surfaces interpreted from 3D volume of seismic data; (3) incorporate information about unconformities from paleontological data; (4) calibrate source rock parameters with geochemical measurements; and (5) perform risk analysis for different input and boundary conditions in petroleum system modeling.

7.9 Acknowledgements

This work was supported by the Stanford Rock Physics and Borehole Geophysics (SRB) project and by DOE awards DE-FC26-04NT15506 and DE-FG02-03ER15423. We acknowledge Ken Peters for valuable discussions. We also acknowledge IES and US Geological Survey for providing Petromod software license to Stanford University. We

are thankful to Schlumberger for providing Petrel software license to Stanford Rock Physics.

7.10 References

Allen, P.A., and Allen, J.R., 1996, Basin Analysis: Principles and Applications: Blackwell Scientific Publications, 451.

Aziz, K., and Settari, A., 1979, Petroleum Reservoir Simulation: Applied Science Publishers, 476.

Baric, G., Mesic, I., Jungwirth, M., and Sparic, D., 1991, Gas and gas condensate-fields in the north-west of the Drava depression, Yugoslavia. In A.M. Spencer (Ed.), Generation, accumulation and production of Europe's hydrocarbons, Special Publication of the European Association of Petroleum Geoscientists No. 1: 323-339.

Barker, C., 1972, Aquathermal pressuring—role of temperature in development of abnormal pressure zones: AAPG Bulletin, 56, 2068–2071.

Behar, F., Vandenbroucke, M., Tang, Y., Marquis, F., and Espitalie, J., 1997, Thermal cracking of kerogen in open and closed systems: Organic Geochemistry, 26, 321-339.

Bjørkum, P.A., 1996, How important is pressure in causing dissolution of quartz in sandstones?: Journal of Sedimentary Research, 66, 147-154.

Bjørkum, P.A., Oelkers, E.H., Nadeau, P.H., Walderhaug, O., and Murphy, M.W., 1998, Porosity prediction in quartzose sandstones as a function of time, depth, temperature, stylolite frequency, and hydrocarbon saturation: AAPG Bulletin, 82, 637-648.

Bjorlykke, K., Jahren, J., Mondol, N.H., Marcussen, O., Croize, D., Peltonen, C., and Thyberg, B., 2009, Sediment Compaction and Rock Properties: AAPG Search and Discovery Article #50192 (2009).

Connan, J., 1984, Biodegradation of crude oils in reservoirs. In: J. Brooks and D.H. Welte, Editors: Advances in Petroleum Geochemistry Volume 1, Academic Press, London.

Sclater, J. G., and Christie, P. A. F., 1980, Continental stretching: an explanation of the post-Mid-Cretaceous subsidence of the Central North Sea Basin: Jour. Geophys. Res., 85, 3711–3739.

Dailly, P., Goh, K., Lowry, P., and Monson, G., 2001, The Rio Muni Basin of Equatorial Guinea: A new hydrocarbon province: GCSSPEM Foundations 21st Annual Research Conference, Petroleum system of deep-water basins.

Dailly, P., Lowry, P., Goh, K., and Monson, G., 2002, Exploration and development of Ceiba Field, Rio Muni Basin, Southern Equatorial Guinea: The Leading Edge, 21, 1140-1146.

Dieckmann, V., 2005, Modeling petroleum formation from heterogeneous source rocks: The influence of frequency factors on activation energy distribution and geological prediction: Marine and Petroleum Geology, 22, 375-390.

Ehrenberg, S.N., 1990, Relationship between diagenesis and reservoir quality in sandstones of the Garn Formation, Haltenbanken, mid- Norwegian continental shelf: AAPG Bulletin, 74, 1538-1558.

Ehrenberg, S.N., 1993, Preservation of anomalously high porosity in deeply buried sandstones by grain-coating chlorite: examples from the Norwegian continental shelf: AAPG Bulletin, 77, 1260-1286.

Ehrenberg, S.N., and Nadeau, P.H., 1989, Formation of diagenetic illite in sandstones of the Garn Formation, Haltenbanken area, mid-Norwegian continental shelf: Clay Minerals, 24, 233-235.

Goff, J. C., 1983, Hydrocarbon generation and migration from Jurassic source rocks in the East Shetland Basin and Viking Graben of the Northern North Sea: J. Geol. Soc. Lond., 140, 445-474.

Hantschel, T., and Kauerauf, A.I., 2009, Fundamentals of Basin and Petroleum Systems Modeling: Springer Verlag.

Horvath, F., Szalay, A., Dovenji, P., and Rampler, J., 1986, Structural and thermal evolution of the Pannonian Basin: In J. Burrus (Ed.), Thermal Modeling in Sedimentary Basins, 339-358.

Houseknecht, D.W., Influence of grain size and temperature on intergranular pressure solution, quartz cementation, and porosity in a quartzose sandstone: Journal of Sedimentary Research; 1984, 54, 348-361.

Lawrence, S. R., Munday, S., and Bray, R., 2002, Regional geology and geophysics of the eastern Gulf of Guinea (Niger Delta to Rio Muni): The Leading Edge, 21, 1112-1117.

Leder, F., and Park, W. C., 1986, Porosity reduction in sandstone by quartz overgrowth: AAPG Bulletin, 70, 1713-1728.

Lopatin, N.V., 1971, Temperature and time as geologic factors in coalification: Akademiia Nauk SSSR, Izvestiia Seriia Geologicheskalu, 3, 95-106.

Magoon, L.B., and Dow,W.G., 1994, The petroleum system- From source to trap: AAPG memoir, 60, 655.

Magoon, L.B., 2004, Petroleum system: Nature's Distribution system for oil and gas: Encyclopedia of energy, 4, 823-836.

Mavko, G., Mukerji, T., and Dvorkin, J., 1998, The Rock Physics Handbook, tools for seismic analysis in porous media: Cambridge University press.

Mohriak, W. U., Mello, M. R., Bassetto, M., Vieira, I. S., and Koutsoukos, E. A. M., 2000, Crustal Architecture, Sedimentation, and Petroleum Systems in the Sergipe-Alagoas Basin, Northeastern Brazil: AAPG Memoir 73, Chapter 20, 273 – 300.

Nadeau, P.H., and Bain, D.C., 1986, Composition of some smectites and diagenetic illitic clays and implications for their origin: Clays & Clay Minerals, 34, 455-464.

Nadeau, P.H., Peacor, D.R., Yan, J., and Hiller, S., 2002, I/S precipitation in pore space as the cause of geopressuring in Mesozoic mudstones, Egersund Basin, Norwegian Continental Shelf: American Mineralogist, 87, 1580-1589.

Palumbo, F., Main, I. G., and Zito, G., 1999, The thermal evolution of sedimentary basins and its effect on the maturation of hydrocarbons: Geophysical Journal International, 139, 248-260.

Passey,Q.R., S.Creaney, J.B.Kulla, F.J.Moretti and J.D.Stroud, 1990, A practical model for organic richness from porosity and resistivity logs: AAPG Bulletin, 74, 1777-1794.

Peters, K.E., and M.R. Cassa, 1994, Applied source rock geochemistry. In: L.B. Magoon and W.G. Dow, Editors, The Petroleum System—from source to trap, The American Association of Petroleum Geologists, Memoir 60, 93–120.

Peters, K.E., Walters, C.C., and Moldowan, J.M., 2005, The Biomarker Guide- volume 1: Cambridge University Press., 97-100 and 117-118.

Pepper, A.S., Covri, P.J., 1995, Simple kinetic models of petroleum formation: Part I-Oil and gas generation from kerogen: Marine and Petroleum Geology, 12, 291-319.

Posamentier, H. W., and Vail P. R., 1988, Eustatic controls on clastic deposition II-Sequence and systems tract models: Sea-level Changes: An Integrated Approach (eds., Wilgus, C.K., Hastings, B.S., Posamentier, H., Van Wagoner, J., Ross, C.A. and Kendall, C.G. St.C.), SEPM, Special Publication, 42, 125-154.

Renard, F., Ortoleva, P., and Gratier, J.P., 1997, Pressure solution in sandstones: influence of clays and dependence on temperature and stress: Tectonophysics, 280, 257-266,

Robert, P., 1988, Organic metamorphism and geothermal history: ELFAquitaine and D. Reidl, Dordrecht, 311.

Turner, J. P., 1995, Gravity-driven structures and rift basin evolution: Rio Muni Basin, offshore equatorial West Africa: AAPG Bulletin, 79, 1138-1158.

Vetö, I., and Dövényi, P., 1986, Methods for paleotemperature estimation using vitrinite reflectance using vitrinite reflectance data: a critical evaluation, in Lecture notes in Earth Science, Paleogeothermcs: Evaluation of Geothermal Conditions in the Geological Past, 5, 105-118.

Waples, D. W., 1980, Time and temperature in petroleum formation: application of Lopatin's method to petroleum exploration: AAPG Bulletin, 64, 916-926.

Waples, D.W., Suizu, M., and Kamata, H., 1992, The art of maturity modeling: Part 2-Alternative models and sensitivity analysis: AAPG Bulletin, 76, 47-66.

Welte, D.H., Horsfield, B., Baker, D.R., eds., 1997, Petroleum and basin evolution: New York, Springer-Verlag,535.

Wilhelms,A., 2001, Biodegradation of oil in uplifted basins prevented by deep-burial sterilization: Nature, 411, 1034-1037.

Wrygala,B.P., 1989, Integrated study of an oil field in the southern Po basin, northern Italy: PhD dissertation, University of Koln. Kernforschungsanlage Jueich, 217.

Yukler, M., 1987, How essential is basin modelling in petroleum exploration: 7th Bi-annual Petroleum Congress of Turkey, Turkish Assoc. Petroleum Geolology,16.